6-8-2018

Search for Supersymmetry in Proton-Proton Collisions at 13 TeV with the CMS Detector using Identified Top Quarks

Yagya R. Joshi
Florida International University, yjosh001@fiu.edu

DOI: 10.25148/etd.FIDC006832

FLORIDA INTERNATIONAL UNIVERSITY

Miami, Florida

SEARCH FOR SUPERSYMMETRY IN PROTON-PROTON COLLISIONS AT 13 TEV WITH THE CMS DETECTOR USING IDENTIFIED TOP QUARKS

A dissertation submitted in partial fulfillment of the

requirements for the degree of

DOCTOR OF PHILOSOPHY

in

PHYSICS

by

Yagya Raj Joshi

2018

To: Dean Michael R. Heithaus
College of Arts, Sciences, and Education

This dissertation, written by Yagya Raj Joshi, and entitled Search for Supersymmetry in Proton-Proton Collisions at 13 TeV with the CMS Detector using Identified Top Quarks, having been approved in respect to style and intellectual content, is referred to you for judgment.

We have read this dissertation and recommend that it be approved.

Misak Sargsain

Brain Raue

Pete E. C. Markowitz

Grenville Draper

Jorge L. Rodriguez, Major Professor

Date of Defense: June 08, 2018

The dissertation of Yagya Raj Joshi is approved.

Dean Michael R. Heithaus
College of Arts, Sciences, and Education

Andrés G. Gil
Vice President for Research and Economic Development
and Dean of the University Graduate School

Florida International University, 2018

ABSTRACT OF THE DISSERTATION

SEARCH FOR SUPERSYMMETRY IN PROTON-PROTON COLLISIONS AT 13 TEV WITH THE CMS DETECTOR USING IDENTIFIED TOP QUARKS

by

Yagya Raj Joshi

Florida International University, 2018

Miami, Florida

Professor Jorge L. Rodriguez, Major Professor

A search for supersymmetry is presented based on proton-proton collision events containing identified hadronically-decaying top quarks (i.e., events with no identified leptons), and an imbalance $E_{\mathrm{T}}^{\mathrm{miss}}$ in transverse momentum. The data were collected with the Compact Muon Solenoid (CMS) detector at the CERN Large Hadron Collider (LHC) at a center-of-mass energy of 13 TeV, and correspond to an integrated luminosity of 35.9 fb^{-1}. The 84 exclusive search regions are defined in terms of the multiplicity of bottom-quark-jet and top-quark candidates, the $E_{\mathrm{T}}^{\mathrm{miss}}$, the scalar sum of jet transverse momenta, H_{T}, and the transverse mass variable sensitive to the pair production of heavy particles, each of which decays into an invisible particle M_{T2}. A novel and robust top quark reconstruction algorithm, which is based on a multivariate approach and is capable of identifying top quarks in wide spectrum of top quark transverse momentum, is developed. Methods in the modeling of events arising from quantum chromodynamics and electroweak boson production, which are major backgrounds in searches for new physics at the LHC, are also presented. No statistically significant excess of events is observed relative to the expectation from the standard model. Discussion of the non-excluded regions of the model parameter space is given. Lower limits on the masses of supersymmetric particles are determined at a 95% confidence level in the context of simplified models with top quark production. For a

model with direct top squark pair production followed by the decay of each top squark to a top quark and a neutralino, top squark masses up to 1020 GeV and neutralino masses up to 430 GeV are excluded. For a model with pair production of gluinos followed by the decay of each gluino to a top quark-antiquark pair and a neutralino, gluino masses up to 2040 GeV and neutralino masses up to 1150 GeV are excluded. These limits extend previous results obtained with 8 TeV data and 2.3 fb^{-1}, 13 TeV data.

DEDICATION

To Serene, love of our life.

ACKNOWLEDGMENTS

For this accomplishment, I would like to express my sincere gratitude to my family, friends, and professors for their continuous support and encouragement.

At first, I would like to express my heart-felt gratitude to my excellent adviser Prof. Jorge Rodriguez for his continuous support, intellectual guidance, expert suggestions, and most of all, the trust he put in me. This work would not have been possible without his support, guidance, and trust. He continuously guided me towards academic excellence. I would like to thank him for being an excellent mentor and a great teacher throughout my graduate career. I wish to thank Prof. Rodriguez along with the National Science Foundation for funding this work.

I would also like to thank members of my committee including Profs. Pete Markowitz, Misak Sargsian, Brian Raue, and Grenville Draper for their passionate support at several stages of writing this dissertation. I would like to thank all the physics professors for their support and guidance throughout my graduate career.

I also like to thank all the other scientists, engineers and theorists who I do not know personally, but are fellow collaborators and contributors to the Compact Muon Solenoid experiment and the Large Hadron Collider. They had the commitment, innovation and ambition to design an experiment like no other, stick with it for decades and see it all the way through. They laid the foundation for future students to expand their knowledge for years to come. Thank you Sam, Hongxuan, Joe, and Scarlet for being such a helpful collaborators.

I am indebted to my Buwa and Aama for the sacrifice they made to ensure that I had an excellent education. Thank you Ananta and Amrita their unconditional love.

I want to express my love and heart-felt gratitude to my wife Iru for her support and sacrifice. Finally, to Serene, I didn't know love until I had her.

TABLE OF CONTENTS

LIST OF TABLES

LIST OF FIGURES

FIGURE PAGE

CHAPTER 1

Introduction

My research focuses on the search for massive, weakly interacting, elementary particles known as supersymmetric top quarks. The research is conducted with massive amounts of data collected with Compact Muon Solenoid (CMS) experiment located at CERNs Large Hadron Collider (LHC). The LHC collides two proton beams at 13 trillion electron volts, the highest energy ever achieved. On occasion, these very high energy collisions result in new states of mater that subsequently decay into well-known particles that leave electronic traces in the CMS detector. By reconstructing the events we can search for new and exotic forms of matter; our search is targeted at particular signatures that are consistent with supersymmetric particles that, if discovered, could shed light on the most profound mysteries in physics and astronomy. For example, supersymmetric particles could explain why the Higgs bosons mass, discovered at the LHC in 2012, is stable against quantum corrections (cancelation of very high order terms in theoretical predictions to the measured mass). Moreover, since supersymmetric particles are both massive and weakly interacting they are excellent candidates for the constituents of the, as yet, unexplained dark matter, which we currently know makes up 80% of all the matter in the universe.

Additionally, to analyze the huge volume of data and sift through the billions of events, a sophisticated and complex set of tools and data analysis techniques were developed. The tools and analysis by-products developed in my research were published for use by the global high energy physics community and will advance further studies in this field. The tools themselves are based on sophisticated machine learning techniques that will benefit further research at the LHC and the other high energy physics experiments in the future. The analysis techniques applied here are uniquely

designed to perform optimally with the dataset collected by the CMS experiment at the LHC during the 2015 run period known as Run−2.

Chapter 2 describes the theoretical framework of the entire dissertation. It begins with a brief description of elementary particles, and the forces of nature. In the first section, I focus on the theory of the strong, weak, and electromagnetic interactions all within the context of relativistic quantum gauge theories known as the Standard Model (SM) of particle physics. I also describe the Higgs Mechanism and show that through the interaction with the doublet scalar Higgs field, the gauge bosons and fermions acquire their masses via the process known as Electroweak Symmetry Breaking. I then describe some outstanding problems with the SM. They include the fact that some observations are directly contradicted by the SM, while others are completely unexplained by the SM. In addition, there are some theoretical complications such as the Hierarchy Problem. The final section presents supersymmetry as a potential natural solution to the problems mentioned here. The final section of the chapter focuses on how supersymmetry may manifest at the energy scale the LHC is currently exploring.

Chapters 3 and 4 give a description of the hardware and software segments of the experiment. The former describes how the LHC uses state of the art technologies to accelerate proton beams up to a center of mass energy of 13 TeV. The description of the LHC machine will be followed by an explanation of the CMS detector, its components, their construction, objectives, design, and performance. Chapter 4 details how information from the detector elements are used by the CMS particle flow algorithm to reconstruct particles coming from the proton-proton collisions.

Chapter 5 covers the central feature of this study. I introduce the simplified models that are SUSY inspired models with a few well defined final states that decay via specific channels. In this work we target two simplified models where supersymmetric particles are produced in pairs that subsequently decay into a standard model particle and a weakly interacting particle. In both targeted searches, the standard model particle produced in the final state is a top quark and a weakly interacting particle is known as the Lightest Supersymmetric particle (LSP). I define the search strategy, variables used, state the assumptions made and justify their use. I also describe the backgrounds observed and the methods used to suppress them. Finally, I outline the work done on developing a novel top quark reconstruction technique used for the first time. This work was a joint effort with fellow CMS collaborators.

Chapter 6 mentions the methods of background estimation in detail. I focus on the estimate of backgrounds from top and W decays and, for completeness, highlight the work done by my colleagues on other important backgrounds in the data.

In Chapter 7 the results of the analysis are presented along with a discussion on the systematic uncertainties and a statistical interpretation of the results. There is a comparison of all simulated Monte Carlo backgrounds against the entire data collected in Run-2. I also discuss all sources of the systematic uncertainties and a brief description of methods of their evaluation. The chapter ends with the statistical methods used to interpret a data and the exclusion limit on the parameters of interest. The parameters of interest are the mass of the gluino, the stop mass, and the LSP mass.

CHAPTER 2

Theoretical Framework

2.1 Overview

The aim of particle physics is to understand the structure and behavior of the universe in terms of fundamental building blocks known as elementary particles. Understanding the natural universe requires three basic ingredients: particles that constitute matter, the forces those particles feel, and finally the influence of those forces on those particles. Many elementary particles are commonly not observed in nature. Rather, they are created during collisions between particles at sufficiently high energies either at particle accelerators or in cosmic-ray interactions. All particles and their interactions are currently described by a collection of quantum field theories known as the Standard Model of Particle Physics. Details of the Standard Model will be discussed in Section 2.2.

All matter in the universe is composed of spin-$\frac{1}{2}$ particles called fermions. There are two types of fermions, leptons and quarks. In analogy with the electric charge, quarks have an additional charge-like property known as color charge. Unlike electric charge, the color charge comes in three different varieties, Red(R), Green(G), and Blue(B). These color charges are responsible for the strong interaction, which is mediated through the exchange of spin-1 gauge bosons called gluons. Gluons bind quarks into hadrons and nucleons. Similarly, a gauge boson known as the photon is the particle mediating electromagnetic interactions. In addition to gluons and photons there are two other types of gauge bosons that transmit the weak interaction, responsible for some nuclear decays, the W and Z bosons. Unlike gluons and photons, these bosons have mass ($M_W \approx 80$ GeV and $M_Z \approx 91$ GeV) and are the force carriers of the weak interactions. The gauge bosons, along with the fermions and the Higgs boson, are

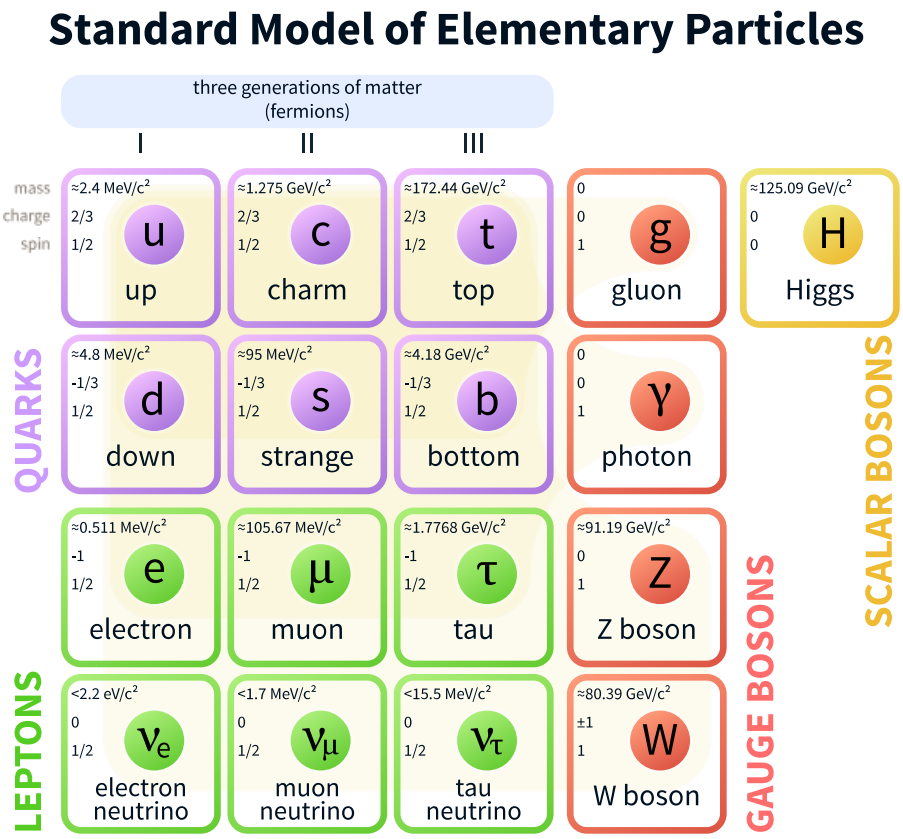

Figure 2.1: The Standard Model of elementary particles (more schematic depiction), with the three generations of matter, gauge bosons are in the fourth column, and the Higgs boson in the fifth column [2].

shown in Table 2.1.

With the recently discovered Higgs boson [13] at the Large Hadron Collider (LHC), the standard model of particle physics is complete. Detailed discussion about the Higgs boson and its role is presented in the Section 2.2.3.

2.2 Standard Model

The Standard Model (SM) is one of the most successful theories in physics. There is extraordinary matching between theoretical predictions and experimental observa-

Table 2.1: Forces and Gauge Bosons [1].

Force	Acts On	Transmitted by
Gravity	All particles	graviton (massless, spin-2)
Electromagnetism	All electrically charged particles	Photons(γ (massless, spin-1)
Weak interaction	quarks leptons, electroweak gauge bosons	$W^{\pm}$, Z^0 (heavy spin-1)
Strong interaction (QCD)	All colored particles (quarks and gluons)	Eight gluons(g) (massless spin-1)

tions. With carefully defined symmetry arguments in the context of special relativity and quantum mechanics, we can derive the entire theory known as the Standard Model. In the following section we will derive the Lagrangian for spin $\frac{1}{2}$ fermions from the Dirac approach and again from symmetry arguments described by the gauge group *U(1)*. Later, the entire SM will be derived from gauge invariance under the $SU(3) \times SU(2) \times U(1)$ local gauge symmetry group.

2.2.1 Quantum Electrodynamics(QED)

The operator version of the standard relativistic relation $E^2 = m^2c^4 + \vec{p}^2c^4$ can be written in natural units ($\hbar = 1, c = 1$) as the **Klein Gordon** equation [1]

$$(\partial^2 - m^2)\phi = 0. \tag{2.1}$$

A major problem with the Klein Gordon equation is that energy eigenvalues have both negative and positive solutions $E = \pm\sqrt{m^2 + \vec{p}^2}$. The negative energy eigenvalues are physically meaningless because negative energy means we don't have a true

vacuum. As a result particles can cascade down forever, yielding an infinite amount of radiation.

Dirac invented the "anti-particle" to explain negative energy eigenvalues. The Lagrangian for spin-$\frac{1}{2}$ particles in terms of Dirac spinor can be written as

$$\mathcal{L}_D = \bar{\psi}(i\gamma^\mu \partial_\mu - m)\psi. \tag{2.2}$$

The classical electromagnetic Lagrangian with quadratic kinetic terms is given by the expression,

$$\mathcal{L}_{EM} = -\frac{1}{4}F_{\mu\nu}F^{\mu\nu} - J^\mu A_\mu, \tag{2.3}$$

where J^μ and A_μ are the 4-vector current and potential, respectively. $F^{\mu\nu}$ is an anti-symmetric electromagnetic field strength tensor given by the expression $\partial^\mu A^\nu - \partial^\nu A^\mu$. Looking at the Dirac Lagrangian (Eq 2.2) with complex spinor fields ψ and $\psi^\dagger$, we can make the transformation $\psi \to e^{i\alpha}\psi$ and $\psi^\dagger \to e^{-i\alpha}\psi^\dagger$, where α is an arbitrary real number. We call this transformation the $U(1)$ transformation. We notice that the Lagrangian is invariant under $U(1)$ symmetry, with current

$$j^\mu = \bar{\psi}\gamma^\mu\psi. \tag{2.4}$$

In the example above we observed that the symmetry was a **Global Symmetry**. That is a symmetry that changes the field at all points in space.

It is also seen that the Lagrangian in Eq. 2.2 along with the electromagnetic part in Eq. 2.3 have no terms in common, meaning there is no interaction in the theory. In the real world, particles interact with with each other so we need to add an interaction

term into the electromagnetic Lagragian as

$$\mathcal{L} = \mathcal{L}_D + \mathcal{L}_{EM} + \mathcal{L}_{int}, \tag{2.5}$$

so that

$$\begin{aligned} \mathcal{L} &= \bar{\psi}(i\gamma^\mu \partial_\mu - m)\psi - \frac{1}{4}F_{\mu\nu}F^{\mu\nu} - J^\mu A_\mu - qj^\mu A_\mu, \\ &= \bar{\psi}(i\gamma^\mu \partial_\mu - m)\psi - \frac{1}{4}F_{\mu\nu}F^{\mu\nu} - (J^\mu + qj^\mu)A_\mu. \end{aligned} \tag{2.6}$$

$\mathcal{L}$ is still invariant under $U(1)$ and the current is unchanged, i.e. $\bar{\psi}\gamma^\mu\psi$. Setting $q = e$, the magnitude of electron's charge, then Eq. 2.6 is the Quantum Electrodynamics Lagrangian (QED). In the next couple of paragraphs, we derive the same QED Lagrangian in a more fundamental way.

As we discussed before, the Dirac Lagrangian in Eq. 2.2 is invariant under $U(1)$ transformation and the underlying symmetry was essentially *global*. But we want our symmetry to be *local*, so that α is space-time dependent. Thus, the differential operator now acts not only on ψ, but also on $\alpha(x)$. That essentially leaves the Lagrangian with one extra term. We still want invariance of $\mathcal{L}$ under a local $U(1)$ transformation, so we replace the derivative ∂_μ with a covariant derivative,

$$D_\mu = \partial_\mu - ig_1 A_\mu, \tag{2.7}$$

where the g_1 is the coupling strength and A_μ is the invariant vector field under $U(1)$ if it transforms as

$$A_\mu \to A_\mu + \frac{1}{g_1}\partial_\mu \alpha. \tag{2.8}$$

Now our new Lagrangian is

$$\mathcal{L} = \bar{\psi}(i\gamma^\mu \partial_\mu - m - \frac{1}{g_1}\gamma^\mu A_\mu)\psi. \tag{2.9}$$

Using Eq. 2.8 in Eq. 2.9 followed by some algebra, it is clear that $\mathcal{L}$ is now invariant under $U(1)$ and the conserved quantity is charge $j^\mu = \bar{\psi}\gamma^\mu\psi$. A field A_μ has no kinetic term, and therefore there is no kinetic energy in the system. But in reality, we can not imagine any physical field without the kinetic energy. So we introduce a gauge-invariant kinetic term for an arbitrary field A_μ as

$$\mathcal{L}_{Kin,A} = -\frac{1}{4}F_{\mu\nu}F^{\mu\nu},$$

where $F^{\mu\nu}$ is expressed in terms of a covariant derivative

$$F^{\mu\nu} = \frac{i}{g_1}[D^\mu, D^\nu]. \tag{2.10}$$

For any physical field A_μ, it is natural to assume that there is some source causing the field, which we simply call J^μ. This makes our final Lagrangian

$$\mathcal{L} = \bar{\psi}(i\gamma^\mu D_\mu - m)\psi - \frac{1}{4}F_{\mu\nu}F^{\mu\nu} - J^\mu A_\mu, \tag{2.11}$$

which is the same as we derived in Eq. 2.6.

We started with the Lagrangian for spin $\frac{1}{2}$ particles with a global $U(1)$ symmetry, added kinetic terms, and finally required that the gauge symmetry be local. The field A_μ, upon quantization describes a spin-1 gauge boson known as the photon [14].

2.2.2 Quantum Chromodynamics(QCD)

Inspired by success of local gauge theory for QED, now we try to generalize this approach to QCD [1], the theory that describes the strong interactions and is responsible for the binding of quarks into mesons and baryons. Mesons are quark anti-quark bound states while baryons are three-quarks bound states. The Δ^{++} particle is a particle with a "++" electric charge and a spin of 3/2. A spin 3/2 particle composed of half-integer-spin quarks must include a hidden degree of freedom to satisfy Fermi-Dirac statistics. The hidden degree of freedom must come in three distinct varieties, one for each of the three quarks, which we call color. Baryons can thus be thought of as half-integer-spin composite states composed of three quarks, each with a different color, while mesons are composite states composed of quark anti-quark pairs, each representing color combinations that are colorless or color-singlets. The underlying theory of QCD is a non-abelian gauge theory with an $SU(3)$ symmetry group. To cope with a non-Abliean theory, consider a Lagrangian $\mathcal{L}$ that is invariant under $SU(3)$ symmetry

$$\psi^j \rightarrow U^{jk}\psi^k, \tag{2.12}$$

where U^{jk} is a 3×3 unitary matrix of $SU(3)$. U^{jk} can be written as an exponential function of Hermition operators that are linear combination of the generators of a Lie-algebra. Eq. 2.12 can be written as,

$$\psi \rightarrow U\psi = e^{i\theta^a(x)T^a}\psi \equiv e^{i\vec{\theta}.\vec{T}}\psi, \tag{2.13}$$

where θ^a are the $3^2 - 1 = 8$ parameters of the $SU(3)$ group, and T^a are generator matrices of the group. These commutators obey the commutation relation

$$[T^a, T^b] = if_{abc}T^c,$$

where f_{abc} is called the structure constant of the group.

To construct the QCD Lagrangian we use the same arguments used to motivate QED but now the result is more complicated due to a larger symmetry group. The covariant derivative takes the form

$$D_\mu = \partial_\mu - ig_2 T^a A^a_\mu, \tag{2.14}$$

where the term g_2 is the strong coupling constant and the field A^a_μ is a field that transforms as

$$A^a_\mu \to A^a_\mu - \frac{1}{g_2}\partial_\mu \theta_{a(x)} - f_{abc}\theta_b A^a_\mu. \tag{2.15}$$

The extra term in the transformed field will cancel the additional terms introduced by gauge transformation of the covariant derivative. Now adding the kinetic energy term completes the Lagrangian, which is still invariant under the gauge transformation. The field strength tensor takes the form

$$F^a_{\mu\nu} = \partial_\mu A^a_\nu - \partial_\nu A^a_\mu - g_2 f_{abc} A^b_\mu A^c_\nu. \tag{2.16}$$

Finally, with Eqs. 2.14, 2.15 and 2.16, we can write the complete Lagrangian for QCD as

$$\mathcal{L} = \bar{\psi}(i\gamma^\mu D_\mu - m)\psi - \frac{1}{4}F_{\mu\nu}F^{\mu\nu}. \tag{2.17}$$

This has the exact same form as the QED Lagrangian but with extra complexity due to the $SU(3)$ symmetry hidden in the covariant derivative and the stress energy tensor. These extra terms give rise to additional interaction terms between the gauge bosons as these have the color charge and can thus interact with each other as well

as with the colored quarks.

2.2.3 Electroweak Theory and Higgs Mechanism

QED describes the physics of electrically charged fermions interacting with each other and the electromagnetic field, while QCD describes the physics of particles with color charge that interact with each other and a gluonic field. What QED and QCD fail to describe are some types of decays of heavier particles into lighter ones. For example, in beta decay a nucleus can transmute into another nucleus by the emission of a beta particle (either a positron or electron) and a neutrino. This type of process is not described either by QED nor QCD and is of primary importance in the nuclear reactions that powers our sun. The list of reactions that are not explained by QCD or QED is large. A necessity for a unified theory of electromagnetic and weak interactions was realized and those problems were elegantly solved by yet another gauge theory that combines the electromagnetic and weak interaction into a theory known as the electroweak theory [15].

In the theory of electroweak interactions, left handed fermions are represented as doublets and right handed fermions as singlets. The $SU(2)$ symmetry corresponds to an unbroken weak theory with two "weak" charges, in analogy with the $SU(3)$ of the strong interaction. $U(1)$ has a single hypercharge that is analogous to the elerctric charge of QED. Initially the theory has four massless vector bosons, three that correspond to the $SU(2)$ part and one to the $U(1)$ part. These vector bosons will acquire mass through the Higgs Mechanism [16]. We will discuss the Higgs mechanicsm later in this section. The massive vector bosons have all been observed. The W and Z bosons were discovered at CERN by the UA1 and UA2 collaborations at the super

proton sychrotron collider [17].

Getting the Standard Model gauge bosons from group theory is a monumentally significant result, but the problem is they are all massless. This is acceptable for photons and gluons but it has been experimentally verified that the weak bosons have a mass. As mentioned previously, left-handed fermions are $SU(2)$ doublets while right-handed fermions are $SU(2)$ singlets, so the mass term takes the form

$$m\bar{\psi}\psi = m(\bar{\psi_L}\psi_R + \bar{\psi_R}\psi_L). \tag{2.18}$$

This mass term in the Lagrangian would break chiral symmetry [14]. It implies that Dirac fermions are massless but it is clear from observations that they posses a non-zero rest mass. So we now introduce another field ϕ, which is an $SU(2)$ doublet and a complex scalar

$$\phi = \begin{pmatrix} \phi^+ \\ \phi^0 \end{pmatrix}. \tag{2.19}$$

The covariant derivative takes the form

$$D_\mu = \partial - ig^{'}\frac{1}{2}YB_\mu - igTW_\mu, \tag{2.20}$$

where g and $g^{'}$ are coupling constants of different strengths, B_μ is the gauge field of the unbroken $U(1)$ symmetry while W_μ is the gauge field of the unbroken $SU(2)$ symmetry, and T is a vector of Pauli matrices that satisfies the commutation relation,

$$[\sigma_i, \sigma_j] = 2\epsilon_{ijk}\sigma_k. \tag{2.21}$$

These Pauli matrices generate the $SU(2)$ group.

The covariant derivative of Eq. 2.20 acts on left-handed doublets as

$$D_\mu \begin{pmatrix} \psi_u \\ \psi_d \end{pmatrix}_L = (\partial - igTW_\mu + ig^{'}\frac{1}{2}B_\mu) \begin{pmatrix} \psi_u \\ \psi_d \end{pmatrix}_L , \tag{2.22}$$

and the right-handed singlets as

$$D_\mu \psi_R = (\partial + ig^{'}B_\mu)\psi_R. \tag{2.23}$$

Right-handed and left-handed fermions couple with each other via the Yukawa interaction. The Lagrangian for the unbroken electroweak theory can be written in the same fashion as in QCD:

$$\mathcal{L} \;=\; \bar{\psi}(i\gamma^\mu D_\mu - m)\psi - \frac{1}{4}W_{\mu\nu}W^{\mu\nu} - \frac{1}{4}B_{\mu\nu}B^{\mu\nu}, \tag{2.24}$$

where

$$W^i_{\mu\nu} = \partial_\mu W^i_\nu - \partial_\nu W^i_\mu + g\epsilon^{ijk}(W^j_\mu \times W^k_\nu),$$

and

$$B_{\mu\nu} = \partial_\mu B_\nu - \partial_\nu B_\mu.$$

Now with the field we introduced in Eq. 2.19, we write the Lagrangian as

$$\mathcal{L} = (D_\mu \phi)^\dagger (D_\mu \phi) - V(\phi). \tag{2.25}$$

In order to explain the massive W and Z bosons observed in the lab, electroweak symmetry must be spontaneously broken. Thus, we can construct the potential energy

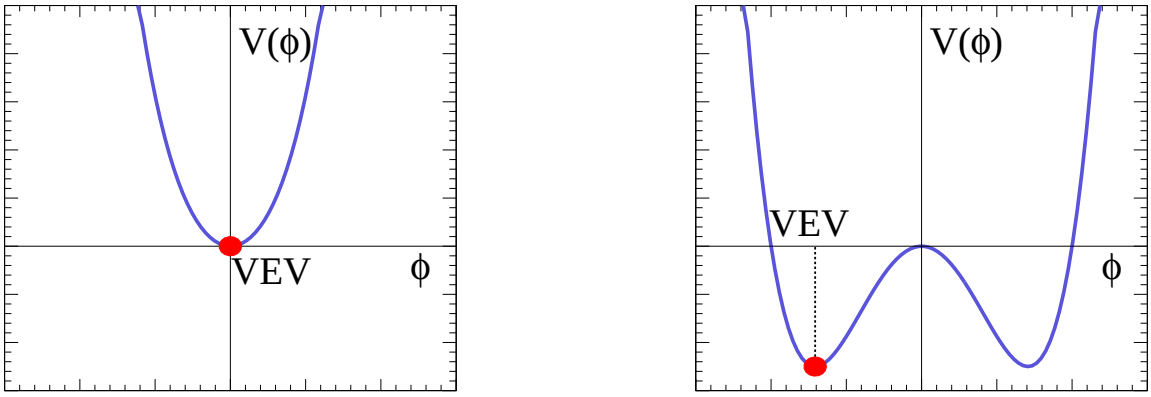

(a) $\mu^2 > 0$ (b) $\mu^2 < 0$

Figure 2.2: Two possible shapes of the potential in Eq. 2.26. A minimum potential (a) indicates no interesting physics but (b) a indicates nonzero vacuum expectation value (VEV) [3].

term from a complex scalar field as mentioned in Eq. 2.19 as

$$V(\phi) \quad = \quad -\mu^2\phi^\dagger\phi + \lambda(\phi^\dagger\phi)^2, \tag{2.26}$$

where μ^2 , $\lambda \in \mathbb{R}$. With such a representation of the potential, it can take basically two forms as shown in Fig. 2.2.

The bounded nature of the potential from below means λ is positive and μ^2 is negative. The potential energy then looks like that shown in Fig. 2.2b. This is referred to as the Mexican hat potential where the minimum is not at V(ϕ) = 0 but at some non-zero ϕ as shown in Fig. 2.2b. This scenario illustrates a non-zero vacuum expectation value (VEV) with a two-fold degeneracy. If we now allow the potential to have an additional degree of freedom, in an orthogonal dimension α, the two-fold degeneracy become continuous. Writing the potential ϕ in terms of the expectation value $\langle\phi\rangle$, α, and massless scalar β, the Lagrangian will have five terms with no $U(1)$ symmetry. Essentially we broke the global symmetry by writing the field, ϕ, in terms

of the quantum fluctuation $(\alpha + i\beta)$ around $\langle\phi\rangle$ and we get massless bosons, known as Goldstone Bosons.

Now let us force a symmetry to be a local with the same potential as in Eq. 2.26 such that the vacuum expectation value is $\phi = \langle\phi\rangle$ and expanding ϕ as

$$\phi = \langle\phi\rangle + h. \tag{2.27}$$

With the new covariant derivative in Eq. 2.20 we can expand the Lagrangian in Eq. 2.25 around the minimum ϕ and we end up with a Lagrangian of the form

$$\mathcal{L}_{SM} = \mathcal{L}_{QCD} + \mathcal{L}_{EW} + \mathcal{L}_{Higgs} + \mathcal{L}_{Yukawa}, \tag{2.28}$$

$$\begin{aligned}
\mathcal{L}_{SM} \quad &= \frac{1}{2}(\partial_\mu h)^2 + \frac{1}{2}\mu^2 h^2 - \lambda\langle\phi\rangle h^3 \\
&-\frac{\lambda}{4}h^4 + \underline{\frac{1}{4}g^2\langle\phi\rangle^2 B_\mu^2} + \frac{1}{4}g^2\langle\phi\rangle B_\mu^2 h \\
&+\frac{1}{4}g^2 B_\mu^2 h^2 + \underline{\frac{1}{4}g'^2\langle\phi\rangle^2(\vec{T}.\vec{W}_\mu)^2} + \frac{1}{2}g'^2\langle\phi\rangle^2(\vec{T}.\vec{W}_\mu)^2 h^2 \\
&+\frac{1}{2}g'^2\langle\phi\rangle^2(\vec{T}.\vec{W}_\mu)^2 h^4 + \sum_{i,j=1}^{9}\psi_i y_{ij}\psi_j h + \underline{\langle\phi\rangle\sum_{i,j=1}^{9}\psi_i y_{ij}\psi_j} \\
&+\text{Gluonic field} + \mathcal{L}_{kinetic}.
\end{aligned} \tag{2.29}$$

The underlined terms above are quadratic in the field, which are interpreted as mass terms for the corresponding SM field. The last underlined term contains the mass terms for the SM fermions, which is quadratic in the fermion fields and is multiplied by the VEV and corresponding Yukawa coupling. The second underlined term corresponds to the origin of mass for gauge bosons. Here the VEV has been added to the Lagrangian and upon diagonalizing the 2x2 matrix, one of the eignevalues is zero and

corresponds to the photon while the other is non-zero and corresponds to the massive gauge bosons in the broken theory:

$$W_\mu^\pm = \frac{1}{\sqrt{2}}(W_\mu^1 - iW_\mu^2),$$

$$Z_\mu = \cos\theta_W W_\mu^3 - \sin\theta_W B_\mu,$$

and

$$A_\mu = \cos\theta_W B_\mu + \sin\theta_W W_\mu^3,$$

where $\theta_W = \tan^{-1}(\frac{g}{g'})$ is called the Weinberg angle [18]. We get the mass of vector bosons from

$$M_Z = \frac{1}{2}\langle\phi\rangle\sqrt{g^2 + g'^2}, \tag{2.30}$$

$$M_Z = \frac{1}{2}\langle\phi\rangle g, \tag{2.31}$$

and

$$M_A = 0. \tag{2.32}$$

We generalize the mass terms for all vector bosons V_μ with

$$\mathcal{L}_m = \frac{1}{2}V_\mu \mathbf{M}^2 V^\mu, \tag{2.33}$$

Where the mass matrix $\mathbf{M}^2$ is

$$\mathbf{M}^2 = \frac{v^2}{4}\begin{bmatrix} g'^2 & 0 & 0 & 0 \\ 0 & g'^2 & 0 & 0 \\ 0 & 0 & g'^2 & -gg' \\ 0 & 0 & -gg' & g^2 \end{bmatrix}. \tag{2.34}$$

All mass eigenstates mentioned in the Lagrangian of Eq. 2.29 are obtained by diagonalizing $\mathbf{M}^2$. The mass of the resulting bosons and the zero mass of the photon are exactly observed in nature.

This mechanism of introducing mass in a gauge invariant way is called the Higgs Mechanism [16], named after Peter Higgs, who along with Englert, and Bourt first described the mechanism in a relativistic context. The resulting field h is called the Higgs field and the excitation state is called the Higgs boson whose mass is equal to $\mu\sqrt{2}$. The Higgs boson was discovered with the Large Hadron Collider(LHC) in 2012 [13]. This discovery completed the Standard Model. The overall process of generating masses in a gauge invariant way is what the Higgs mechanism brings to the standard model. It incorporates the spontaneous breaking of the $SU(2)_L \times U(1)_Y$ symmetry to a $U(1)_{EM}$ symmetry and generates masses for all SM particles in a gauge invariant way, which is a requirement for a quantum field theory to be renormalizable or self-consistent and allows for solutions that are sensible and free of infinities.

2.3 Shortcoming of the Standard Model

Despite an excellent agreement between the SM and almost all experimental measurements concerning elementary particles, the SM is not the final theory of everything. For one thing the SM does not include gravity in any way. Additionally some ob-

servations are beyond the scope of the SM to explain. For example there is no dark matter candidate within the SM. The standard model can't tell why there are exactly three families of leptons and quarks. It does not fully explain as to why there is more matter than antimatter. There is also the fine-tuning problem [19] in the standard model. The fine-tuning problem is where quantum loop corrections to the Higgs mass term cancel each other in miraculous way to keep the Higgs mass low and stable.

Take gravity for example; it was the first force understood and it is known to have influence over very large distances. It is however, very poorly understood at short distances, the domain of the particle physics. At the microscopic level the gravitational force is very much weaker than any of the other forces so is typically ignored when trying to describe the physics of fundamental particles, which are close to massless when compared to the Plank mass ($\sim 10^{19}$ GeV). No modern day colliders (the LHC collision energy is about 10^3 GeV) or for that matter possible future collider can reach anywhere near the Plank scale, so ignoring the effects of gravity in particle collisions is justified.

From a wide spectrum of astrophysical data, it is observed that baryonic matter accounts for 5% of the universe while dark matter accounts for about 26%, The rest of the energy density is in the form of a mysterious force called dark energy, which acts like anti-gravity and is responsible for the observation of the accelerated expansion of the universe [20]. If dark matter is composed of particles they must be stable, massive, and weakly interacting. The neutrino is the one SM particle that could be considered a candidate for dark matter, however, hot dark matter (hot here meaning that they would be moving close to the speed of light) have been ruled out as dark

matter candidates from astrophysical observations [21].

Almost all SM propagators and vertices are proportional to the original parameters of the theory. This means if tree-level parameters are small, original parameters will stay small. The underlying reason is symmetry. Symmetries protect parameters from being too big even if the symmetry is broken. Essentially, gauge boson masses are protected by gauge symmetry and fermion masses are protected by chiral symmetry. The only particle's mass that is not protected against higher order correction is the Higgs boson. There are basically two contributions to the Higgs mass; the bare mass parameter m_0 and quantum corrections. The latter when summed together with the bare mass, results in the observed mass. In real experiments we do not measure the bare mass. We split self energy (effective mass due to interactions between the particles and its system of particles) into a finite and a divergent part. The finite part is the bare mass and the divergent part is a correction to the bare mass. So, the measured mass, expressed in terms of the bare mass and the correction is

$$m_H^2 = m_0^2 + \delta m_C^2. \tag{2.35}$$

Out of many possible loop corrections to the Higgs boson mass, the largest correction comes from the heaviest fermion, the top quark. This contribution is proportional to the Yukawa coupling y, as

$$\delta m_C^2 \propto -|y|^2 \Lambda^2. \tag{2.36}$$

In the Standard model, the Yakawa coupling is not related to any other interaction. There are no other diagrams to cancel this divergence. If a very large renormalalization parameter μ is chosen, the Higgs mass doesn't survive re-normalization, which means that its value is not definite and can take on any value whatsoever. However,

with the recent observation of the Higgs boson with a mass of 125 GeV, we know that the Higgs boson exists and has a finite mass. But our best theory, the SM, does not predict the mass of the Higgs. The Higgs mass is not protected by a symmetry, it can in fact, take on any value up to the Planck mass at 10^{19} GeV. This riddle is still unsolved in the standard model and is known as the Hierarchy Problem.

Moreover, there is a huge difference between fermion masses. For example, the electron is about 200 times lighter than the muon and 3500 times lighter than the tau while in the SM, neutrinos are massless. It is now an experimentally established fact that neutrinos have a mass. It is not clear if the neutrino masses would arise in the same way that the masses of other fundamental particles do in the Standard Model.

These issues alone motivate us to look for new physics beyond the Standard Model. There are many other models and theories that provide some solutions to problems of the Standard Model. In the next section we will discuss one possible class of theories that builds on lessons learned from the SM and provides a natural fix to the many problems mentioned above.

2.4 Super Symmetry (SUSY)

In previous sections we have encountered symmetry arguments that can have a tremendous role in the successful construction of a theory. It is a firmly established fact that almost all of the possible fundamental symmetries are preserved by the SM. The only remaining symmetry not exploited by the SM is the symmetry between the fermions and the bosons. The fundamental difference between fermions and bosons is spin. Supersymmetry is essentially a symmetry between the bosons and fermions.

We can think of an operator $\hat{Q}$ whose action is

$$\hat{Q}\,|Fermion\rangle = |Boson\rangle\,, \tag{2.37}$$

$$\tag{2.38}$$

$$\hat{Q}\,|Boson\rangle = |Fermion\rangle\,. \tag{2.39}$$

Those spinors are intrinsically complex objects. Q and $Q^\dagger$ are symmetry generators and fermionic operators. As $|Boson\rangle$ and $|Fermion\rangle$ states differ by spin $\frac{1}{2}$, the fermionic operator Q itself carries spin $\frac{1}{2}$ and we can find Q following an algebra of anti-commutation relations:

$$\left\{Q, Q^\dagger\right\} = P^\mu, \tag{2.40}$$

$$\{Q, Q\} = 0, \left\{Q^\dagger, Q^\dagger\right\} = 0, \tag{2.41}$$

and

$$[P^\mu, Q] = 0, [P^\mu, Q^\dagger] = 0, \tag{2.42}$$

where P^μ is the four-momentum generator of space-time.

In a supersymmetric theory, all single particle states like $|F\rangle$ and $|B\rangle$ are combined into single objects called super multliplets. Each supermultliplet contains both bosons and fermions, which have the same gauge charges. In the SM there are no particles that share all of their quantum numbers and are of the same mass but differ by 1/2 spin. So in the SUSY framework there are predicted to be twice as many particles as we currently observe. If supersymmetry was an unbroken theory then the masses of the SUSY partner would be identical to the mass of the SM counterpart. Because we do not observe SUSY partners the symmetry must be broken by some mechanism at

some high-energy scale such as in the early stages of the evolution of the universe.

SUSY Nomenclature: All bosonic SUSY partner names are preceeded by an "s" in their name. For ferminoic SUSY partners an "ino" is attached to the end of their name. We end up with amusing names for particles. The name of the SUSY partner of any quark will be "squark" and is represented by a tilda above the symbol. For example the SUSY partner of the top quark (t) will be the stop ($\tilde{t}$). Similarly the W boson will get it's partner the Wino ($\tilde{W}$). Another category of SUSY particles are the neutralinos, which consist of the photino, Higgsino, and the Zino. The charginos are linear combinations of the charged Wino and charged Higgsinos.

2.4.1 SUSY Lagrangian

To consider SUSY as a serious replacement for the SM, we have to start by making supermultliplets that preserve SM symmetries and rules. So we create "chiral supermultliplets" combining Weyl fermions [22] with complex scalar particles and "gauge supermultiplets" by combining gauge bosons and Weyl fermions. To deal with unequal dimensions of fields in the chiral and gauge supermultiplets, we introduce auxiliary fields "F^a" and "D^a" such that,

$$\mathcal{L}_F = F^a * F^a \tag{2.43}$$

and

$$\mathcal{L}_D = \frac{1}{2} D^a D^a. \tag{2.44}$$

The "F" and "D" have no kinetic term. The next step in creating SUSY multiplets is to introduce a superpotential to specify interactions of the supermultiplets. As in the SM, we start with fermions that are now chiral supermultiplets labeled with indices i

and j. The Lagrangian for the scalar (ϕ_i), fermion (ψ_i), and auxiliary (F_i) fields and their interaction terms, provided that the Lagrangian can be renormalized, takes the form,

$$\mathcal{L}_{chiral} = (-\frac{1}{2}W^{ij}\psi_i\psi_j + W^i F_i) + \text{c.c}, \tag{2.45}$$

with

$$W^{ij} = \frac{\partial^2 W}{\partial\phi_i\partial\phi_j}, W^i = \frac{\partial W}{\partial\phi_i}.$$

W is a superpotential of the form

$$W = \mathcal{L}^i\phi + \frac{1}{2}M^{ij}\phi_i\phi_j + \frac{1}{6}y^{ijk}\phi_i\phi_j\phi_k,$$

where M^{ij} is the fermion mass term, y^{ijk}, known as the Yukawa interaction. Finally L^i are the parameters with dimension of $[mass]^2$, which affects only the scalar potential part of the Lagrangian.

Similarly, the Lagrangian for the gauge supermultiplet is written as:

$$\mathcal{L}_{gauge} = -\frac{1}{4}F^a_{\mu\nu}F^{\mu\nu a} + i\lambda^{\dagger a}\bar{\sigma}^\mu\Delta_\mu\lambda^a + \frac{1}{2}D^aD^a, \tag{2.46}$$

where,

$$F^a_{\mu\nu} = \partial_\mu A^a_\nu - \partial_\nu A^a_\mu + gf^{abc}A^b_\mu A^c_\nu$$

is the usual Yang-Mills field strength, and

$$\Delta_\mu\lambda^a = \partial_\mu\lambda^a + gf^{abc}A^b_\mu\lambda^c.$$

A^a_μ is the covariant derivative for the gaugino field and transforms as

$$A^a_\mu \to A^a_\mu + \partial_\mu \Lambda^a + g f^{abc} A^b_\mu \Lambda^c, \tag{2.47}$$

where λ^a is the two-component gaugino with an index a that runs over all Weyl fermion adjoint representations of the gauge group.

U(1) Transformation: As in the SM, we want the theory to be gauge invariant. This means that we will get an interacting theory through gauge bosons just like the SM. But because of SUSY, we also get the superpartners of the gauge bosons called gauginos along with some D terms and their interactions. We have to take into consideration the interaction between gauge and chiral supermultliplets. The details are worked out in [23] and give

$$F_i = -W_i^*,\ F^{*i} = -W^i \text{and } D^a = -g\phi^* T^a \phi, \tag{2.48}$$

with T^a as the generator of the group, g being the gauge coupling, and W are the gauginos. With these terms in Eqs. 2.45, 2.44, and 2.43, we can see the complete Lagrangian with trilinear and quadratic interactions introduced by auxiliary fields F and D.

2.4.2 SUSY Breaking

One of the motivations that led to supersymmetry was the hierarchy problem. This can be turned around and used to explore how SUSY is broken. SUSY required us to introduce scalar fields for each SM Dirac fermion that cancel out the quadratic divergent terms in the Higgs mass. A simple way to generalize this statement is to show that loop corrections for fermions and bosons are of opposite sign. The intro-

duction of the SUSY field helps to cancel the divergent terms in the Higgs mass as their contribution to the correction are opposite in sign. If SUSY was an unbroken symmetry then there will be no mass difference between the SM particles and SUSY particles. This lead to the situation where theories in SUSY can't explain mass at all.

So the effective Lagrangian can be broken into two parts; one ($\mathcal{L}_{susy}$) part that contains gauge and Yukawa interaction and preserves SUSY invariance and another softly broken term that contains the mass and interaction terms:

$$\mathcal{L} = \mathcal{L}_{susy} + \mathcal{L}_{soft}. \tag{2.49}$$

Sometimes, this type of breaking of SUSY is called "soft" supersymmetry breaking [23]. Soft breaking consists of several possible terms:

$$\mathcal{L}_{soft} = -\frac{1}{2}M_a\tilde{\lambda}_a\tilde{\lambda}_a - \frac{1}{6}b_{ijk}\tilde{f}_i\tilde{f}_j\phi_k - \frac{1}{2}b_{ij}\tilde{f}_i\tilde{f}_j - m_{ij}^2\tilde{f}_i^*\tilde{f}_j, \tag{2.50}$$

where,

$\tilde{\lambda} \rightarrow$ super partner field of gauge bosons

$\tilde{f} \rightarrow$ super partner field of fermions.

$\phi \rightarrow$ scalar field

The first term in the equation represents the gaugino mass, the last two terms represent the sfermions mass, and the second term indicates the triple-scalar interaction. These terms break SUSY preserving R-parity [1]. In the upcoming section, we will

[1] R-parity is a symmetry acting on the Minimal Supersymmetric Standard Model (MSSM) and defined as:

$$P_R = (-1)^{3B+L+2s}$$

where s is spin, B is a baryon number, and L is a lepton number. All Standard Model particles have R-parity of {+1} while supersymmetric particles have R-parity of {-1}.

expand generic soft breaking terms within the context of the Standard Model.

2.4.3 Minimal Supersymmetric Standard Model

Names		spin 0	spin $\frac{1}{2}$	$SU(3)_C, SU(2)_L, U(1)_Y$
squarks, quarks	Q	$(\tilde{u}_L\ \tilde{d}_L)$	$(u_L\ d_L)$	$(3, 2, \frac{1}{6})$
(3 families)	$\bar{u}$	$\tilde{u}_R^*$	$u_R^\dagger$	$(\bar{3}, 1, -\frac{2}{3})$
	$\bar{d}$	$\tilde{d}_R^*$	$d_R^\dagger$	$(\bar{3}, 1, \frac{1}{3})$
sleptons, leptons	L	$(\tilde{\nu}, \tilde{e}_R)$	(ν, e_R)	$(1, 2, -\frac{1}{2})$
(3 families)	$\bar{e}$	$\tilde{e}_R^*$	$e_R^\dagger$	$(1, 1, 1)$
Higgs, higgsinos	H_u	(H_u^+, H_u^0)	$(\tilde{H}_u^+, \tilde{H}_u^0)$	$(1, 2, +\frac{1}{2})$
	H_d	(H_d^-, H_d^0)	$(\tilde{H}_d^-, \tilde{H}_d^0)$	$(1, 2, -\frac{1}{2})$

Table 2.2: Chiral supermultiplets in the Minimal Supersymmetric Standard Model. The spin-0 fields are complex scalars, and the spin-$\frac{1}{2}$ fields are left-handed (with subscript L) and right-handed (with subscript R) two-component Weyl fermions.

The MSSM is an extension to the Standard Model. The word minimal refers to the model with the smallest number of new particle states and interactions consistent with existing theoretical model and experiments. Table 2.2 and 2.3 form the particle list for MSSM. Note that there are two Higgs supermultiplets. The second Higgs supermultiplet is required to give "up" type fermions their mass after spontaneous symmetry breaking. It also prevents gauge any anamoly [23] [24]. The superpotential

Names	spin $\frac{1}{2}$	spin 1	$SU(3)_C, SU(2)_L, U(1)_Y$
gluino, gluon	$\tilde{g}$	g	(8, 1, 0)
winos, W bosons	$\tilde{W}^{\pm}, \tilde{W}^0$	$W^{\pm}, W^0$	(1, 3, 0)
bino, B boson	$\tilde{B}^0$	B^0	(1, 1, 0)

Table 2.3: Gauge supermultiplets in the Minimal Supersymmetric Standard Model.

for MSSM is written as

$$W_{mssm} = \bar{u} Y_u Q H_u - \bar{d} Y_d Q H_d - \bar{e} Y_r L H_d + \mu H_u H_D. \tag{2.51}$$

To describe MSSM completely, we take the generic soft breaking terms in Eq. 2.50 and express them in terms of the super fields listed in Tables 2.2 and 2.3. All soft breaking terms are [23]:

- **Gaugino mass** $-\frac{1}{2}(M_3 \tilde{g}\tilde{g} + M_2 \tilde{W}\tilde{W} + M_1 \tilde{B}\tilde{B})$
- **SFermion masses** $-\tilde{Q}^{\dagger} \hat{M}^2_{\tilde{Q}} \tilde{Q} - \tilde{L}^{\dagger} \hat{M}^2_{\tilde{L}} \tilde{L} - \tilde{\bar{u}} m^2_{\tilde{\bar{u}}} \tilde{\bar{u}}^{\dagger} - \tilde{\bar{d}} m^2_{\tilde{\bar{d}}} \tilde{\bar{d}}^{\dagger} - \tilde{\bar{e}} m^2_{\tilde{\bar{e}}} \tilde{\bar{e}}^{\dagger}$, where mass matrices are 3×3 Hermition matrices.
- **Triple scalar coupling** $-(\tilde{\bar{u}} \hat{a}_u \tilde{Q} H_2 + \tilde{\bar{d}} \hat{a}_d \tilde{Q} H_1 + \tilde{\bar{e}} \hat{a}_e \tilde{L} H_1 + c.c$ where scalar couplings are 3×3 complex matrices
- **Higgs masses and mixing** $-m^2_{H_2} H_2^{\dagger} H_2 - -m^2_{H_1} H_1^{\dagger} H_1 - (b H_2 H_1 + \text{c.c.})$

These four sets contain 107 unknown parameters along with four from the Higgs doublet making for a total of 111 parameters in the MSSM. These 111 parameters are

unspecified and can only be extracted from measurements. This vast parameter space is impossible to explore, at least for the time being.

2.4.4 Minimal Super Gravity(mSUGRA)

By imposing some assumptions on MSSM, we can reduce the number of the parameters to some workable number. These assumptions reduce the SUSY breaking parameters from above one hundred to five. Essentially, the idea is that at very high energies (the GUT and Strong unification scale of 10^{19} GeV), all super partners become mass degenerate. This assumption allows us to set the mass of all sfermions to a single value at very high energy and we do the same for the gaugino mass and the higgsino mass. Imposing additional constraints such as CP-violation [25] and inserting small off-diagonal elements in the mass matrix in Eq. 2.50 leads to the universality of SUSY breaking. Under this universality, all mass matrices are proportional to the unit matrix, triple scalar couplings are proportional to the Yukawa matrix, and breaking parameters have no complex phase. The five remaining parameters after the mSuGRA assumptions are:

$$M_1 = M_2 = M_3 = M_{\frac{1}{2}}, \tag{2.52}$$

$$\hat{m}^2_{\tilde{Q}} = \hat{m}^2_{\tilde{L}} = \hat{m}^2_{\tilde{\bar{u}}} = \hat{m}^2_{\tilde{\bar{d}}} = \hat{m}^2_{\tilde{\bar{e}}} = M_0^2 \hat{1}, \tag{2.53}$$

$$M_0^2 = m^2_{H_1} = m^2_{H_2}, \tag{2.54}$$

$$a_u = A_0 Y_u, a_d = A_0 Y_d, a_e = A_0 Y_e, \tag{2.55}$$

and

$$b = B_0 \text{sign}\mu, \tag{2.56}$$

where signμ is a sign of μ SUSY conserving Higgsino mass parameter and takes the value ± 1. Given the small parameter space, this model can be extrapolated from the experimental data. Also, since off-diagonal elements in the mass matrix are non-zero in the SM and in CP-violation we allow a complex phase in the quark-mixing matrix. Moreover, the theoretical motivation for grand unification is mainly aesthetical. These two assumptions are weakly motivated from theoretical point of view, the reason to go along with these assumptions is practicality.

2.4.5 Simplified Model Spectra (SMS)

A simplified model is defined by a set of hypothetical particles and a sequence of their production and decay. In the simplified models under consideration, only the production process for two primary particles is considered. Each primary particle can undergo a direct decay or a cascade decay through an intermediate new particle. Each particle decay chain ends with a neutral, undetected particle, denoted LSP (lightest supersymmetric particle) and one or more SM particle. The masses of the primary particle and the LSP are free parameters. The simplified models with a T1-, T3-, and T5-prefix are all models of gluino pair production and those with a T2- and T6-prefix are models of squark-antisquark production. In this document, only the T1tttt and T2tt models are considered for interpretation. Simplified models will be described in Chapter 5. Detailed description of the SMS is presented in [26].

This analysis focuses on a search for supersymmetric particles produced in two specific decay chains associated with a simplyfied SUSY model: gluino and stop pairs produced at a center of mass energy of 13 TeV in proton-proton collisions. Furthermore, our search assumes the stop and gluino masses are around 2 TeV, with

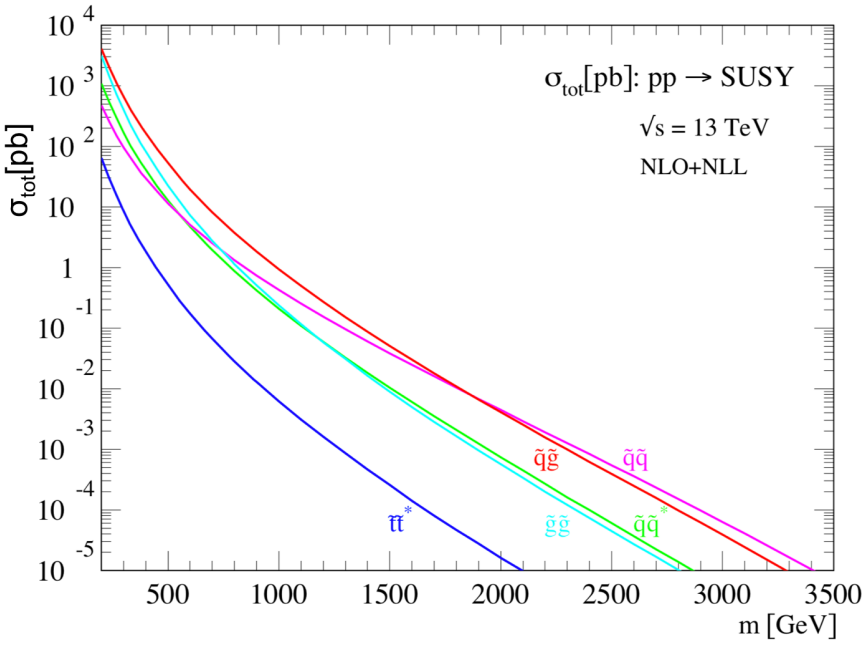

Figure 2.3: NLO+NLL production cross sections for the case of equal degenerate squark and gluino masses as a function of mass at $\sqrt{s} = 13$ TeV [4]

an inclusive cross section of approximately 10^{-2} pb. Theoretical expectations for SUSY cross sections as a function of mass at 13 TeV are shown in Fig. 2.3. This is the mass scale the LHC is capable of exploring.

CHAPTER 3

Experimental Setup

3.1 Collider Physics

The basic procedure for performing experiments in high energy physics is very simple. We accelerate subatomic particles to very high energies that are then collided to produce new and exotic states of matter that subsequently decay into ordinary subatomic particles. We capture these decay products with particle detectors, which are then used to recreate the existence of new forms of matter in order to study their properties. There are two types of colliding particle experiments: Fixed target and colliding beams experiments. Fixed target experiments are comparatively simple in terms of setup and an operation. Here, a beam of particles is incident on a static target and the detectors are placed in the forward region behind the target to collect the decay products resulting from the collision. In colliding beam experiments there are two beams that are collided head to head or at slightly offsetting angles. In this case, the detectors need to surround the entire collision zone to collect all of the decay products resulting from the collision. The detectors usually cover the entire solid angle of 4π. Elaborate accelerator physics is needed to focus the beams and aim them to collide head on or at some small angle. These conditions makes collider beam experiments more complicated.

Despite those complexities, collider beam experiments are preferred as they yield a higher Center of Mass (CoM) energy $\sqrt{s}$. In fixed target experiments the CoM energy, available to discover new physics, is related to the beam energy as:

$$\sqrt{s} = \sqrt{2E_{\text{beam}}M_{\text{target}}}. \tag{3.1}$$

In colliding beam experiment the CoM energy is

$$\sqrt{s} = 2E_{\text{beam}}. \tag{3.2}$$

This implies that at very high energies $E_{\text{beam}} \gg M_{\text{target}}$, colliding beam experiments yield much higher CoM energies than would fixed target experiments. An example of this is the Large Hadron Collider (LHC) with a beam energy of 6.5 TeV for each beam. It is the highest energy ever achieved for any particle accelerator and is just short of the designed energy of 7 TeV. In practice it is somewhat difficult to accelerate protons to multi-TeV energies in an accelerator of reasonable size given that very high magnetic field bending magnets are needed to steer the beams around the accelerator. High magnetic fields, on order of 8 Tesla, are difficult to produce and require very sophisticated superconducting magnets. In the past decades many particles and new discoveries have been made at machines of ever increasing energy scales. These discoveries have led to a better and more complete picture of the inner workings of our universe but still leave many unresolved issues, particularly with the Standard Model. In search of solutions to these unresolved problems we expect to probe new and even rarer processes. These rare processes imply low cross sections, inversely related to $\sqrt{s}$, and thus require high energy and high luminosity machines such as the LHC.

The use of a circular collider with a proton beams is motivated primarily by a desire to reach the high energies needed to probe new physics. While a high energy electron-positron collider would provide a much cleaner environment, given that electron/positrons are point-like objects and not composite particles consisting of many partons, the energy losses in steering charged particles with tiny masses around a

circular beam line would make for a hopelessly impractical accelerator for rings of reasonable size (R). Recall, that energy losses are proportional the inverse of the mass (M) of the beam particles to the 4^{th} power as:

$$[\frac{E}{M}]^4 \frac{1}{R}, \tag{3.3}$$

where R is the radius of the collider, E is the beam energy, and M is mass of colliding particles. With protons being nearly 2000 times heavier than an electron, there will be much less energy loss in hadron colliders than electron colliders. We could presumably use linear colliders but these are fraught with many problems with beam focusing and much reduced luminosity associated with a single-shot crossing. We would also need to build a very long and straight accelerator to reach the high energies needed.

Another important consideration is the "rate"; that is, the total number of collisions. Even with high $\sqrt{s}$, if the collision rate is low, production of new particles is significantly suppressed. The expected event rate is dependent on mainly two quantities, the luminosity $\mathcal{L}$ and the cross section σ

$$\frac{dN}{dt} = \mathcal{L}\sigma. \tag{3.4}$$

To achieve the intense beams needed to search for a new physics, we need to have higher luminosity, which is given by

$$\mathcal{L} = \frac{\kappa_b N_B^2 f \gamma}{4\pi\epsilon_n \beta^*} F, \tag{3.5}$$

where γ is a Lorentz factor, f is the revolution frequency, κ_B is the number of particle bunches, N_p is the number of particles per bunch, ϵ_n is the normalized transverse

beam emittance, β^* is the beta function at the Interaction Point (IP), and F is the geometric luminosity reduction factor due to the crossing angle at the IP. The total cross section is calculated from the Parton Distribution Function (PDF) as

$$\sigma_{total} = \sum_{i,j} \int dx_i \int dx_j f_i(x_i, Q^2) f_j(x_j, Q^2) \hat{\sigma}_{ij}, \tag{3.6}$$

where $\hat{\sigma}_{ij}$ is a partonic cross section and the PDF is the probability of finding the given parton i with momentum fraction x_i and the energy scale Q. The colliding partons, the constiuents particles that make up a hadron, carry different momentum fractions x_1 and x_2, the effective CoM energy is

$$\sqrt{s_{eff}} = \sqrt{s x_1 x_2}. \tag{3.7}$$

3.2 Large Hadron Collider

The Large Hadron Collider (LHC) is a proton-proton (pp) collider located at the European Organization for Nuclear Research (CERN) just outside of Geneva, Switzerland. The circumferences of the accelerator ring is 26.7 km (17 mi) and 100 m (roughly 300 ft) below ground. The first operation of the LHC was in 2011 when proton beams collided at a CoM energy of 7 TeV followed by $\sqrt{s} = 8$ TeV in 2012. After a temporary shutdown (also known as long shutdown-1) [27], the beam energy was increased to $\sqrt{s} = 13$ TeV, the highest CoM energy achieved by any particle accelerator in the world. The goal of the LHC experiments ranges from detailed understanding of partonic substructure to a search for the existence of new physics phenomena. To reaffirm that future discoveries are in fact new physics, the LHC experiments will make more precise measurements of already established Standard Model parameters

and look for deviations from established measurements. The anticipated discoveries not only require highly energetic collisions but also intense beams that produce many interactions.

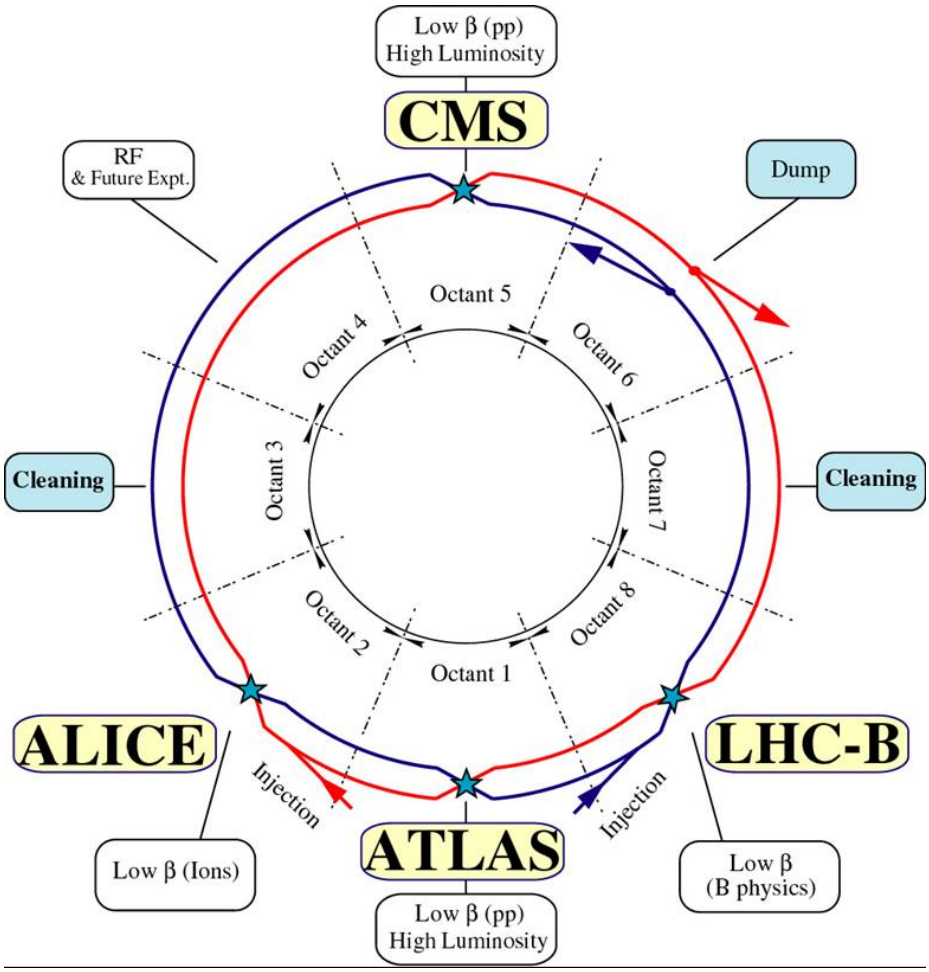

Figure 3.1: The Large Hadron Collider layout [5]. Four stars in the ring represent four interaction points.

At ideal design conditions, the LHC can collide proton-proton beams at $\sqrt{s} = 14$ TeV and with a luminosity of 10^{34} cm^{-2}s^{-1}. These performance parameters are for the high luminosity experiments namely, the Compact Muon Solenoid (CMS) and the ATLAS [28]. For other experiments like TOTEM and LHCb, the LHC will operate

at a lower luminosity of 10^{29} cm^{-2}s^{-1} and 10^{32} cm^{-2}s^{-1} respectively. In Fig. 3.1, the LHC and the experiments at the LHC rings are shown. The desired luminosity is reached with 2808 (κ_B) proton bunches. Each bunch consists of 1.2×10^{11} protons (N_p) at a bunch spacing of 25 ns or 8 m.

To ensure different beam magnetic field polarities in dipoles, the beams are run in two separate vacuum pipes with separated dipole fields provided by large 8.33 Tesla magnets. These main dipoles (MB from Magnet Bend) and the main quadrupoles (MQ) are the principle components of the LHC. There are 1232 MBs, that fill out more than 2/3 of the ring. These magnets direct the beams around the LHC's track. The remaining tunnel length is filled with the 392 MQs. The task of MQs is to focus the beams. Both MB and MQ magnets are wound with a NbTi copper-stabilized superconductors operating in a bath of superfluid helium, at 1.9 K. A Rutherford cable with 15.1 mm width is used to protect the coils, which carries a very high current of 13 kA. A description of the final features of the LHC main magnets can be found in [29, 30, 5]. There is only a 130 m section of the ring where the beams share the same pipe. A pictorial representation of the LHC accelerator complex is shown in Fig. 3.1.

The record setting beam energy of 6.5 TeV was achieved after much effort was expended on tuning and configuring many of the components around the accelerator complex. The particle acceleration sequence, starting from injection of the first beam, running of the beams in different accelerators, and routine testing between two runs consumes nearly one hour for the LHC turnaround. After residual gas scattering and interactions reduce luminosity, there will be 6-12 hours of data taking per day. With 200 days of running, the LHC provides about 100 fb^{-1}of data to CMS and ATLAS

in a year. This thesis includes a subsample of the delivered integrated luminosity corresponding to 35 fb^{-1} collected between March 2015 and January 2017.

3.3 Compact Muon Solenoid (CMS)

The Compact Muon Solenoid (CMS) is one of the two general purpose detectors in the LHC ring designed for precise measurement of decay products from the p-p collision. The entire detector weighs approximately 12,500 tonnes and occupies 3600 cubic meters in volume. It is 21.6 m long with a diameter of 14.6 m. It is situated about 100 m underground near the French city of Cessy. The location of the detector in the LHC ring is shown in Fig. 3.1. The operation and maintenance of the detector is carried out by the CMS collaboration, which is comprised of approximately 3000 participants from 199 institutions in 43 countries.

CMS employs both a right-handed Cartesian coordinate system as well as a HEP coordinate system (the Lorentz invariant spherical coordinate system). The origin is centered at the interaction point with $\hat{y}$ pointing vertically up, $\hat{x}$ pointing radially inward towards the center of the LHC and $\hat{z}$ pointing in the counter-clockwise direction of the beam pipe as viewed from above. The azimuthal angle ϕ is measured in the $x-y$ plane from the $x-$axis and the polar angle θ is measured from the $z-$axis. The variables listed below describe the position and momentum of any track in the detector,

$$p_T = \sqrt{(p_x)^2 + (p_y)^2}, \tag{3.8}$$

$$\eta = -\ln[\tan(\theta/2)], \tag{3.9}$$

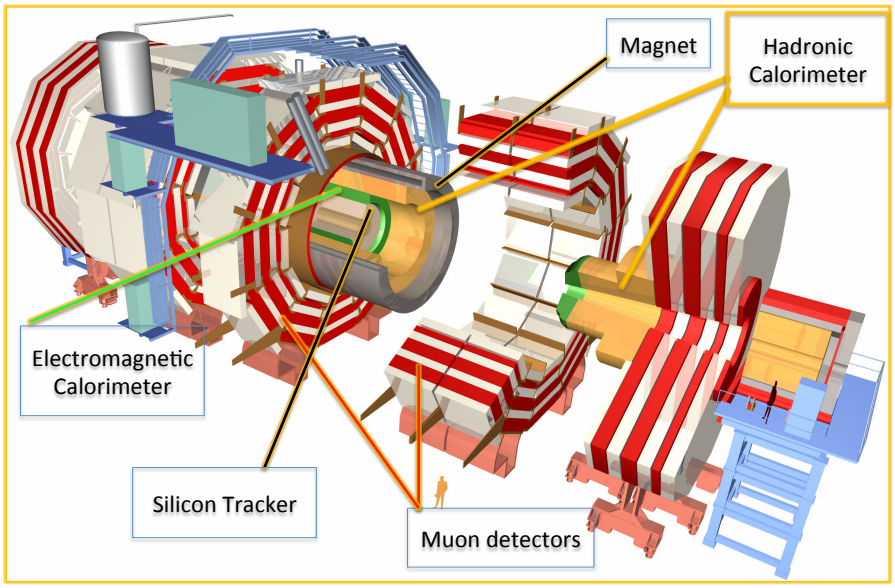

Figure 3.2: 3D view of Compact Muon Solenoid Detector. Typical human size in picture is for scale [6].

and

$$\phi = \quad \tan^{-1}(p_y/p_x), \tag{3.10}$$

where η is the pseudorapidity[1] and p_T is the transverse momentum.

The major components of the CMS detectors are shown in Fig. 3.2. The four basic elements from inside out are:

- **The Tracking system:** A silicon based tracker with pixel and silicon strip detectors.
- **The Electromagnetic Calorimeter(ECAL):** Made up of lead tungstate $PbWO_4$ scintillating crystals.

[1]Pseudorapidity is the same as the rapidity, Y, for a massless particle. $Y = \frac{1}{2}ln(\frac{E+p_z}{E-p_z})$

- **The Hadronic Calorimeter (HCAL):** A sampling calorimeter with plastic scintillators interspersed with brass. It encapsulates the ECAL and is surrounded by the superconducting solenoid magnet.

- **The Magnet:** The central device around which the experiment is built, is 12.9 m long and generates a 3.8 Tesla magnetic field that is 100,000 times stronger than that of the Earth′s magnetic field.

- **The Muon System:** The outermost part of the detector, optimized to identify and measure the momentum of muons. It consists of three different and complementary detection technologies: The Drift Tube Chambers (DT) in the barrel region, the Cathode Strip Chambers (CSC) in the endcap region, and the Resistive Plate Chambers (RPCs) in both the barrel and endcap regions [31].

3.3.1 Silicon Tracker

The CMS tracker [7, 32] is the innermost of all sub-detectors and the first one particles' decay products encounter as they emerge from the collisions. The main task of the tracker is to successfully measure the track momentum of charged particles. When charged particles traverse through the tracking system, they bend due to the presence of the strong magnetic field from the superconducting solenoid magnet. Figure 3.3 shows a quarter view of the CMS tracker. At design luminosity, nearly 1000 particles are produced in every 25 ns bunch crossing. So the innermost layer must be capable of disentangling millions of particle tracks per mm^2 each second. Moreover, particles like τ leptons and those with b and c quarks travel a few millimeters before decaying so their decay products are displaced from the interaction point or the primary vertex. Those decay vertices are known as secondary vertices. To separate the two types of interaction vertices, an excellent spatial resolution of the tracker is necessary.

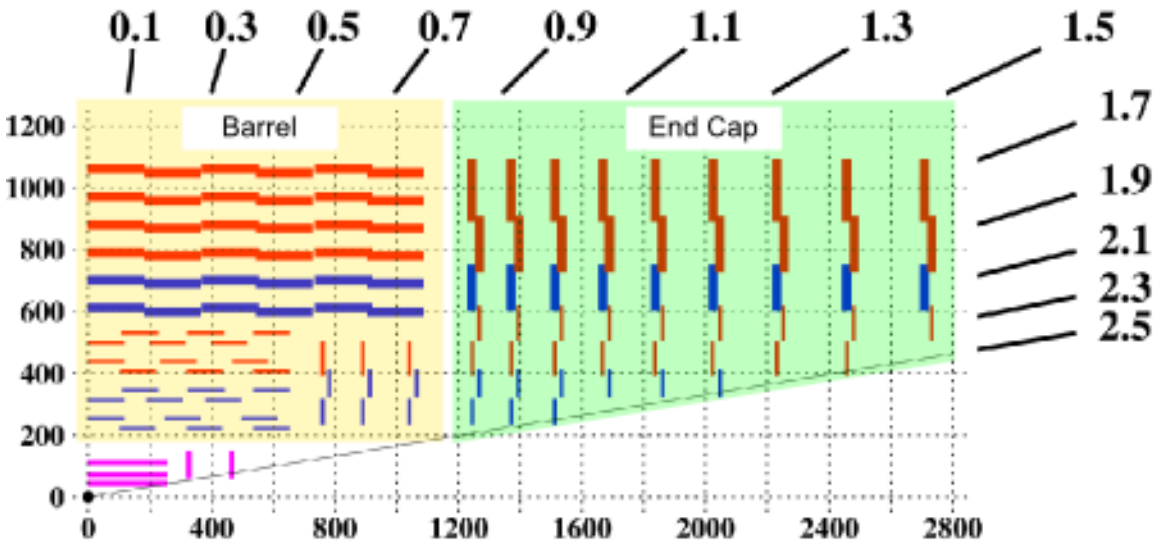

Figure 3.3: Schematic view of $\frac{1}{4}$ of the CMS Tracker when viewed toward the center of the LHC. Barrel region in horizontal lines and Endcap region are vertical lines [7].

The CMS tracker consists of two subsystems; the innermost pixel detectors that extend to a radius of 11 cm from the IP and the outer strip tracker extending up to a radius of 1.2 m. The former consists of 66-million silicon pixels while the strip detector contains nearly 10-million silicon strips. Both combined cover up to pseudo-rapidity $|\eta| < 2.4$ in the central and forward regions of the detector. The inner pixel detector consists of three cylindrical layers. Two endcap disks located at 34.5 and 46.5 cm on either side of the center enclose the pixel detector.

As we move away from the IP, particle occupancy per unit area decreases. So the outer strip detector has a comparatively lower spatial resolution. Switching from a high resolution pixel detector to a lower resolution strip tracker was done as a cost-saving measure. The barrel tracker region is divided into two parts: a Tracker Inner Barrel (TIB) and a Tracker Outer barrel (TOB). The TIB is made up of four layers

using 320 μm silicon sensors and 80-to 120 μm-thick strip pitch. In the TOP, there are six layers and the sensors are thicker (500 μm). The barrel is accompanied by three disks in the Tracker Inner Disk (TID), and nine disks in the Tracker End Cap (TEC) covering $|\eta|$ up to 2.5. The thickness of the sensors is 320 μm for the TID and the three innermost rings of the TEC and 500 μm for the rest of the TEC. Combining all the 66-million pixels and 9.3-million strips, we can get a transverse momentum resolution of

$$\frac{\delta p_T}{p_T} = 0.15 p_T[\ \mathbf{TeV}] \oplus 0.005, \tag{3.11}$$

where $\oplus$ represents sum in quadrature.

3.3.2 Electromagnetic Calorimeter

The tracker measures the momentum of electrically charged particles in the presence of the magnetic field. But neutral particles, like the photon, do not leave a trace in the tracker. The scintillators that make up the calorimeters, absorb the energy of neutral particles and convert it into light. Ultimately, photodetectors, convert the light energy into electrical signals that are then transformed into a digitized format and stored on tape for a subsequent analysis.

The Electromagnetic Calorimeter (ECAL) sits between the tracker and the Hadronic Calorimeter. It is made up of lead tungstate ($PbWO_4$) crystals. When electrons at relativistic energy interact with the crystal, they radiate photons by a process known as the bremsstrahlung [18]. The radiated photon may interact with the material and convert into an electron-positron pair. As more particles are created in the process, their energy decreases. The initial energy of a photon or an electron is the sum of the energy of the particle shower resulting from the bremsstrahlung or e^+e^- production.

Once the ECAL measures the energy deposited from particle showers, this energy is assigned to the incident particle.

The choice of the scintillating materials was inspired by its high density, an efficient transmission of light, and a very short radiation length[2] ($X_0 = 0.89$ cm) so that full absorption of the particle shower is possible with a very small Moliere radius [18] of $R_m = 2.2$ cm allowing the realization of a homogeneous compact calorimeter with high granularity. These properties result in a very good spatial resolution.

The 75,848 crystals are arranged in a central barrel section (EB), with pseudorapidity coverage up to $|\eta| = 1.48$. The crystal are read out by Avalanche Photo Diodes (APD). The nearly 23-cm-thick crystals results in a radiation length of $26X_0$. The endcap (EE) crystals are read out with Vacuum Photo Triodes (VPT) and cover $|\eta| = 3$. The EE detector is located 3.15 m away from the IP and each endcap weighs 12 tonnes and occupies 1.5 m^3 of volume. The endcap crystal are about 22 cm long and correspond to $25X_0$ radiation lengths. Crystals are projective and positioned slightly off-pointing (3°) relative to the IP to avoid cracks aligned with particle trajectories. The endcaps consist of two Dees, with 3,662 crystals in each Dee. The total crystal volume is 11 m^3 and the weight is 92 tonnes. Ten of the crystals are mounted into a thin-walled fiberglass cavity called a submodule. Groups of submodules make a module and the modules are combined to make the supermodules. There are 36 supermodules in the barrel region. A preshower detector (PS), based on a lead absorbers and a silicon-strip sensors, is placed in front of the endcaps at $1.6 < |\eta| < 2.6$, and improves the photon-π° separation. A schematic view of the calorimetry and tracking system is

[2]The radiation length is the distance a particle travels before it loses 1/e of its energy

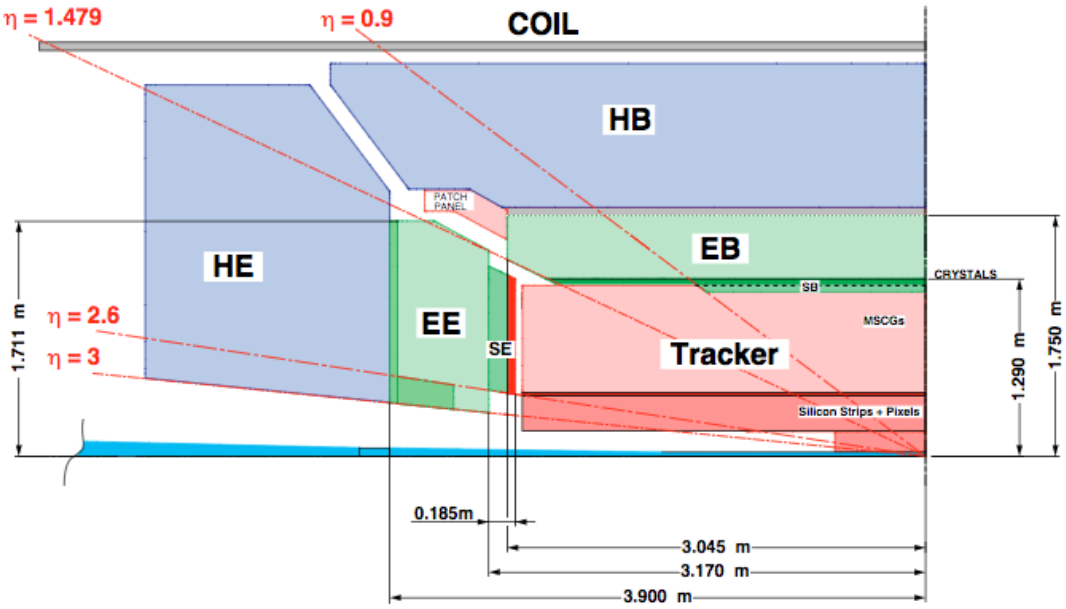

Figure 3.4: Schematic view of one quadrant of the calorimetry and tracking system [8].

shown in Fig. 3.4

The performance of the supermodules were measured with test beams. The energy resolution is determined by fitting a Gaussion function to the reconstructed energy distribution and has been parameterized as a function of energy as

$$\frac{\sigma}{E} = \frac{S}{\sqrt{E}} \oplus \frac{N}{E} \oplus C, \tag{3.12}$$

where $\oplus$ represents sum in quadrature. In the first term, $S = 0.028$ is a stochastic fluctuation of light yields. In the second term $N = 0.12$ is electronic noise and $C = 0.003$ in the third term represents the calibration error. The ECAL supermodule energy resolution $\frac{\sigma_E}{E}$ is shown in Fig. 3.5.

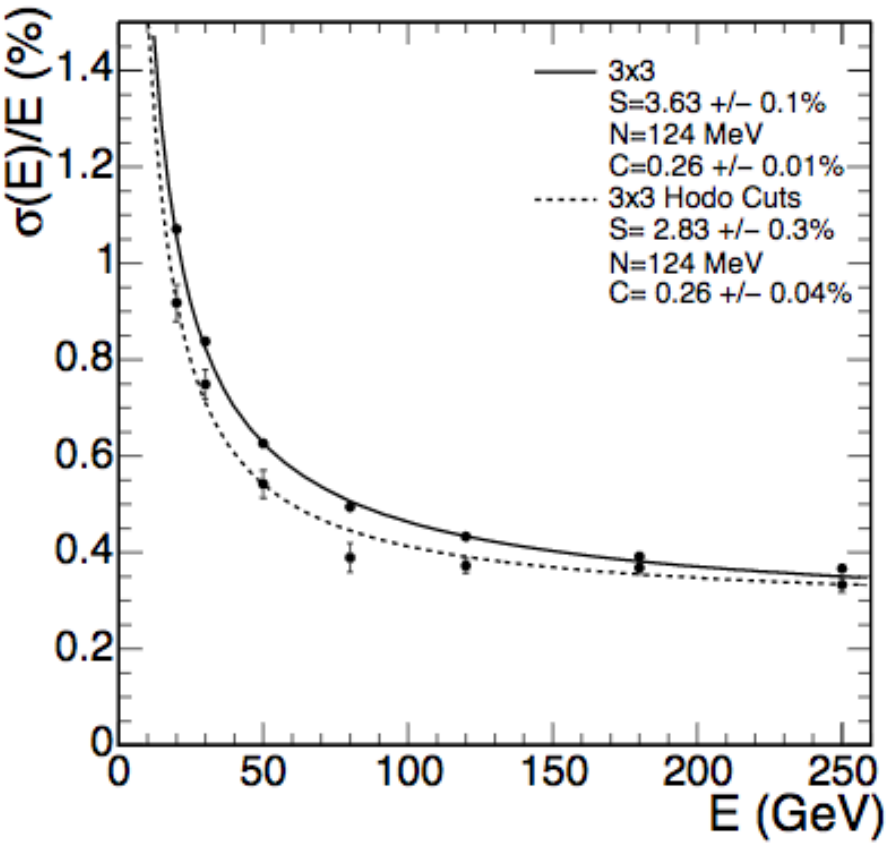

Figure 3.5: ECAL supermodule energy resolution $\frac{\sigma_E}{E}$ as a function of electron energy as measured from the test beam [6].

3.3.3 Hadronic Calorimeter

The hadronic calorimeter sits between the ECAL and the outer superconducting solenoid magnet. It aims to quantify hadronic activity and missing transverse energy ($E_{\mathrm{T}}^{\mathrm{miss}}$). Hadrons, like electromagnetic objects, interact with materials and form particle showers. Both the Hadronic Barrel (HB) and Hadronic Endcap (HE) are made up of non-magnetic materials (copper alloy and stainless steel) as they experience a high magnetic field of four Tesla. The central hadron calorimeter is a sampling calorimeter: it consists thick plastic scintillator tiles inserted between copper absorber plates. The absorber plates are 5-cm thick in the barrel and 8-cm thick in the endcap. The

metal bars cause the hadrons to shower and the showers deposit their energy in the plastic scintillators that follow the bar. The scintillator then converts the energy to light which is then collected by photodetectors. The HCAL subdetectors and their locations are shown in Fig. 3.6.

The HB and HE are hermetically joined and together and they cover up to an $|\eta| = 1.4$. The HE extends coverage up to $\eta = 3.0$. The forward (HF) overlaps with a sections of the HE. The HF extends coverage up to a pseudorapidity between 2.9 to 5.0. The HF is located 11.2 m away from the IP. In the barrel region, the interaction length ranges between $5\lambda_0$ and $10\lambda_0$ and in the endcap region the radiation length is $10\lambda_0$.

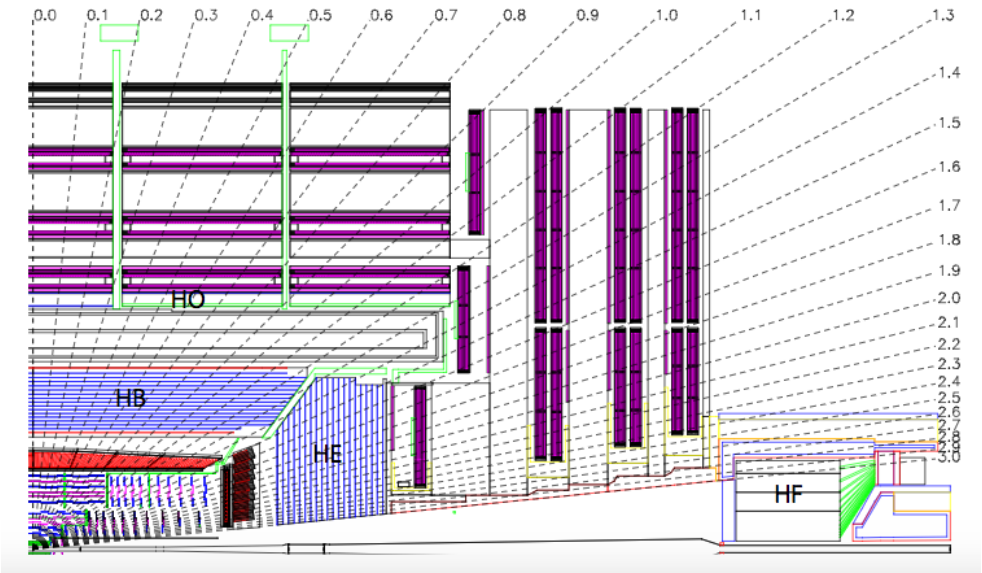

Figure 3.6: A section view of the CMS detector showing the HCAL subsystems (HB, HE, HO, and HF). Dashed lines shows range of pseudorapidity [9].

The HB consists of 32 towers divided into two half barrels. Each of a half barrels consist of 18 individual wedges 20° wide in ϕ. Each wedge consists of alternating lay-

ers of flat brass-alloy absorber plates and plastic scintillator tiles with an innermost layer made up of stainless steel. Those 36 wedges are matched geometrically with 36 supermodules of the ECAL. Each scintillator tile in a tower has $\Delta\eta \times \Delta\phi$ dimension of 0.08×0.087. The endcaps of the HE consist of 14 η towers with 5° segmentation. The HE is composed entirely of brass absorber plates and scintillators in an 18-fold ϕ-geometry matching that of the barrel calorimeter. The thickness of the plates is 78 mm, while the scintillator thickness is 3.7 mm, hence reducing the sampling fraction. There are 19 active plastic scintillator layers. The forward calorimeter is made of steel absorbers and embedded radiation-hard quartz fibers, which provide a fast collection of Cherenkov light. The outermost (HO) layer contains scintillators with a thickness of 10 mm, which lies outside of the vacuum tank of the coil and cover $|\eta| = 1.26$. They sample energy from penetrating hadronic showers leaking through the rear of calorimeters and serves as the tail catcher after the magnet coil. The HO improves the E_T^{miss} resolution of the calorimeter. Details of design and performance of different parts of the HCAL can be found in [33, 9, 34, 35]

The best way to gauge performance of the HCAL is to look at the jet energy resolution and missing transverse energy resolution. The jet energy resolution as a function of E_T is determined from the three subdetectors of the HCAL by granularity of sampling. Fig. 3.7 illustrates the energy resolution in different parts of the HCAL.

3.3.4 Superconducting Solenoid

The superconducting solenoid magnet system [36] divides the inner sub-detectors from the outer muon system. The magnet is very important to the functionality of detector. Its large dimension (12.9 m in length and 6 m in diameter) along with the superconducting coil made up of Niobium Titanium provides the CMS with a

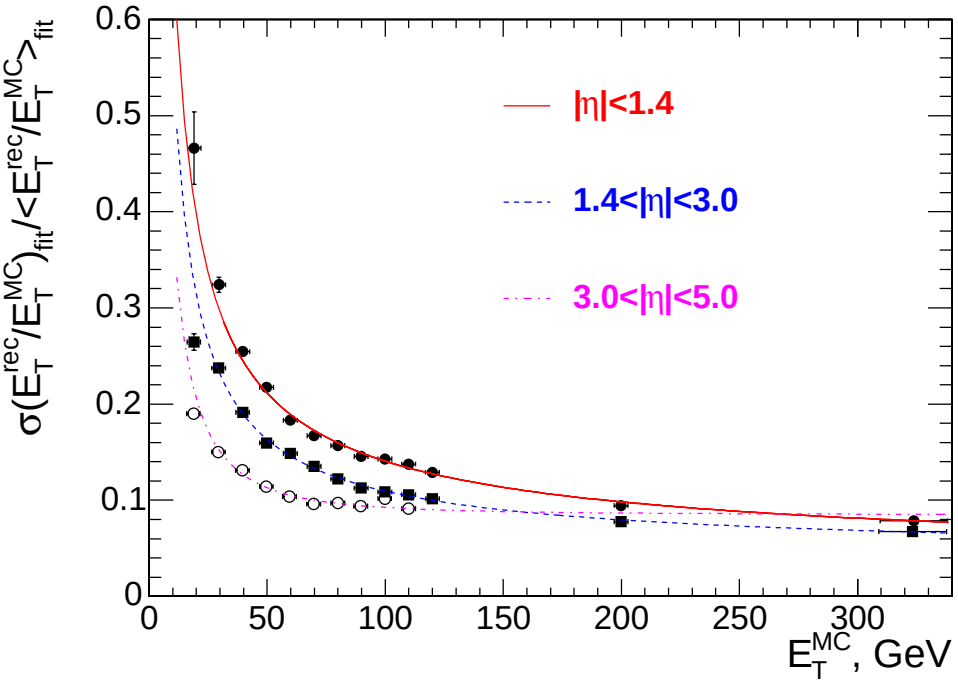

Figure 3.7: The jet transverse energy resolution as a function of the simulated jet transverse energy for barrel jets ($|\eta| < 1.4$), endcap jets ($1.4 < |\eta| < 3.0$) and very forward jets ($3.0 < |\eta| < 5.0$).

very strong magnetic field of 3.8 Tesla. The magnet provides the bending power for charged tracks thus allowing a determination of track momentum. The superconducting coils are cooled by liquid helium that is supplied via a multistage cryogenic system, which maintains the temperature of the coil through which a current of 19.5 kA flows, to 3.2 K.

3.3.5 Muon System

The Compact Muon Solenoid, as the name suggests is optimized in the reconstcution of muons from proton-proton collisions. Out of particles that can be observed in the detectors like electrons, protons, photons, charged pions, kaons and muons, the muons are relatively easy to identify and they do not shower in the subdetectors. They do not interact hadronically and are stable with respect to the LHC energies. Moreover, the muons do not lose any significant part of their energy when traversing through subdetectors as they ionize an atom the least. These features make muons unique in the sense that we can get clean data in an important channels like $H \rightarrow ZZ \rightarrow 4\mu\mu$. The Muon System (MS) identifies muons and also measures their momenta. By design, The MS has a cylindrical barrel and two endcaps and consists of three subsystems; Drift Tubes (DT), cathode strip chambers (CSC) and resistive plate chambers (RPC) [6]. All three and their pseudo-rapidity coverage is shown in Fig. 3.8.

- **Drift Tubes (DT)**: The Barrel Detector consists of 250 chambers organized in 4 layers inside the magnet return yoke, at radii of approximately 4.0, 4.9, 5.9 and 7.0 m from the beam axis. In the barrel region ($|\eta|$ <1.2), where the neutron-induced background is small, the muon rate is low and the residual magnetic field in the chambers is low, DT chambers are used.

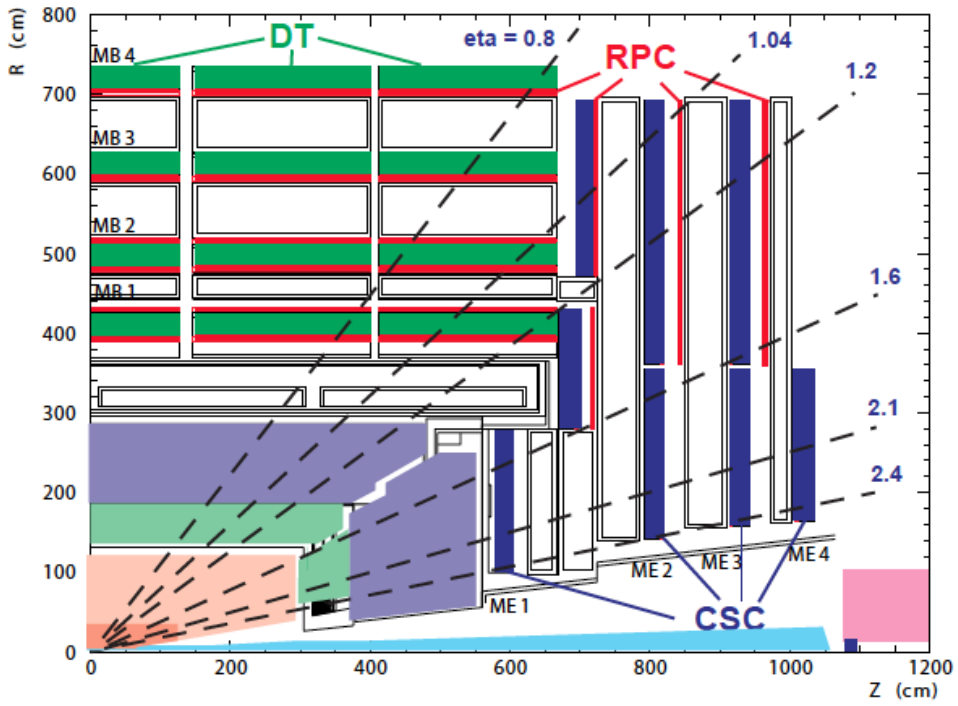

Figure 3.8: Layout of one quarter of the CMS muon system for initial low luminosity running [6].

- **Cathode Strip Chambers (CSC)**: 468 CSCs are deployed in the two endcap regions and cover the region up to $|\eta| < 2.4$ where the muon rate, as well as the neutron-induced background rate, is high, and the magnetic field is also high.

- **Resistive Plate Chambers (RPC)**: The RPCs extend in both the barrel and the endcap regions and are operated in an avalanche mode to ensure good operation at high rates (up to 10 kHz/cm^2). There are 36 chambers mounted in each of the two rings in each of the endcap stations.

The muon system itself is capable of determining the momentum of muons with a p_T of up to 1 TeV with a resolution of 15% in the barrel and 40% in the endcaps. Information from the muon system is combined with that of the tracker to achieve a resolution to 5%. The $\frac{\Delta p_{\mathrm{T}}}{p_{\mathrm{T}}}$ averaged over ϕ and η varies in p_{T} from (1.8$\pm$0.3(stat)%

at $p_{\mathrm{T}} = 30$ GeV to (2.3±0.3(stat)% at $p_{\mathrm{T}} = 50$ GeV [37].

3.3.6 Triggers and Data Acquisition System (DAQ)

The trigger system and data acquisition system [38] are two essential component of the CMS data recording process. There are one billion proton-proton collisions per second and most of them carry no valuable information and should be discarded. The decision making process in rejecting noise and writing of interesting data to the disk must be very quick and efficient. Due to finite resources available, only on the order of 10^3 events per second can be stored. So in order to reject 10^6 events per second, the CMS deploys a two-level trigger system.

The Level-1 (L1) Trigger system is the first step in selecting the most interesting events for further analysis. This reduces the event rate by a factor of 10^3. It uses local information from the muon system as well as the calorimeters and is based on customized programmable electronics. L1 uses trigger primitives (energy deposits in the calorimeters and hits in the muon chambers) to analyze the collision immediately after each bunch crossing to compute the four-vectors of $\mu/e/\gamma$, transverse momentum of all particle flow candidates as well as missing energy $E_{\mathrm{T}}^{\mathrm{miss}}$. The L1-trigger has a small window of 3 μs. The trigger rate for the L1-trigger is given by the expression:

$$\text{Trigger Rate} = \frac{\text{Number of events fired}}{\text{Number of zero biased events}} * \text{LHC frequency} * \text{nBunches} \quad (3.13)$$

where the LHC frequency is 11245.6 Hz, the expected number of bunches are 2592 in 2017, and the zero-bias rate is the product of LHC frequency and the number of bunches. The L1 trigger allows up to a 100 kHz online rate. Events passing the L1

trigger are sent to the second trigger called the High Level Trigger (HLT).

Events passing the L1-trigger are the baseline for the HLT. Depending on the physics objectives, there are a number of HLT paths. In Chapter 5 we will discuss HLT paths used in this analysis. It uses information from all subdetectors, including the tracker, with full granularity. It determines physics objects more precisely than the L1 trigger but when compared with offline reconstruction it is less precise. So during the analysis, we measure the efficiency with reconstructed data. The HLT trigger is implemented mostly in software and reduces the rate to $\mathcal{O}(1)$ kHz. An event is sent to the mass-storage system at the CMS Tier 0 computing center. The computing center is located in the CERN Data Center.

CHAPTER 4

Particle Flow Algorithm and Event Reconstruction

4.1 Introduction

The identification and reconstruction of all event-level observables and particles from the collisions requires an optimal combination of information from different subdetectors. The basic data elements from the detector (particle tracks, calorimetr clusters) are analyzed to form higher level objects such as particle candidates, jets, and missing transverse momnetum. The CMS Particle Flow (PF) algorithm [39, 40] is responsible for the construction of these higher level objects. We show in Fig. 4.1 a representation of one of the octets of the CMS detector and the various categories of particles as they travel through the octets interacting with the detector elements.

As shown in Fig. 4.1, photons are reconstructed from energy deposited in the ECAL cells as shown by the dashed blue line that terminates in the ECAL. The granularity of the ECAL along with the magnetic field of 3.8 T allows charged particles energy to be separated from the photon energy with excellent energy resolution. Electrons leave a signal in the tracker and deposit their energy in the ECAL cells and are shown with solid red lines. Charged hadrons, represented with solid green lines, are bent in the tracker and deposit their energy in the hadronic calorimeter (HCAL). Neutral hadrons don't leave any trace in the tracker and their energy is abosrbed by the HCAL cells. Muons, represented in Fig. 4.1 with a solid blue line, is the only particle to escape the detecter. In the process, it leaves a signal in the inner tracker, deposits energy in the calorimeters with most of the interaction taking place in the muon chamber. Muons are identified by linking tracks in the inner tracker and the muon chamber and are known as "a global muon". Muon Candidates identified only with a track in the muon system are known as "a standalone muon". Both forms of

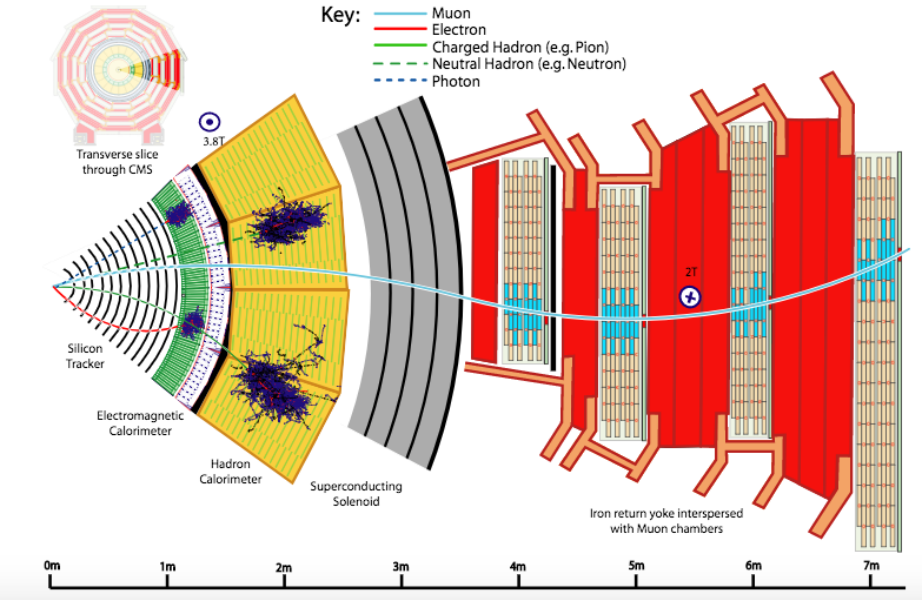

Figure 4.1: Sketch of particles and their interaction with different subdetectors as they traverse through detector.

reconstruction are necessary as the muon system does not provide good coverage in the high η regions and the information from the tracker may not be enough to identify muons. Neutrinos and other weakly interacting particles that escapes detection are inferred from the transverse missing energy, E_T^{miss}, which is defined as the absolute value of the vector sum of all reconstructed particle energy. Charged hadrons, neutral hadrons, and photons are the basic constituents of hadronic jets and hadronic tau decays, and are essential ingredients in the $E_{\mathrm{T}}^{\mathrm{miss}}$. They are the focus in this chapter as the analysis depends heavily on these physics objects. Details of the particle flow algorithm are explained in [10].

The detector does not identify particles itself. It essentially records two types of event signatures: charged particle tracks and calorimeter clusters. For each event, we need complete information of all charged particle tracks and clusters of energy deposits in

the calorimeters. Also, all clusters in the calorimeters must be linked with a charged particle tracks. If calorimeter clusters are from neutral particles, there will be no corresponding tracks associated with them. The method of finding all tracks is discussed in Section 4.1.1, the clustering process is described in Section 4.1.2, and the method of linking tracks and clusters is described in Section 4.1.3. The algorithm to identify particles is presented in Section 4.2. The performance of the algorithm on jets and missing transverse momentum is discussed in Section 4.3.

4.1.1 Iterative Tracking

About two thirds of the energy in a jet is, on average, carried by charged particles. Therefore, measuring the properties of charged particles with the silicon tracker before they reach the calorimeters will provide us with a more accurate determination of the momentum, and thus energy, and the direction and origin of the charged particles. This is important since particles that reach the calorimeters lose energy as they bend in the magnetic field and travel through the silicon tracking system. Also, the calorimeter alone provides very poor information on the direction of charged particles. Therefore, we need tracking information that is efficient with a low mis-reconstructed track rate or fake rates.

To achieve this goal, an iterative-tracking algorithm [41, 42] was adopted in the track reconstruction. First, very tight restrictions are imposed on track seeds. This results in a moderate efficiency with a very low fake rate. The tracks are then re-fit now with hits removed, previously assigned to the track and with looser track seeding criteria. This is done to maintain the high tracking efficiency while keeping the fake rates low. By the end of the third iteration, isolated muon tracking efficiency as high as 99.5% is achieved with a slightly lower efficiency for charged hadrons. The next

two iterations are performed with a relaxed criterion on track origin that allows for the reconstruction of particles originating from a secondary vertex. Such processes include photon conversion, nuclear interaction, and decay of long-lived particles.

4.1.2 Calorimeter Clustering

Clustering in each subdetector of CMS is performed separately except at the Hadronic Forward (HF) calorimeter [43]. This is done to determine the best possible measurement of the direction and energy of neutral particles like photons and neutrons. It also helps to distinguish the energy carried by charged verse neutral particles. Moreover, reconstruction and identification of electrons and Bremsstrahlung photons is carried out by the clustering algorithms. Additionally, charged hadrons missed during track reconstruction are reconstructed and added to the particle flow with calorimeter clusters.

Clustering is done in three steps. First, calorimeter cell energy maxima above a certain threshold are marked as "cluster seeds". In the next step, those seeds grow into "topological clusters". This is done by combining cells with at least a corner in common with a cell already in the cluster and with an energy in excess of a cell threshold set to twice the noise level. Topological cluster gives rise to the number of "particle-flow clusters" equal to number of "seeds". The energy of each cell is shared with all particle-flow clusters according to the cell-cluster distance to exploit granularity of calorimeter.

4.1.3 Link Algorithm

A muon can leave a trace on the tracker, clusters on one or more of the calorimeters, and one muon track in the muon system tracker. Similarly, charged hadrons will

have a track in the tracker and a cluster in the HCAL. Moreover, an electron leaves a trace on the silicon tracker and a energy cluster in the electromagnetic calorimeter. An efficient link procedure that connects together the deposits of each particle in a sub-detector is desired to avoid possible double counting. For each event, the link algorithm essentially quantifies the link between each pair of elements and produces "particle flow blocks" of elements that are connected directly or indirectly. Typically, a blocks contain one, two, or three elements. These blocks are an input for the particle reconstruction and identification algorithm. The link algorithm quantifies the following three types of links:

- Link between the silicon tracker tracks and and a corresponding calorimeter clusters.
- Link between the HCAL clusters and a corresponding ECAL clusters.
- Link between silicon tracker track and a corresponding muon system track.

4.2 Particle Reconstruction and Identification

A collection of tracks, calorimeter clusters, and a link between them are used as input to the particle flow algorithm and is called as particle a flow block. Particles within the blocks themselves are identified by the particle-flow algorithm. This identification is what gives rise to global objects that are subsequently used for physics analysis. After identifying particles, we remove identified particles from the blocks to avoid double counting.

Muons are identified first to avoid ambiguity with charged hadrons. The global muons are reconstructed from the information with the charged particle track in the silicon

tracker and muon chamber track. The global muon gives rise to a "particle-flow muon" and the corresponding track is removed from the block for further identification. Then follows the more difficult electron reconstruction as a Bremsstrahlung photon emission can cause double energy counting in the calorimeter cluster. At first, tracks in the block are sent for pre-identification. With a Gaussian-Sum Filter [44] fitting, these tracks are followed up to the ECAL clusters and by combining track and calorimeter cluster variables, electrons are identified as a "particle-flow electrons" and the electron tracks are removed from the blocks. Tighter quality criteria are applied to the remaining tracks such that remaining elements subsequently can be constructed as charged hadrons, photons, neutral hadrons or muon in some rare cases. By comparing the momentum of tracks with the energy detected in the calorimeter, we can reconstruct photons from the ECAL cluster and neutral hadrons from the HCAL cluster. The expected muon energy is subtracted from the HCAL and the ECAL clusters' energy. Effective measures are taken for the case where multiple tracks connect to calorimeter clusters or vice-versa. In rare cases, the total calibrated calorimetric energy is still smaller than the total track momentum by a large amount. Additional steps are performed to find the global muon and remaining tracks in the block gives rise to a particle-flow charged hadron. All resulting particles are then used to reconstruct jets, the missing transverse energy $E_{\mathrm{T}}^{\mathrm{miss}}$, and identify taus from their decay products.

4.3 Performance

Performance of particle flow algorithm was studied with events generated by PYTHIA [45] and simulated using the GEANT4-based toolkit [46]. The QCD multijet events were used for jets-performance studies and $t\bar{t}$ samples were used for $E_{\mathrm{T}}^{\mathrm{miss}}$ performance studies.

4.3.1 Jets Reconstruction and Performance

In general, charged particles, photons, and neutral hadrons carry 65%, 25%, and 10% of the jet energy respectively. These fractions ensure that 90% of the jet energy can be reconstructed with good precision by the particle-flow algorithm. About 10% of the energy is reconstructed with the hadronic calorimeter information.

A widely used method to reconstruct jets is clustering. A jet clustering algorithm maps the momenta of the final state particles into the momenta of a certain number of jets. There are two main classes of jet algorithms: sequential recombination algorithms and cone algorithms. The former takes a bottom-up approach: combines particles starting from closest ones, iterates recombination until few objects are left, and then call them jets. The latter takes a top-down approach: find coarse regions of energy flow and find the axis that coincides with the sum of momenta of particles in it. CMS uses one from amongst a class of sequential clustering algorithms called the anti-kT algorithm [47]. In the sequential clustering algorithms, jets can have fluctuating areas in (η, ϕ) space. Due to computational complexities and the jet area not being trivially accessible, experimentalist avoided using this method. But with the availability of sufficient computing resources, an anti-kT algorithm was adopted by the CMS collaboration to cluster jets.

All clustering algorithms use two distance variables. The first variable, the jet distance parameter is $d_{ij} = \min(p_{Ti}^a, p_{Tj}^a) \times \frac{R_{ij}^2}{R}$, where R is the final distance parameter that determines the size of the jet, $R_{ij}^2 = (\eta_1 - \eta_2)^2 + (\phi_1 - \phi_2)^2$ is distance between particle i and j in $\eta - \phi$ space and the label a specifies the type of algorithm: $a = 2$ indicates the kT algorithm [48]; value of $a = 0$ is the case of the Cambridge/Aachen algorithm [49]; and $a = -2$ is the anti-kT algorithm. An another distance param-

eter used is $d_{iB} = p_{ti}$. This distance is the momentum space distance between the beam axis and the detected particle. The distance d_{ij} is dominated by a high p_T in the anti-kT algorithm and the algorithm prefers to cluster high momentum particles first. In CMS, when the distance parameter used is $R = 0.4$ we label these jets as "ak4jets". Jets with distance parameter $R = 0.8$ are also reconstructed and labeled as "ak8jets". These ak8jets are used in this analysis for top tagging purposes.

The performance of the algorithm is gauged by a Monte Carlo method. Monte Carlo generated stable particles, except for neutrinos, give rise to so-called gen-jets. All reconstructed particles are matched with gen-jets in (η, ϕ) space and only those within the distance R < 0.1 are selected. The matching jet efficiency is defined as the fraction of generated jets that give rise to a matched reconstructed jet. The mismatched jet ratio is defined as the fraction of reconstructed jets that do not have a matched generated jet. The matching jet efficiency and the mismatched jet ratio were used to gauge the performance of the algorithm. For a jets with a transverse momentum of 20 GeV, an efficiency close to 80% was achieved and a plateau of more than 99% was achieved for a jets with momentum more than 40 GeV.

4.3.2 $E_{\mathbf{T}}^{\mathbf{miss}}$ Reconstruction and Performance

Stable particles, particles that live long enough to make it through the CMS, detector are mostly captured by the materials that make the CMS detector. Neutrinos and other hypothetical weakly interacting particles are not and instead travel through undetected. These hypothetical particles might be illusive dark matter or supersymmetric particles or any other particle that has not yet been observed in nature. These undetected particles, if they exist, are inferred from the energy imbalance in an event known as missing transverse momentum($E_{\mathrm{T}}^{\mathrm{miss}}$). A precise measurement of $E_{\mathrm{T}}^{\mathrm{miss}}$ is

typically necessary in searches for physics beyond the Standard Model, in particular this one. The particle flow missing transverse energy (pfMET) is defined as the negative vectorial sum over the transverse momenta of all PF particles.

$$\vec{E}_{\mathrm{T}}^{\mathrm{miss}} = -\sum_{i=1}^{N_{patricles}} \vec{p}_{T,i}, \tag{4.1}$$

where $p_{T,i}$ is the transverse momentum of i^{th} particle flow candidate. The performance of the PF reconstruction is determined with a sample of $t\bar{t}$ events by comparing $E_{\mathrm{T,pf}}^{miss}$ and $E_{T,calo}^{miss}$. Fig. 4.2 shows the relative $E_{\mathrm{T}}^{\mathrm{miss}}$ resolution, obtained with a Gaussian fit in each bin of $E_{\mathrm{T,true}}^{\mathrm{miss}}$. The true $E_{\mathrm{T}}^{\mathrm{miss}}$ is derived in a similar manner with all visible generated particles or, equivalently, with all invisible generated particles, like neutrinos and neutralinos.

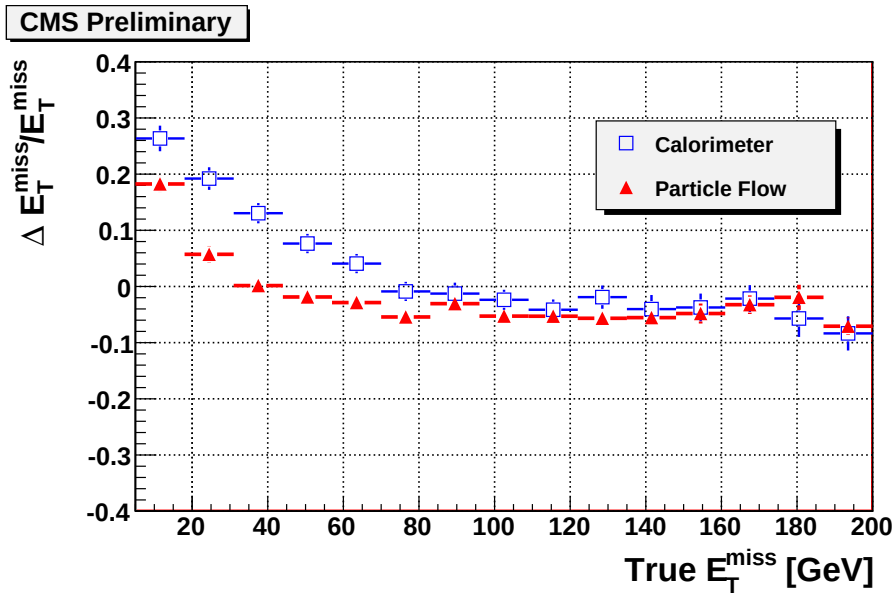

Figure 4.2: Distribution of $(E_{T,reco}^{miss} - E_{T,true}^{miss})/E_{T,true}^{miss}$ as a function of the $E_{T,true}^{miss}$ in the fully inclusive $t\bar{t}$ simulated event sample, for particle-flow reconstruction (solid triangles) and for calorimeter reconstruction (open squares) [10]. The negative value of The missing transverse energy response simply means reconstructed value of $E_{\mathrm{T}}^{\mathrm{miss}}$ from the detector is less that that obtained from generator level information.

4.4 Computing Infrastructure

Each year, CMS collects many petabytes of data. Additionally many more petabytes of Monte Carlo data are generated to complement the raw data created by the LHC. These data need to made accessible 24/7 to the thousands of physics that are members of the collaboration, many of them scattered across the globe. It is simply unrealistic and unsafe to expect the data to be located in a single physical space. The LHC Computing Grid (LCG) [50] is the computing infrastructure used to analyize and process the huge volume of data created by CMS. It is based on a distributed computing model deployed, managed, and maintained by scientist and engineers who are also members of the CMS/LHC community. The LCG consists of four tiers as shown in Fig. 4.3.

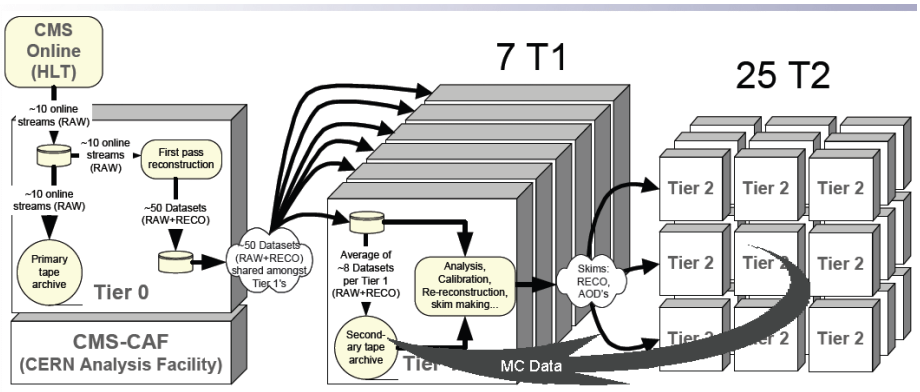

Figure 4.3: Typical structure and standard work flow in CMS computing grid.

- **Tier−0:** Located at CERN, Tier−0 is responsible for the first reconstruction of the full raw collision data sets. This where analysts first look for patterns of discovery. The Tier−0 contributes less than 20% of the grid's total computing capacity. It distributes the raw data and the reconstructed output to the Tier 1s and reprocesses data when the LHC is not running.

- **Tier−1:** There are seven Tier−1 locations throughout the globe. The Tier−1 facilities are also employed in the final level of event reconstruction and calibration and also serve as the main repository of the reconstructed data sets. Each Tier1 facility has its own copy of the full reconstructed data and a portion of the RAW data as a backup to Tier−0.

- **Tier−2:** There are numerous Tier−2 centers around the world, usually located at a university or large computing center. These facilities have substantial computing and storage capacity for user analyses, calibration studies, and Monte Carlo simulations. Tier−2 resources are available to the entire collaboration through grid enabled services.

- **Tier−3:** These are modest facilities at institutes for local use. Such computing is not generally available for coordinated CMS use but is valuable to local physicists.

4.5 CMS Software (CMSSW)

The overall collection of software, generally known as CMSSW is built around a C++ framework known as the Event Data Model. It was built entirely from scratch by CMS physicists and computer professionals. It is extensively used by physicists within CMS for simulation, calibration, reconstruction, and data analysis. The CMSSW framework consists of thousands of modules imbedded in hundreds of libraries that are loaded at runtime by the cmsRun executable. The same cmsRun executable

is used for event reconstruction, data analysis, and Monte Carlo processing. The configurable executable is customized by the user to handle his or her particular data processing needs through job-specific python configuration files. The python configuration file can be customized for types of data, parameter settings, multiple modules, or data processing or analysis procedures, their order of execution, and user specified filters and cuts. The cmsRun executable is extremely lightweight: the only required modules are dynamically loaded at runtime. The CMS Event Data Model (EDM) is organized around the concept of an event. An event is a C++ object container for all RAW and reconstructed data related to a particular collision. During the processing, data are passed from one module to the next via the event and are accessed only through the event. All objects in the event may be individually or collectively stored in ROOT files, and are thus directly browsable in ROOT. This allows tests to be run on individual modules in isolation.

CHAPTER 5

Analysis Description

In supersymmetric particle searches, the stop (top squark), the SUSY partner of the top quark is one of particular interest. For SUSY to provide a natural solution to the hierarchy problem, the mass of the stop should be relatively light. With large a stop mass we would lose naturalness since we would need yet another round of careful adjustment, or fine-tuning, of parameters to cancel quantum corrections to the Higgs mass, a current problem with the standard model. For this analysis, we assume that the stop mass is sufficiently large for it to decay into a top quark and a weakly interacting supersymmetric particle $\tilde{\chi}_1^0$. We target our search on processes that produce a pair of stop quarks in the chain: $pp \rightarrow \tilde{t}\tilde{t}^* \rightarrow t\bar{t}\tilde{\chi}_1^0\tilde{\chi}_1^0$. However, since the analysis is inclusive, other channels can also contribute. Signal models of interest are shown in Fig. 5.1 where we require that the top quarks decay hadronically.

A central feature of the analysis is the top quark tagging algorithm that will be described in Section 5.3. Since more than two thirds of the time a top quark decays hadronically, the decay products are reconstructed as a stream of particles known as "jets" plus an uncharged weakly interacting neutralino $\tilde{\chi}_1^0$ that escapes detection. The typical event signature thus consists of many jets and a large amount of missing energy $E_{\mathrm{T}}^{\mathrm{miss}}$. The analysis is based on exclusive search regions that are a combination of top quark candidates, b-tagged jets [51] , missing transverse energy ($E_{\mathrm{T}}^{\mathrm{miss}}$), the sum of the momentum of all jets (H_{T}) and the transverse mass variable (M_{T2}). A detailed explanation of the variable M_{T2} is presented in Section 5.2. Backgrounds are estimated using well-established data-driven methods.

The diagrams corresponding to the Simplified Model Spectrum (SMS) used to in-

Figure 5.1: Signal models of interest in this search: (left) the stop pair production with the stop decaying into a top quark and a neutralino and (right) gluino pair production where each gluino decays into the on-shell stop and top quark. The stop decay in to the top and a neutralino. The SUSY simplified model topology shown at the left is referred to as T2tt, and that on the right model as a T1tttt.

terpret the results are shown in Fig. 5.1. The left diagram is referred to as T2tt(x,y) and represents direct stop-antistop pair production with "x" and "y" the top squark and $\tilde{\chi}_1^0$ masses respectively. If the gluino is within the reach if the LHC energy in Run 2, gluino-induced processes such as those in the right of Fig. 5.1 would become relevant to the analysis. The right diagram of Fig. 5.1 is called T1tttt(x,y) where "x" and "y" are the gluino and $\tilde{\chi}_1^0$ masses respectively.

5.1 Trigger

In 13 TeV proton-proton collisions at the LHC, a wide range of physics processes are possible. We use triggers to accept events that are interesting to us. This is typically done by collecting data using triggers that accept events if thresholds on certain observable are met. In the trigger these thresholds are reduced to allow further refinement in the offline processing.

In SUSY searches, a large $E_{\mathrm{T}}^{\mathrm{miss}}$ criteria is imposed to suppress the backgrounds. This criteria is also motivated by the fact that SUSY events are expected to contain heavy

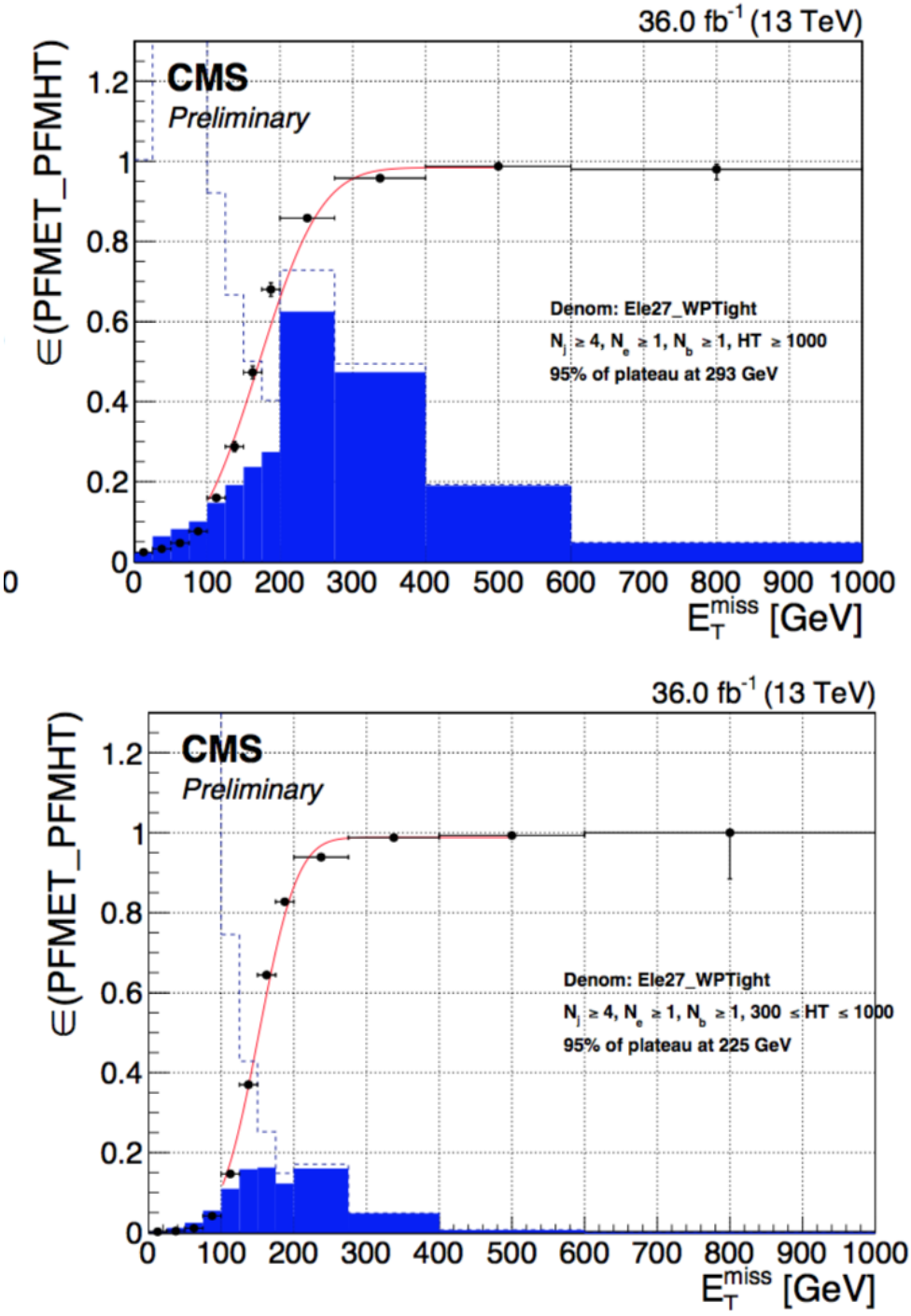

Figure 5.2: The trigger efficiency, denoted by the black point, as a function of the offline $E_{\mathrm{T}}^{\mathrm{miss}}$ for (top figure) $H_{\mathrm{T}} > 1000$ and (bottom figure) $300 < H_{\mathrm{T}} < 1000$. The vertical error bar indicates the statistical uncertainty of the trigger efficiency and the horizontal bar indicates a bin width.

and weakly interacting particles that escape detection in CMS. Also, all hadronic searches require a minimal amount of H_{T} as explained in Section 5.2. In this analysis we use the triggers that are some combination of both $E_{\mathrm{T}}^{\mathrm{miss}}$ and H_{T}. Two conditions must be met in order for triggers to be useful. First, it must be highly efficient in selecting events. Also, it must be possible to make an unbiased measurement of the trigger efficiency.

The probability for triggers to accept events (trigger efficiency) is measured in a sample of events collected by the single-electron trigger. To measure the search trigger efficiency, additional cuts to mimic the pre-selection defined in Section 5.2, are required. The efficiency of the search triggers is measured as a function of the offline $E_{\mathrm{T}}^{\mathrm{miss}}$. In Fig. 5.2, it is seen that the $E_{\mathrm{T}}^{\mathrm{miss}}$ trigger efficiency has a non-trivial dependency on the offline H_{T}. The search trigger efficiencies are measured in the low H_{T} ($300 < H_{\mathrm{T}} < 1000$) and high H_{T} ($H_{\mathrm{T}} > 1000$) region.

5.2 Pre Selection

The search looks at multijet events, with b-jets decaying from top quarks, large $E_{\mathrm{T}}^{\mathrm{miss}}$, and no leptons. Initially, a loose baseline selection is applied in $E_{\mathrm{T}}^{\mathrm{miss}}$, H_{T}, the number of jets (N_{jets}) and $N_{\mathrm{b\text{-}jets}}$. This baseline selection preserves 2-20% of the signal events.

- Filters : As a part of essential data cleaning process at the analysis level, all events must pass all filters that remove detector and beam related noise.

- $N_{\mathrm{jets}} \geq 4$: The stop are produced in a pair and each stop decays to a top and the Lighest Supersymmetric Particle (LSP). In a hadronic decay of a top quark, there will be three jets in the final state. There will be six jets altogether. Not all the jets pass the selection cuts, therefore we require at least four jets. Jets

are reconstructed with the Particle Flow (PF) [39] technique and clustered with the anti-k_{T} algorithm [47] with a resolution parameter R =0.4. Every jet is required to have $p_{\mathrm{T}} > 30$ GeV and $|\eta| < 2.4$. In addition, they must pass the loose jet ID criteria for PF jets. The leading two jets are required to have p_{T} >50 GeV. The high momentum and a central η requirements are motivated by the results of various optimization studies carried out with simulated signal and a background samples. SUSY signal studies predict centrally produced jets with very high momentum.

- $E_{\mathrm{T}}^{\mathrm{miss}} \geq 250$ GeV: We use the particle flow MET with jet energy corrections applied and the cut threshold is constrained by trigger efficiency requirements. As shown in Fig. 5.2, our trigger is very efficient when $E_{\mathrm{T}}^{\mathrm{miss}}$ exceeds 250 GeV.

- $M_{\mathrm{T2}} \geq 200$ GeV: This cut is mainly used to reduce SM background events with a low value of M_{T2}. It specially works well for $t\bar{t}$ events where the M_{T2} shows a kinematic edge around the top quark mass. The M_{T2} variable described in [52], is an extension of the transverse mass variable and is sensitive to pair production of heavy particles, each of which decays into an invisible particle such as a neutralino. From the selected jets in an event, the four-momenta of a three jet system (p^{3-jets}) and a remnant system (p^{Rsys}) along with $E_{\mathrm{T}}^{\mathrm{miss}}$ were used to calculate the M_{T2} assuming the invisible particles are massless. As an example, consider the T2tt channel $pp \rightarrow \tilde{t}\tilde{t}^{*} \rightarrow t\bar{t}\tilde{\chi}_1^0\tilde{\chi}_1^0$. Here M_{T2} is defined as,

$$M_{T2} \equiv \min_{\vec{q}_T^{(1)}+\vec{q}_T^{(2)}=\vec{p}_T} [\max\{m_T^2(\vec{p}_T^{\,t^{(1)}}, \vec{q}_T^{(1)}; m_{\chi_1^0}), m_T^2(\vec{p}_T^{\,t^{(2)}}, \vec{q}_T^{(2)}; m_{\chi_1^0})\}] \ , \qquad (5.1)$$

where the m_T^2 is the transverse mass,

$$m_T^2(\vec{p}_T^{\,t^{(1)}}, \vec{q}_T^{\,(1)}; m_{\chi_1^0}) \equiv m_{t^{(1)}}^2 + m_{\chi_1^0}^2 + 2(E_T^{t^{(1)}} E_T^{(1)} - \vec{p}_T^{\,t^{(1)}} \cdot \vec{q}_T^{\,(1)}) \ . \tag{5.2}$$

From Eq. 5.1, it is clear that M_{T2} is the minimization of the transverse mass provided that the sum of the transverse momenta of both $\tilde{\chi}_1^0$'s is equal to the missing transverse momentum of the event. In the T2tt model mentioned above, we replace quantities represented by superscript (1) and (2) with fully reconstructed top quark (p^{3-jets}) and partially reconstructed top quark (p^{Rsys}) quantities, respectively, if there is only one top in an event. In cases with two or more fully reconstructed top quarks, we replace (2) with fully reconstructed top quark. In Eq. 5.1, $E_{\mathrm{T}}^{\mathrm{miss}}$ corresponds to $\vec{p_T}$ as we assume $\tilde{\chi}_1^0$'s are massless with respect to the stop quark.

In summary, the calculation of M_{T2} starts with an assumption that there is at least one good hadronic top in an event. If there are more than two top candidates in an event, we iterate different combinations of top quarks to get the smallest possible value of M_{T2}. If there is only one top quark reconstructed by the algorithm then we reconstruct the other top quark from the remnant of the event using the b-tagged jet (or the highest p_{T} jet if no b-tagged jet is found) as a seed and the remnant system jet closest to the seed jet with an invariant mass between 50 GeV and the top quark mass of 175 GeV. In case no combination satisfies the invariant mass requirement, we use the seed jet as the only remnant of the other top quark and M_{T2} is calculated by the reconstructed top candidate, the remnant, and the $E_{\mathrm{T}}^{\mathrm{miss}}$.

- $H_{\mathrm{T}} \geq 300$ GeV, with $H_T = \sum_{\mathrm{jets}} p_T$ where the p_{T} is the magnitude. This requirement is also motivated by the fact that a SUSY signal study predicted very high momentum jets. All jets in the H_{T} calculation must meet the same jet selection criteria defined above.

- $N_{\text{b-jets}} \geq 1$, with b-jets identified using the Combined Secondary Vertex(CSV) [51] b-tagging algorithm (CSVM).

- Muon veto: Events with muon candidates satisfying $p_{\mathrm{T}} > 10$ GeV and $|\eta| <2.4$ are removed from the selection.

- Electron veto: Electron candidates are selected using the Electron Physics Object Group (POG)-recommended "Cut Based VETO" selection and events are removed from the selection. Different cut criteria are applied to the barrel and endcap electromagnetic calorimeter region. They are required to have $p_{\mathrm{T}} > 10$ GeV and $|\eta| < 2.5$.

- Angular cut: In order to suppress the background from QCD which tend to produce back to back topologies, we form an angular quantity $\Delta\phi$ defined as the angle between the $E_{\mathrm{T}}^{\mathrm{miss}}$ vector and three leading jets in p_{T}. We require $\Delta\phi$ ($E_{\mathrm{T}}^{\mathrm{miss}}$, $j_{1,2,3}$) > 0.5, 0.5 and 0.3 for the first three leading jets. In QCD processes, the missing energy comes mainly from a under-measurement of the jet energy. So the missing energy vector in the QCD process is closer to the jet direction. Keeping a large angular separation between the jet vector and the missing energy vector help us to suppress the events from the QCD process.

- Isolated track veto: After applying the above mentioned cuts, the remaining background comes from $t\bar{t}$, W+jets events with one $W \rightarrow l\nu$ decay where l can be an electron, muon or tau decaying hadronically. To further suppress these backgrounds, we reject events that have one or more isolated tracks. The

track isolation is calculated from the charged PF candidates consistent with the reconstructed primary vertex ($|dz(PV)| < 0.1$ cm). The requirements are different for muon, electron and charged hadron tracks. For both electron and muon tracks, the isolated track requirements are: $p_{\mathrm{T}} > 5$ GeV, $|\eta| < 2.5$ and relative isolation less than 0.2. For charged hadron tracks, the p_{T} requirement is raised to be at least 10 GeV and the relative isolation value to be less than 0.1. To retain more signal, thus improving our signal-to-background event discrimination, events with one isolated track, as defined above, are only rejected if they satisfy

$$m_T(tk, E_T^{miss}) = \sqrt{2p_T^{tk}E_T^{miss}(1 - \cos\Delta\phi} < 100 \text{ GeV}, \tag{5.3}$$

where p_T^{tk} is the transverse momentum of the track and $\Delta\phi$ is the azimuthal separation between the track and the $E_{\mathrm{T}}^{\mathrm{miss}}$ vector.

Comparisons between all SM background samples combined were compared with the signal scaled to total data yields after the baseline cut in the bin of all search variables as shown in Figs. 5.3 and 5.4. The backgrounds are represented by the color filled histogram stacked on each other. The black dot represent data points. The colored solid lines represent enhanced signal points. It is clearly seen in Figs. 5.3 and 5.4 that in the bins with a relatively large number of entries in all search variables that the signal are well differentiated from the backgrounds.

The events passing the baseline selection are classified into search regions defined in terms of N_{tops}, $N_{\text{b-jets}}$, $E_{\mathrm{T}}^{\mathrm{miss}}$, H_{T}, and M_{T2}. All search variables were combined to make 84 exclusive search bins. Bins with $N_{\mathrm{tops}} \geq 3$ and $N_{\text{b-jets}} \geq 3$ are more sensitive to the T1tttt channel more than the T2tt channel. This is because with more than

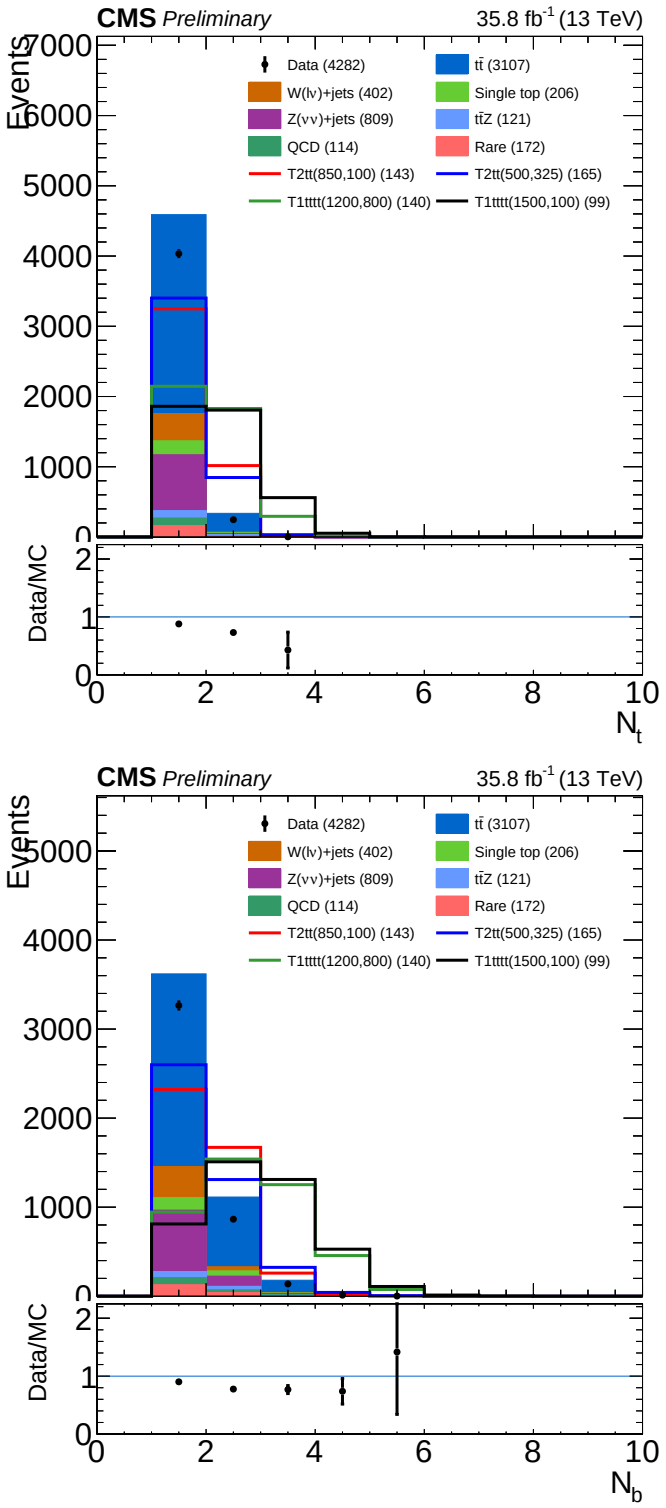

Figure 5.3: Comparisons of various signal models with total SM backgrounds for search variables N_{tops} (top), $N_{\text{b-jets}}$ (bottom). All simulated signals and background samples were scaled to data. The scale is included in the legend for the signal points.

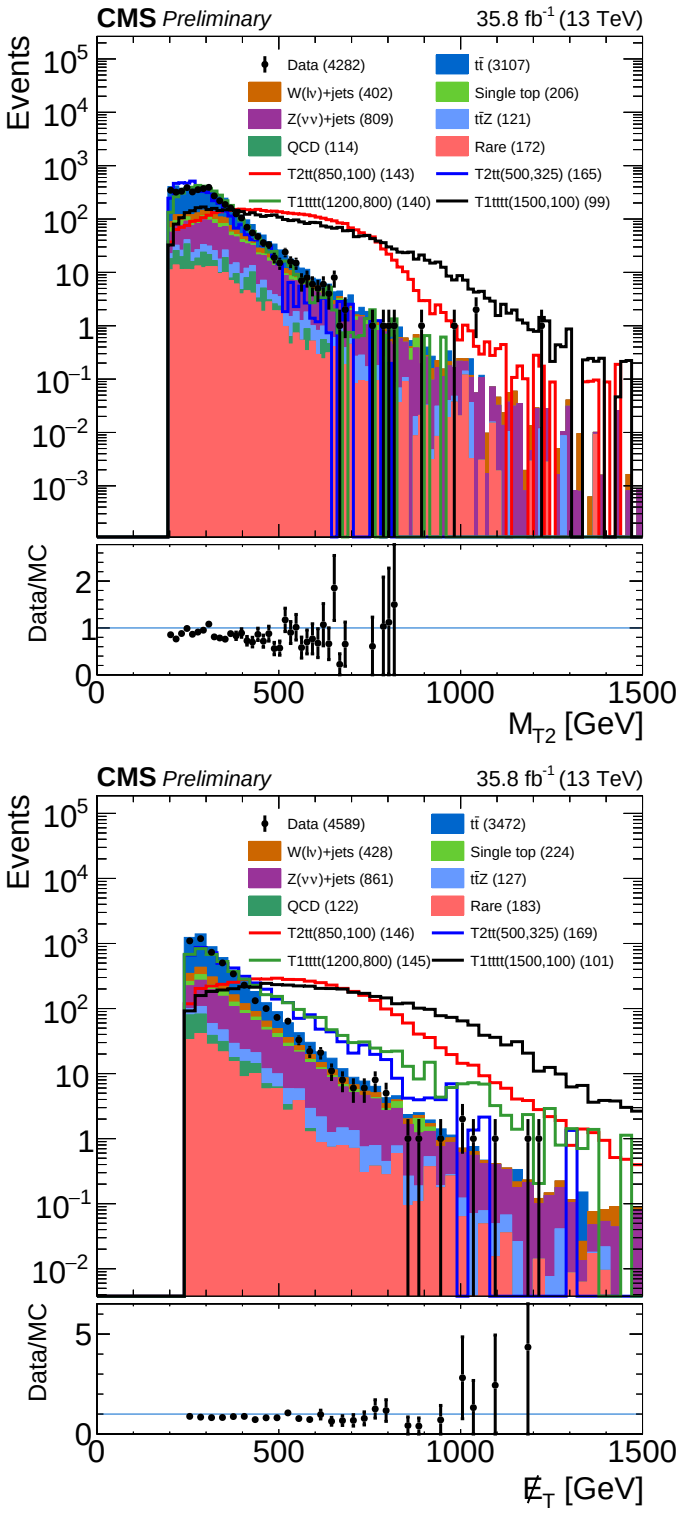

Figure 5.4: Comparisons of various signal models with total SM backgrounds for search variables M_{T2} (top) and $E_{\mathrm{T}}^{\mathrm{miss}}$ (bottom) . All simulated signals and background samples were scaled to data.The scale is included in the legend for the signal points.

two top quarks, we can not define M_{T2} clearly. During the construction of those bins, M_{T2} was replaced by H_{T}. A series of significance scans in the dimension of H_{T}, $E_{\mathrm{T}}^{\mathrm{miss}}$, and H_{T} were performed to study the search bin optimization. All search bins are shown in Fig. 5.5.

5.3 Top Quark Reconstruction and Identification

Depending upon the signal model, there are two or more top quarks produced in the final states. These top quarks can be produced with a wide range of transverse momentum p_{T}. If the mass of the neutralino is small, the top quark will receive a significant boost while a high mass neutralino will produce top quarks with low boost. Moreover, large numbers of particles sharing the initial energy results in a wide p_{T}-spectrum. So a good top tagging algorithm must be efficient in identifying a top quark over a large range of p_{T} and capable of tagging more than one top in a single event.

If the top quark is highly boosted, all the decay products of the top quarks end up in the localized area of the detector and are reconstructed as "fat-jets" or "ak8jets" with relatively large cone parameter ($\Delta R \sim 0.8$). This happens if the top quark has $p_{\mathrm{T}} > 400$ GeV. In this scenario, the top quarks are reconstructed with a very high efficiency and a low fake rate.

When the top quark is lightly boosted, all top quark decay products are identified as individual jets (ak4jets with $\Delta R \sim 0.4$). In this scenario, we have to construct top quarks from individual jets. Reconstruction of the top in this scenario is a bit more complicated as many jets from the different processes can mimic the top decay. So to reduce backgrounds while keeping the fake rate low and maintaining a high

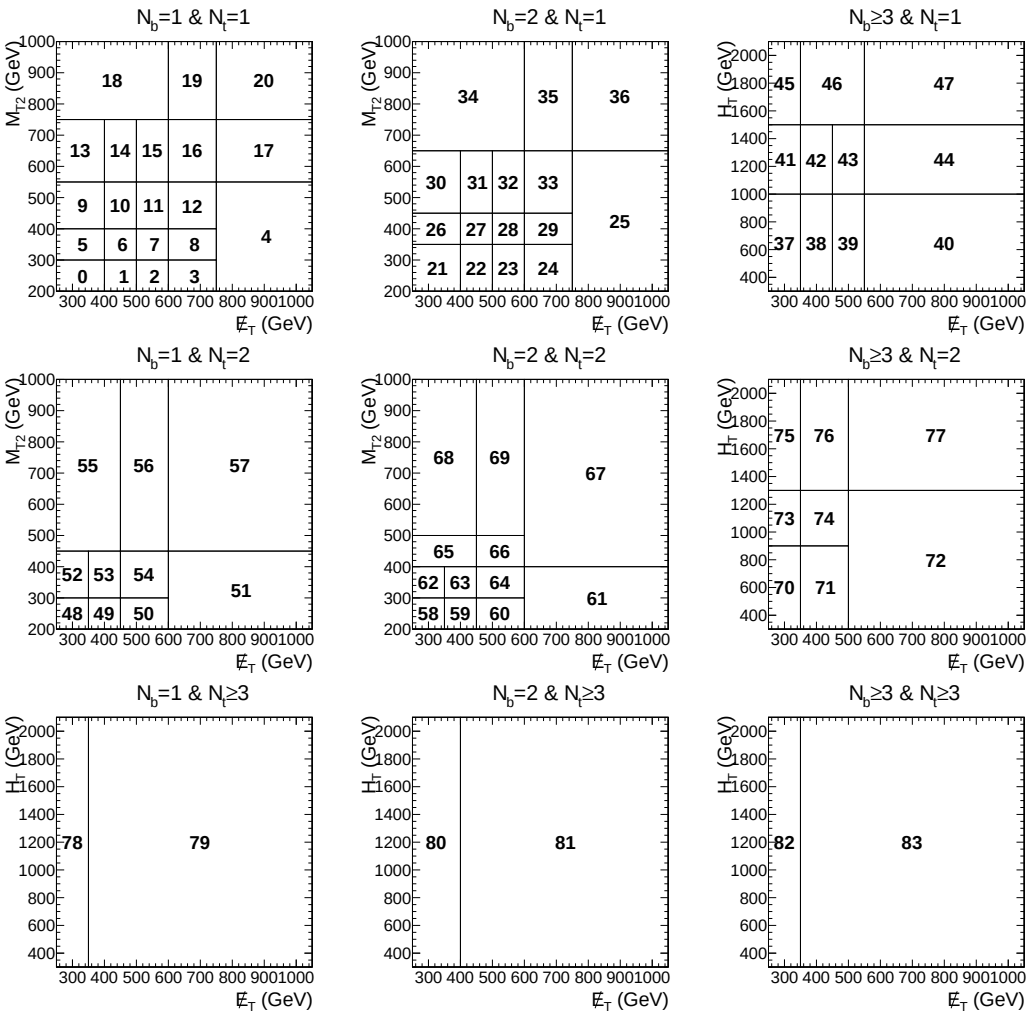

Figure 5.5: All non-overlapping 84 search bins after baseline selections. Regions with $N_{\text{b-jets}} \leq 2$ and $N_{\text{tops}} \leq 2$, we use $N_{\text{b-jets}}$, N_{tops}, $E_{\text{T}}^{\text{miss}}$, and M_{T2} as the binned search variables. Regions with $N_{\text{b-jets}} \geq 3$ and $N_{\text{tops}} \geq 3$, we use $N_{\text{b-jets}}$, N_{tops}, $E_{\text{T}}^{\text{miss}}$, and H_{T}. The reason H_{T} is used for these latter regions, and not M_{T2}, is that in events with many jets, the jets from the decay of a particular heavy object may not always be correctly associated with that object, causing the distribution of M_{T2} to be broad and relatively flat. We find that H_{T} provides better discrimination between signal and background for $N_{\text{b-jets}} \geq 3$ and $N_{\text{tops}} \geq 3$. The boundaries between the regions were determined through sensitivity studies.

efficiency requires robust techniques and multivariate analysis. To create a top quark tagging algorithm that is able to function over the full range of top p_{T}, an algorithm combining both highly boosted and lightly boosted scenario is desired.

5.3.1 Resolved Top Tagging

Most of the existing top tagging algorithms in high energy physics follow a cut based approach. In this approach, we put various kinematic restrictions on variables and select events that pass these restrictions for further study. For example, while identifying the Z boson in an event, one limits the invariant mass of potential Z boson candidates to 50 to 120 GeV and removes all candidates that fall outside of the mass window. Such a method in our case of top quark reconstruction is capable of giving enriched signal regions but comes with an undesirable fake rate. One way to reduce the fake rate is to use many cut variables. But in the cut based approach, the strategy significantly reduces the efficiency of the analysis. An elegant solution in such a scenario is to replace the traditional cut based approach with a Multivariate Analysis (MVA).

Decision Tree: The decision tree is a classic and natural model of learning from the data. The goal is to create a model that predicts the value of a target variable based on several input variables. Suppose one is trying to classify events into a signal and background and has data, or as in our case simulated data samples for each. The first step towards the classification is to split the data into two parts. The first part is called the training sample and second part is called the test sample. The training sample is used to train the model and the test sample will be use to test how accurately the model works on completely new data. Assuming there are several particle identification (PID) variables that help to distinguish signal from background,

we first assign a tree with very basic tasks. Given the particular value of certain variables, we ask for the probability of a particular variable to correspond to signal or to background. Then we pick the boundary value that gives the best separation between signal and background. Then we turn to another variable and repeat the process until we use all variables. A sample decision tree is shown in Fig. 5.6.

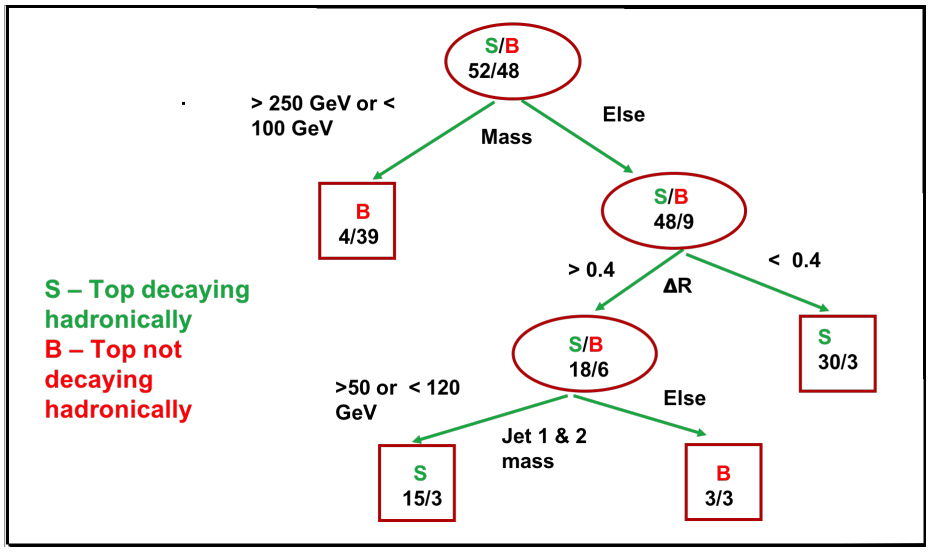

Figure 5.6: Schematic of a decision tree considering only three variables used. S stands for signal, B for background. Terminal nodes (called leaves) are shown in boxes. If signal events are dominant in one leaf, then this leaf is a signal leaf; otherwise it is a background leaf [11].

Random Forest Classifier: Among the myriad of decision tree algorithms available, the most robust against overtraining without losing discrimination power are ensemble algorithms that use a large number of decision trees to create a single discriminator. A number of different algorithms were tested including gradient boost, AdaBoost, random forest, extreme gradient boost, and basic decision trees. During preliminary studies, the gradient boost and the random forest proved to be the strongest options resulting in equivalent performance. The random forest decision

tree algorithm [53] was selected because it allows an ensemble of trees that can separate signal from background effectively without being overtrained on the training data. A random forest decision tree is an ensemble of decision trees that are each independently trained on a different subset of the available training data. Additionally, at each branch point in the individual decision trees, the algorithm only considers a subset of the total number of sample features (input variables) when deciding which cut is best. The output of the random forest is the mode of the individual trees for a classifier or the mean of the individual trees for a regression.

In the top tagging algorithm, the jets in the event are first clustered into top candidates by clustering all combinations of three AK4 jets that have $p_{\mathrm{T}} > 30$ GeV and $|\eta| < 5$. Again the Jets are required to fall into a cone of $\Delta R < 1.5$ and have a combined mass between 110 and 250 GeV in order to encompass the top mass window. The top candidate is allowed to have no more than one b-tagged jet among its three jets. This explicit requirement reduces the fake rate in high b-jet multiplicity events with only a small cost in efficiency. To avoid more than two top candidates sharing the same AK4 jet, the top candidate with the larger MVA discriminator value is allowed to keep the shared AK4 jet.

The Python-based package, Scikit-learn [54], which implements a wide variety of machine learning algorithms, was considered for training of the model. Some preliminary training was performed with this package. But for better integration with our CMSSW workflow, a C++ based package, OpenCV 3.1.0 [55] was used. Also, the OpenCV package comes with a python binding that allows us to match with python-based preliminary work.

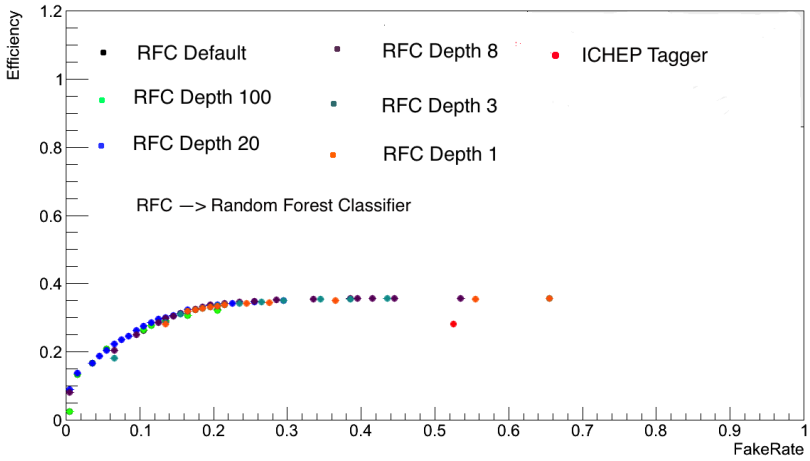

Figure 5.7: Event wise ROC curves for different training depths in random forest classifier. The efficiency was measured in p_{T} bin of generator level top quark in $t\bar{t}$ sample and the fake rate was measured in $Z \to \nu\nu$ samples. The efficiency and fake rate are defined in Eq. 5.4

Training data were prepared with 100000 events from single lepton $t\bar{t}$ samples and 70000 events with $Z \to \nu\nu$ samples. The top candidate criteria mentioned above were slightly loosened for the training samples. The top quark candidates are considered signal if each of the three jets in it is matched to a generator-level quark originating from a single top quark within a cone of $\Delta R < 0.4$. Additionally, the total Lorentz vector of the top candidate must be matched to a generator-level top quark within a cone of $\Delta R < 0.6$. These criteria ensure that the top quark candidate contains an accurate reconstruction of the generator level top quark. The top candidate that fails to satisfy the above criteria are marked as a background. In the case of multiple candidates passing signal or background tests (which often happens), they are all included in the training.

Four quantities were defined to gauge the performance of the tagger. The Receiver Operating Characteristic (ROC) curve is defined in two ways, event-wise and object-

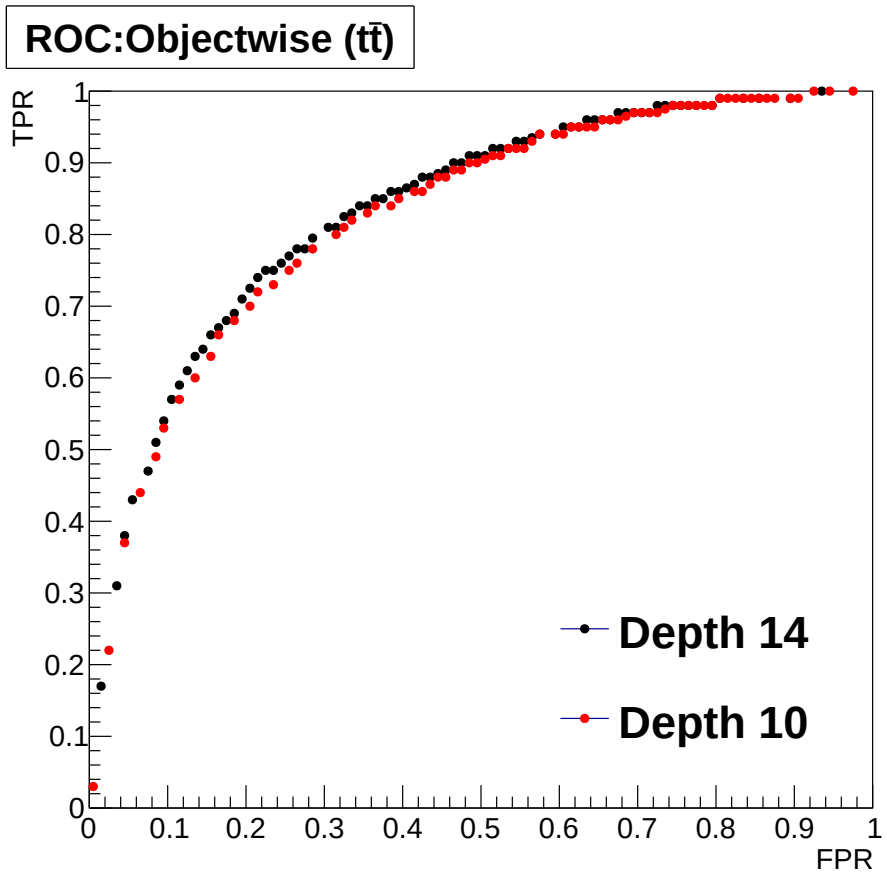

Figure 5.8: Object wise ROC curves for different training depths in random forest classifier. The true positive rate (TPR) and false positive rate (FPR) are defined in Eq. 5.4.

wise. The event-wise ROC is the ratio of the efficiency over the fake rate whereas the object-wise ROC is defined as the ratio of the true positive rate (TPR) over the false positive rate (FPR). These quantities are defined as follows:

$$\text{Efficiency} = \frac{\text{Number of generator-level top quarks matched to a tagged top}}{\text{Number of generator-level top quarks in an event}},$$

$$\text{Fake rate} = \frac{\text{Number of events having at least one tagged top}}{\text{Total number of events}},$$

$$\text{TPR} = \frac{\text{Number of tagged top candidates matched to a generator-level top quark}}{\text{Number of top candidates matched to a generator-level top quark}},$$

$$\text{FPR} = \frac{\text{Number of tagged top candidates not matched to a generator-level top quark}}{\text{Number of top candidates not matched to a generator-level top quark}}. \tag{5.4}$$

Here, "tagged top" indicates the trijet combination (top candidate) with a MVA discriminator value above a given threshold. The fake rate is measured from simulated $Z \to \nu\nu +$ jets events.

The tree depth defines the maximum number of branch nodes in any branch of a particular tree in the random forest. An extensive study was carried out to tune the correct tree depth. The tree depth was smoothly varied to find the balance between the optimized result and computational load management. A depth of 14 was chosen for training the nominal working points to maximize the signal versus background separation. If the depth is chosen too small, the signal distribution for the discriminator will be highly compressed against one end of the spectrum, while if the depth is chosen too large, the risk of overtraining is increased. the ROC curves are shown in Fig. 5.7 and 5.8.

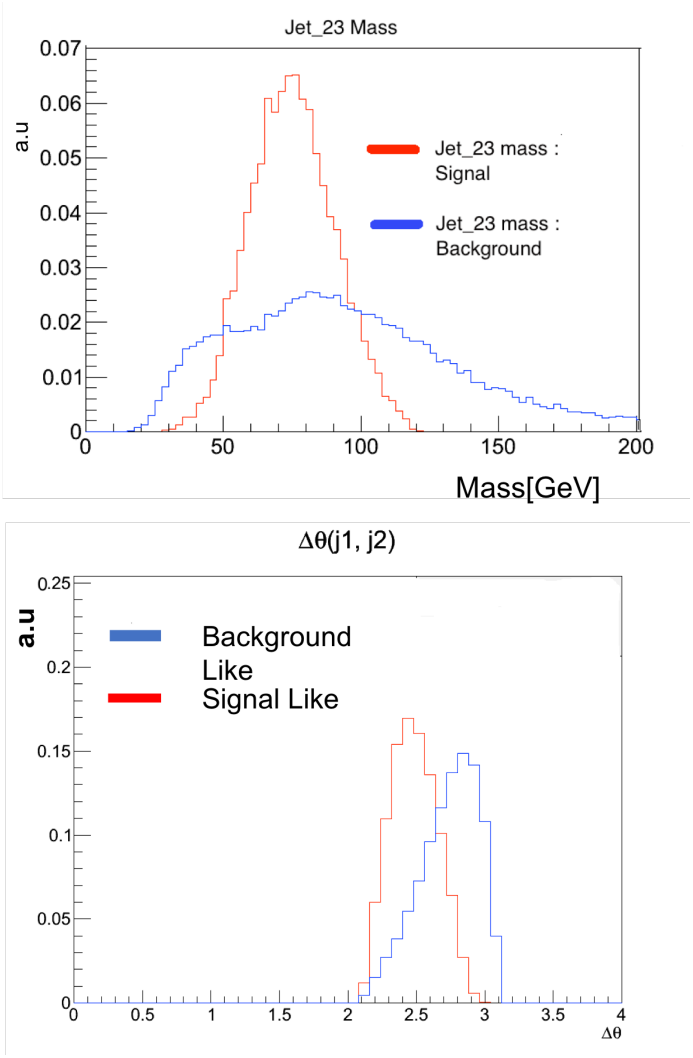

Figure 5.9: Distributions of two input variables in the case of training signal and background. Red (blue) curves indicate signal (background). Top shows the mass of dijet formed of 2nd and 3rd leading p (momentum) jets where p is measured in the rest frame of the trijet. Bottom shows the angular separation between leading and 2nd leading jet in momentum.

A different set of variables were used to check the discriminating power of variables. The most powerful variables were top candidate properties such as mass, p_{T}, and ΔR, constituents jet properties such as p_{T}, mass, η , ϕ and angular variables like ΔR, $\Delta\phi$ $\Delta\eta$ etc. Discrimination performed by a few key variables is shown in Fig. 5.9.

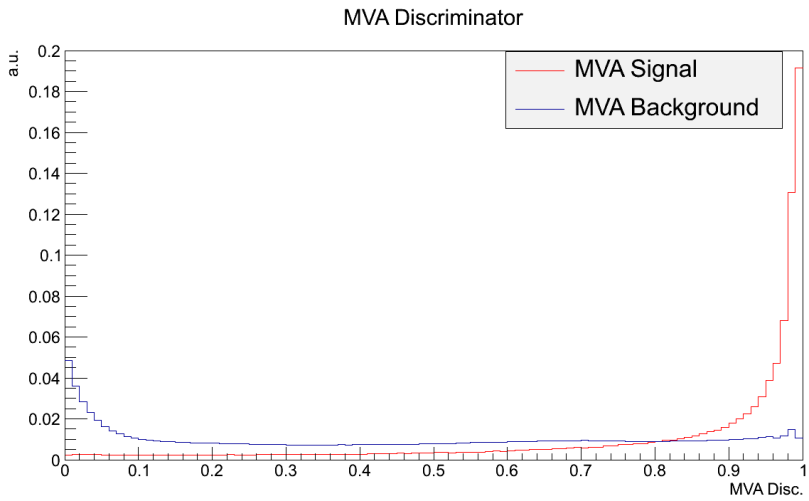

Figure 5.10: The discriminator for signal and background from the final trained random forest separated between signal and background-like candidates. A discriminator cut of 0.85 was used for the final analysis.

The efficiency of the tagger is estimated using the full semi-leptonic $t\bar{t}$ MC sample. The fake rate is measured using the $Z \to \nu\nu$ sample where there are no hadronic decays of the top quark. Any tagged top in the sample where are no real top quarks will be counted as fake. Both the efficiency and fake rate were compared to that of previously adopted cut base tagger [56]. The efficiency of the MVA-based resolved tagging algorithm is somewhat lower than that of the cut-based tagger; however, the fake rate is much reduced. Comparisons between MVA based resolved tagger and cut based tagger for efficiency and the fake rate are shown is Fig. 5.11.

5.3.2 Merged Top Tagging

As the top quark p_{T} increases, decay products get closer together. Thus for high p_{T}, hadronically decaying top quarks, one can no longer distinguish three jets. Instead, we reconstruct the decay products of the top quark as two jets (medium boost) or one jet (high boost). For ak4jets, the full top quark decay would be contained within

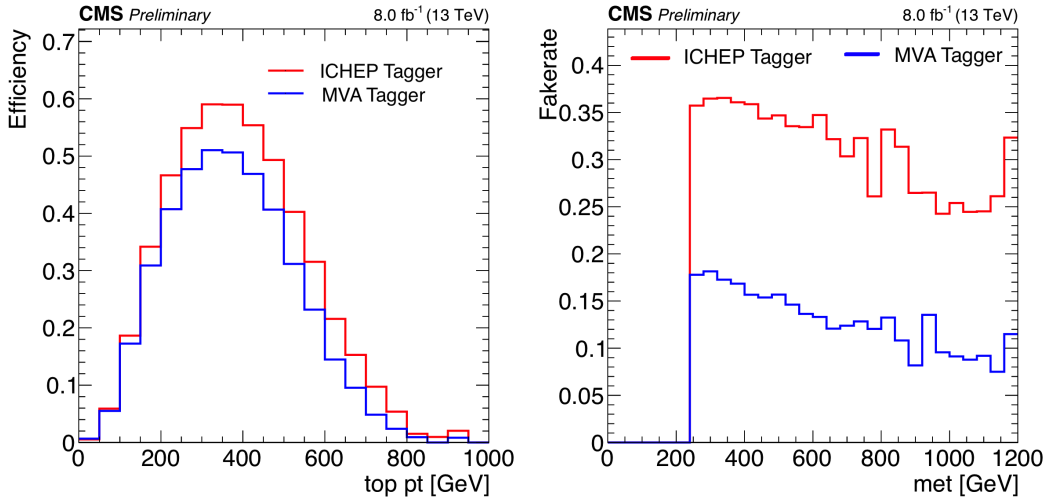

Figure 5.11: Overall efficiency as measured in generator level top quark p_{T} bin of $t\bar{t}$ sample for both a MVA based tagger and an old tagger (left) and fake rate as measured in $E_{\mathrm{T}}^{\mathrm{miss}}$ bin of $Z \to \nu\nu$ sample (right).

the jet at a top quark p_{T} of around 700 GeV, which is quite high, and much larger than the point where the resolved top tagger becomes less effective. Therefore, it has become standard practice to use ak8jets to reconstruct boosted top quarks. Top quarks with a p_{T} above 400 GeV will have decay products contained within the ak8jet. In addition, we also consider the case where only the decay products of the W boson are contained within one ak8jet, which happens for W bosons with $p_{\mathrm{T}} > 200$ GeV.

As per suggestion by the JetMET working group within the CMS, we use three major requirements for boosted top quark tagging. ak8jets with Puppi (pileup suppressed) with $p_{\mathrm{T}} > 400$ GeV to select boosted jets, soft drop mass [57] between 105 GeV and 210 GeV to catch the top quark mass window, and N-subjettiness[1] (τ_{12}) < 0.65 [58] to identify the number of subjets associated with each ak8jet. For the boosted W boson, we require $p_{\mathrm{T}} > 200$ GeV to select a slightly boosted W boson, soft drop mass

[1] N-subjettiness is a jet shape designed to identify boosted hadronic objects such as top quarks. Given N subjet axes within a jet, N-subjettiness sums the angular distances of jet constituents to their nearest subjet axis.

between 65 GeV and 100 GeV to catch the W boson mass window, and subjettiness < 0.60 to make sure there are two jets associated with W boson decay.

Since we are using two jet collections in the same event, we have to make sure that no two jets are sharing the same particle flow candidate. This might lead to over-counting top quarks and a faulty M_{T2} calculation. The basic approach taken here is to remove ak4jets that correspond to an ak8jet (that is tagged as a merged W boson or top quark) from the list of jets used as input to the MVA-based resolved top tagger. The ak4jets removal process can be carried out in two ways: ΔR matching between ak4 and ak8jets, and ΔR matching between the ak4jets and the soft-drop subjets of the ak8jets. In either method, if ΔR is less than certain threshold, then the ak4jet is removed. All tagged W bosons and top quarks that can be matched to a generator-level hadronically decaying W boson or top quark within a cone of $\Delta R = 0.4$ were used. Rigorous cross-validations were performed in different signal models with different mass points.

To check the performance of the subject matching scheme, we count the number of ak4jets that are matched (within a cone of $\Delta R = 0.4$) to the subjects of a given tagged top quark.

5.3.3 Combined Algorithm

Individual taggers have a variety of adjustable parameters that can be tuned to manipulate the performance of algorithms. The most important parameters in merged algorithms were jet p_{T} and the mass window of top quark and W boson. In the resolved tagger, we can adjust the discriminator to tune the efficiency and fake rate. The working point presented in this analysis is the tight working point which keeps

a balance between efficiency and fake rate.

Performance of the combined tagger is very good overall. The efficiency was calculated using the $t\bar{t}$ semileptonic sample and the fake rate by $Z \to \nu\nu$ sample. The overall efficiency as compared with the cut based tagger is shown in Fig. 5.12 and the fake rate in bins of the search variables are shown in Fig. 5.13. There is overall a similar efficiency but the fake rate is reduced drastically.

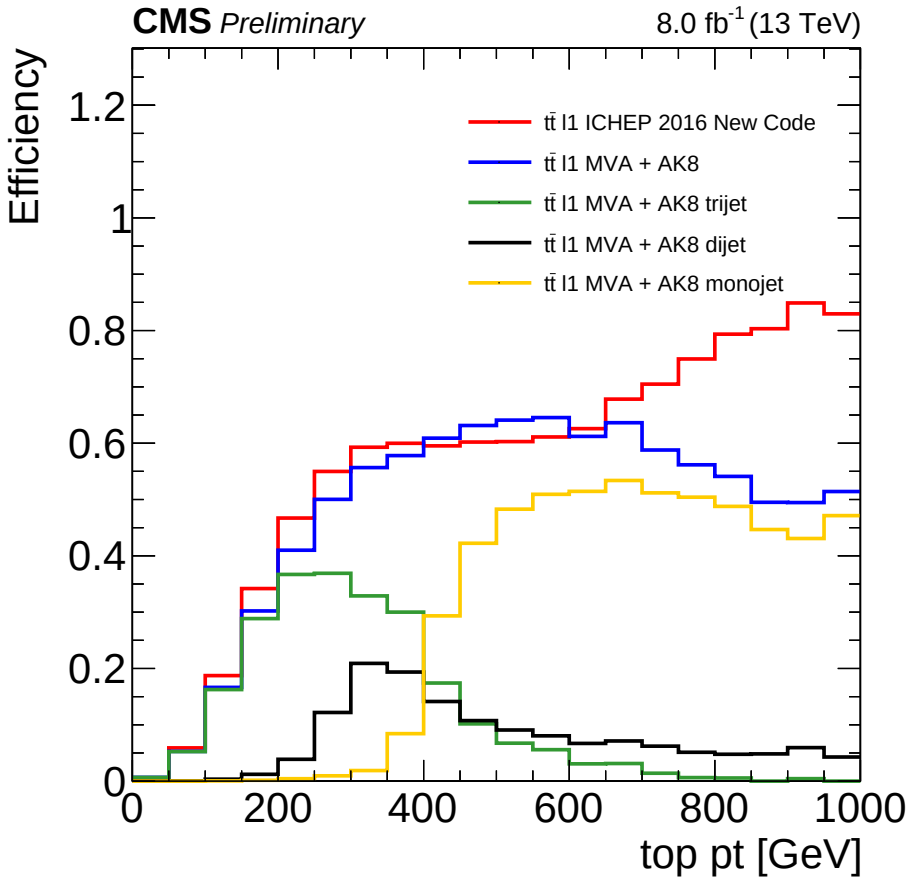

Figure 5.12: Overall efficiency of the combined tagger with a cut based tagger. The red lines are from the result immediately before the combined algorithm was developed. There is no significant loss of efficiency in low top p_{T} region. There is slight drop in efficiency in high p_{T} region but the signal is expected to be very small.

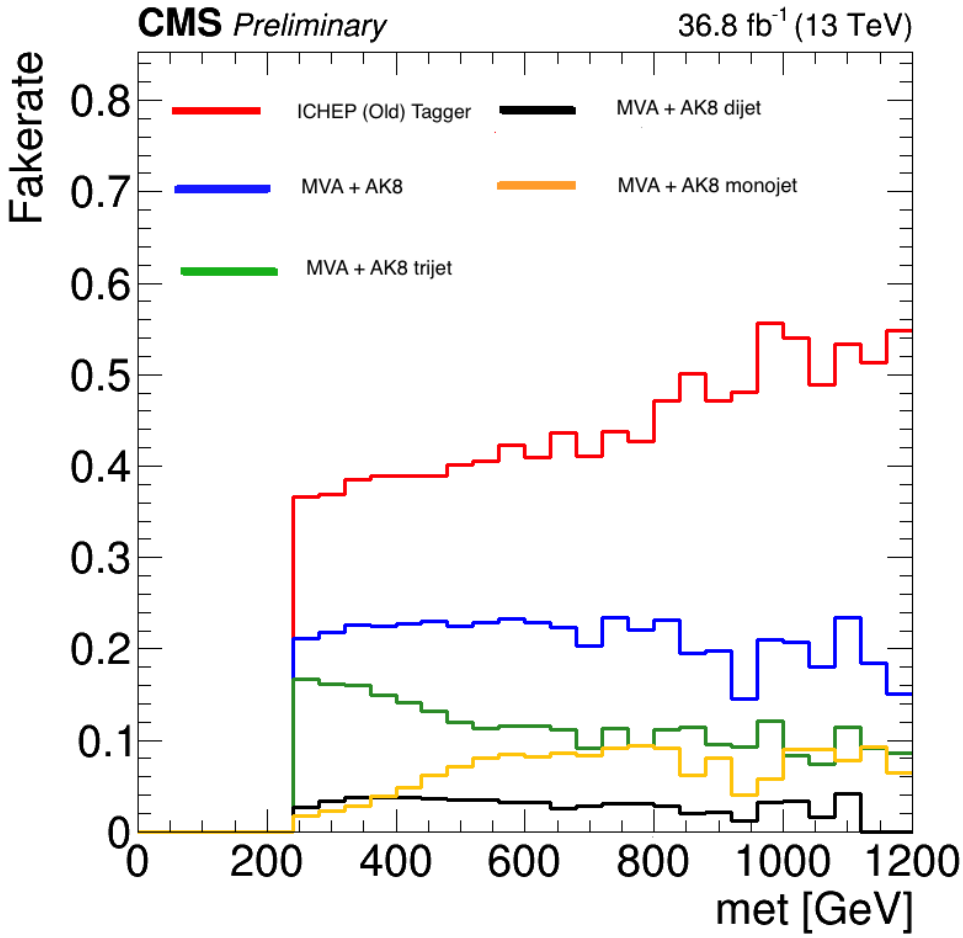

Figure 5.13: Fake rate as measured for search variables $E_{\mathrm{T}}^{\mathrm{miss}}$.

With a large phase space of signals to cover, the SUSY signals used for the analysis are simulated by the CMS fast simulation (fastsim) package. The CMS fast simulation provides an alternative to the GEANT-based approach (aka fullsim) and requires much less CPU time. Previous studies have been carried out with the fullsim sample. For the SUSY analysis, the performance of top tagging needs to be validated in the fastsim sample as well. As seen in Fig. 5.14, the top tagging efficiency is generally shown to be in good agreement between the fullsim and fastsim samples. Efficiency in data was calculated from single muon collider data triggered with a single muon with p_{T} greater than 45 GeV and $|\eta| < 2.1$, corresponding to an integrated luminosity

of 24.8 fb^{-1} and calculated using relation,

$$\epsilon = \frac{\text{best top candidate}}{\text{best top candidate + best jet combination}}. \tag{5.5}$$

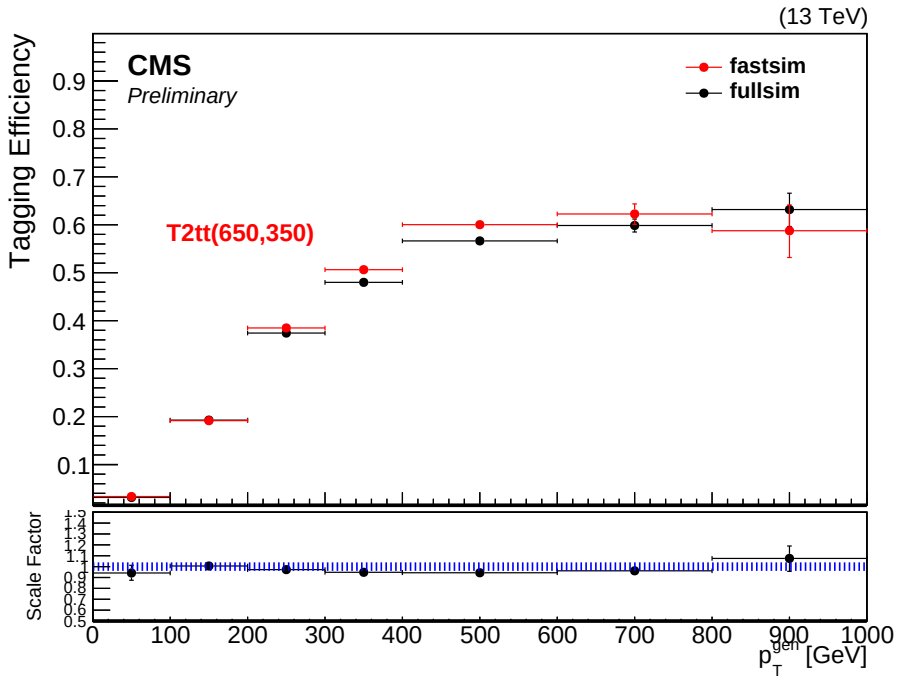

Figure 5.14: Fastsim vs Fullsim comparision and scalar factor of one of the signal point T2tt(stop mass 650 GeV , mLSP 350 GeV). The error bar (mostly smaller than the data symbol) depicts the statistical uncertainty. The ratio of these efficiencies is taken to be the scale factor for the fastsim signal samples.

5.4 Monte Carlo Samples for Background and Signal Studies

The analysis uses a set of Monte Carlo samples for background estimation method and interpretation of the results with respect to the number of simplified models used in the analysis. All background samples are generated with the Geant4-based CMS simulation application while all signal samples used to set limits are generated using the Fast Simulation application. Monte Carlo samples of SM processes reconstructed with CMSSW release 8.0 (Spring16) are used throughout this analysis.

CHAPTER 6

Background Estimation

6.1 Background from Top and W decays

The background from $t\bar{t}$, W + jets and single-top events that are not removed by the lepton-veto and isolated track veto cuts discussed in Chapter 5 are the largest background in the analysis. It can contain either a hadronically decaying tau or light leptons (electrons or muons) that are not isolated, not identified/reconstructed, or are out of the acceptance region. Both types of backgrounds are estimated using the translation factor (TF) method. Being a relatively new method, its validity is tested against the well established "classic lost lepton method" [59].

6.1.1 Translation Factor Method

When W bosons decay into leptons (e, μ or τ) and neutrinos, energy carried by a neutrino results in $E_{\mathrm{T}}^{\mathrm{miss}}$. The event can pass the selection criteria as described in section 6.1. Events with taus, reconstructed as jets in the final state, can also pass the selection criteria. This background is estimated using a control region of single lepton events selected from data using search triggers. Both muon and electron control samples (CS) are used to reduce the statistical uncertainty. The muon control sample is prepared by requiring exactly one muon with the momentum $p_T^{\mu} > 10$ GeV and $|\eta| < 2.4$ in μ + jets events and for the electron control sample we require $p_T^e > 10$ GeV and $|\eta| < 2.5$. A cut on the transverse mass of the W, $m_T = \sqrt{2p_T^l E_T^{miss}(1-\cos\Delta\phi)} < 100$ GeV, is required in order to select events containing a $W \to l\nu$ decay and to suppress possible new physics-signal contamination. Here, l indicates either an electron or a muon and $\Delta\phi$ is the azimuthal angle between

the $\vec{p_T}^{\,l}$ and the $E_{\mathrm{T}}^{\mathrm{miss}}$ directions.

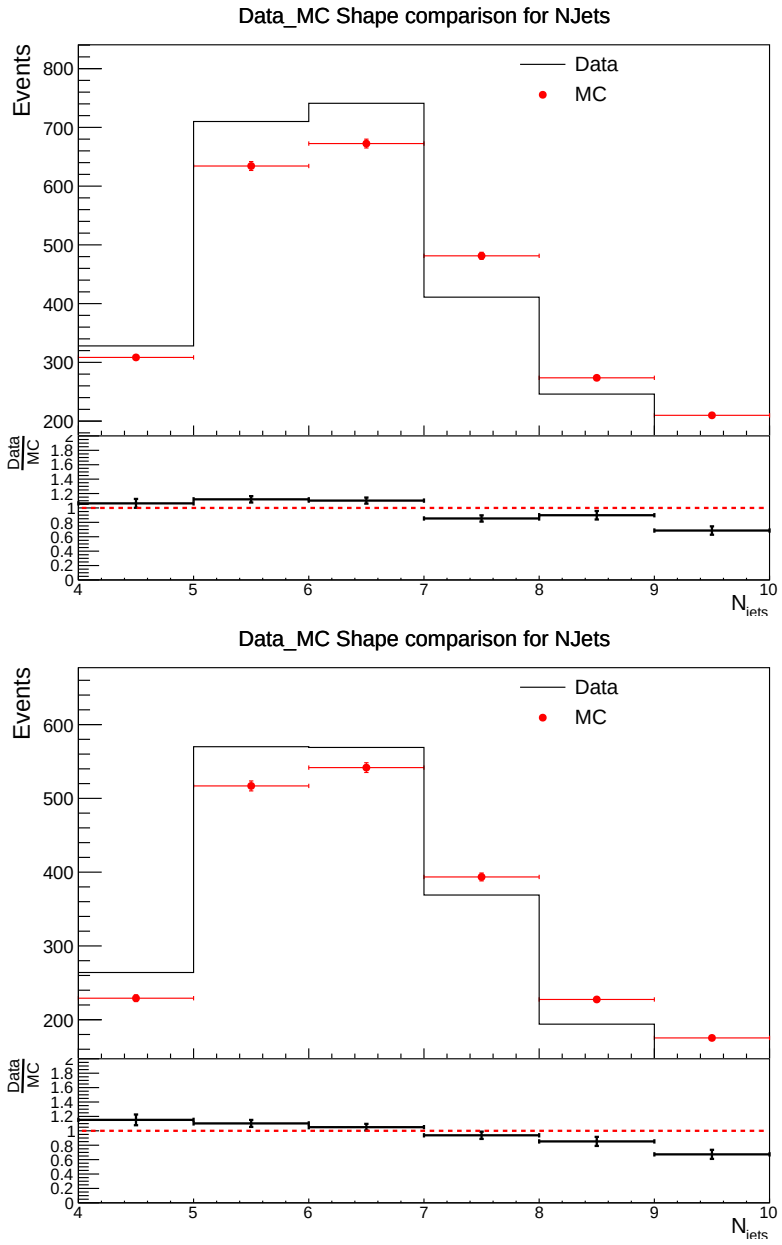

Figure 6.1: A shape comparison for the N_{jets} for the muon (top) and electron (bottom) control samples.

In order to predict the number of events in signal regions, we measure the translation factor (TF) from simulation. The translation factor is defined as $TF^i = N^i_{SR}/N^i_{CS}$,

where N^i_{SR} is the number of either hadronic tau or lost lepton events in the i^{th} signal region and N^i_{CS} is the number of CS events in the corresponding signal region. Apart from the difference of the W boson decay, the CS and signal region have similar hadronic activities. The lepton (muon and electron) control sample is selected from either simulation or collider data applying the same criteria as discussed in Chapter 5 except for the fact that we require exactly one muon for the muon CS and one electron for the electron CS.

The differences between MC and data were studied by shape comparisons with different kinematic variables for both electron and muon control samples. For a shape comparison, the overall MC has been scaled down by 73% for the muon CS and 71% for the electron CS. We find that there is a data versus MC shape difference for N_{tops}, N_{jets}, M_{T2}, and $E_{\text{T}}^{\text{miss}}$. The agreement between data and MC for $N_{\text{b-jets}}$ is already quite good. Shape comparisons between MC and data for kinematic variables are shown in Figs. 6.1 and 6.2. To account for data and MC differences, the MC sample is corrected by three scale factors; Initial State Radiation (ISR) correction, b-tagged jet scale factors, and Lepton Efficiency. The efficiency in lepton detection is very important because they are treated differently in CS where leptons are selected and the signal region where leptons are vetoed. Therefore we do not have a well-identified lepton to begin with and we thus use the following relation to propagate the correction factors:

$$N^i_{prod} = N^i_{lost} + N^i_{sel} \tag{6.1}$$

where the N^i_{prod} is the total produced number of events in the i^{th} signal region with a W boson decaying to a muon, electron or hadronically decaying tau (τ_h), N^i_{lost} is the number of events that end up in our signal region after all the search cuts are applied including the lepton and isolated track veto. N^i_{sel} is the number of events se-

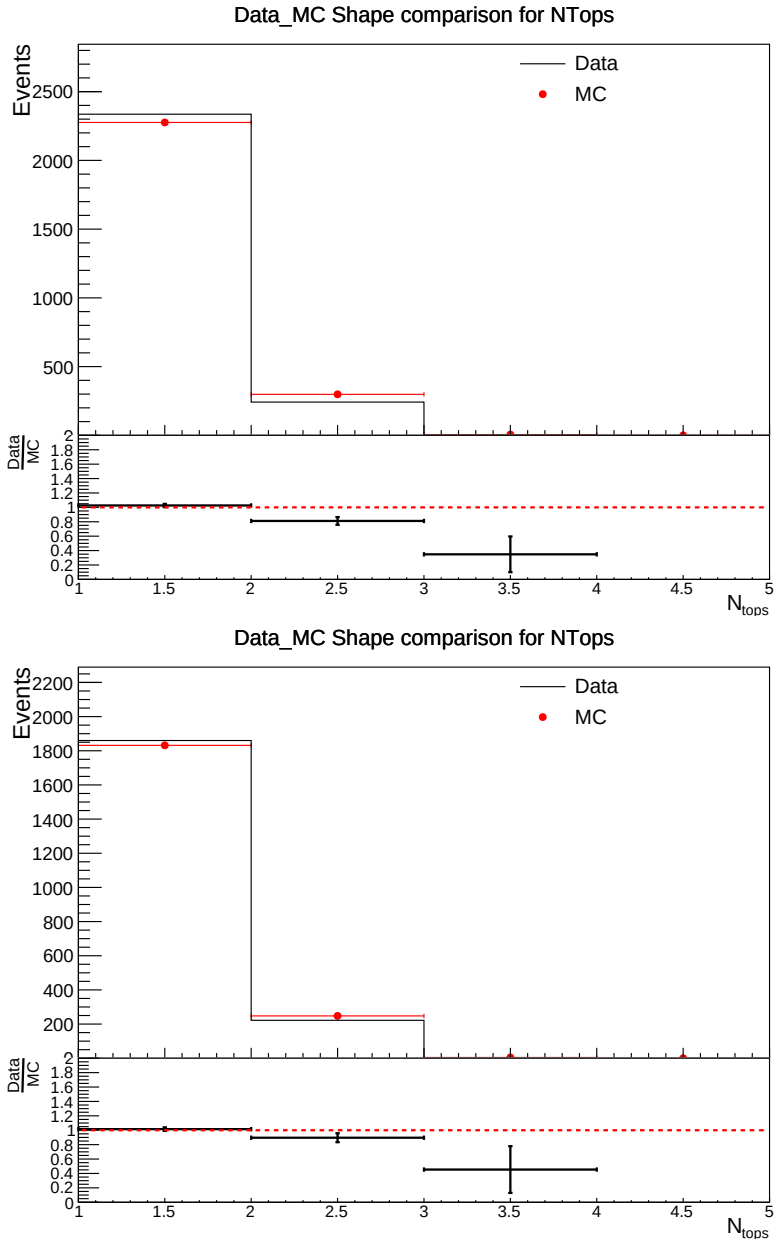

Figure 6.2: A shape comparison for the N_{tops} for the muon (top) and electron (bottom) control samples.

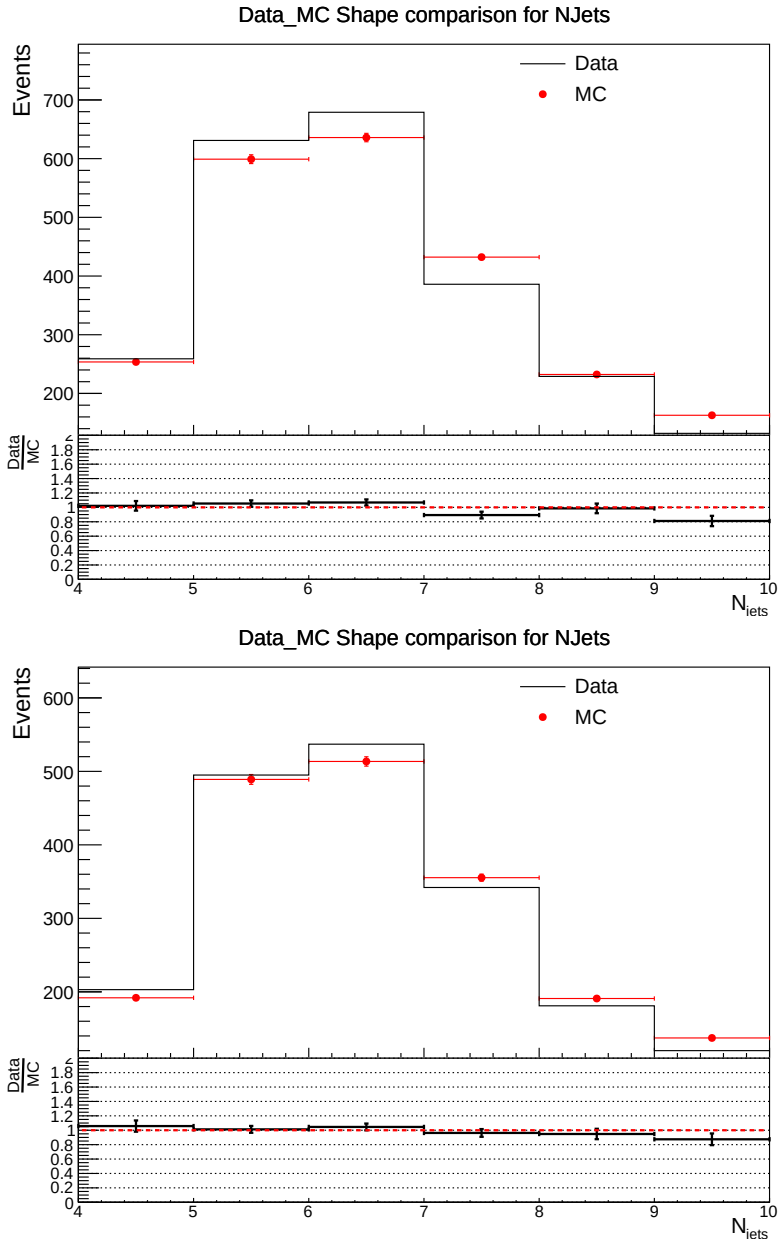

Figure 6.3: Shape comparison for the N_{tops} for the muon CS (top) and electron CS (bottom) after applying various scale factors.

lected with an identified muon, electron or isolated tracks for vetoing. N^i_{prod} remains unchanged regardless of corrections to the lepton data/MC scale factors. Therefore the change of the simulated number of events due to lepton SF on the N^i_{sel} can be easily propagated to the quantity we are interested in, that is, the N^i_{lost}.

After applying scale factors, the event variable shape comparisons are shown in Figs. 6.3 and 6.4. For the shape comparisons, the muon MC CS is scaled by 84% and electron MC CS is scaled by 83%. We can clearly see the improvement of the N_{jets} and N_{tops} distributions.

A single translation factor in each search region is evaluated from simulated $t\bar{t}$, W + jets, and single-top events. The ratio of τ_h or lost lepton events after a full search selection cuts to the lepton CS events selected with the criteria discussed above determines the translation factor. Two sets of TF are measured for muon and electron CS separately. The uncertainty on these scale factors is included as a systematic uncertainty. The data-corrected translation factors for the lepton control sample are shown in Fig. 6.5. As expected, within the uncertainties, the TF from electron and muon CS follow a similar trend across all the search bins.

6.1.2 Systematic uncertainties

The major source of systematic uncertainty of this method is the statistical error on the translation factor. A translation factor includes all the cuts, correction factors, and selection efficiency. The uncertainty on lepton efficiency affects both lepton selection and lepton veto. The jet energy scale uncertainty and b-tag SF uncertainty affect the jet and b-jet selection, respectively. As the prediction is obtained by multiplying the translation factor with the data CS, the change in the prediction can

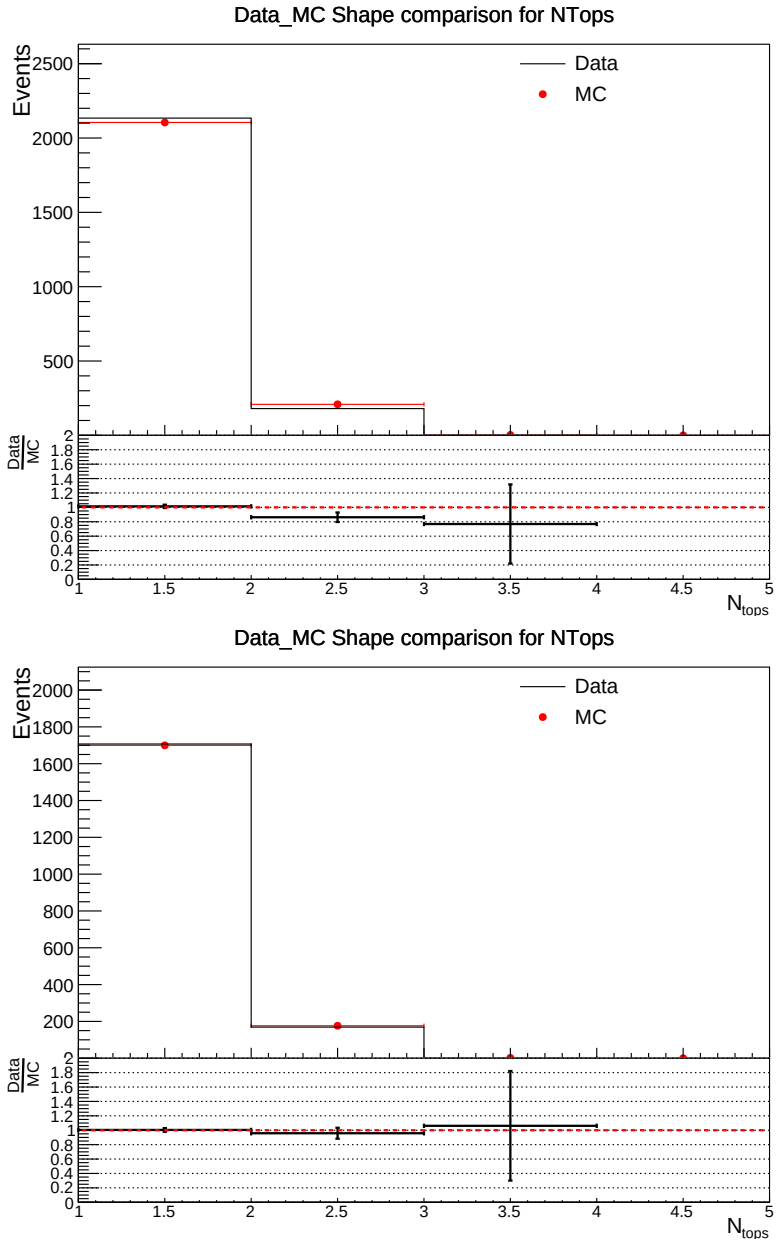

Figure 6.4: Shape comparison for the N_{tops} for the muon CS (top) and electron CS (bottom) after applying various scale factors.

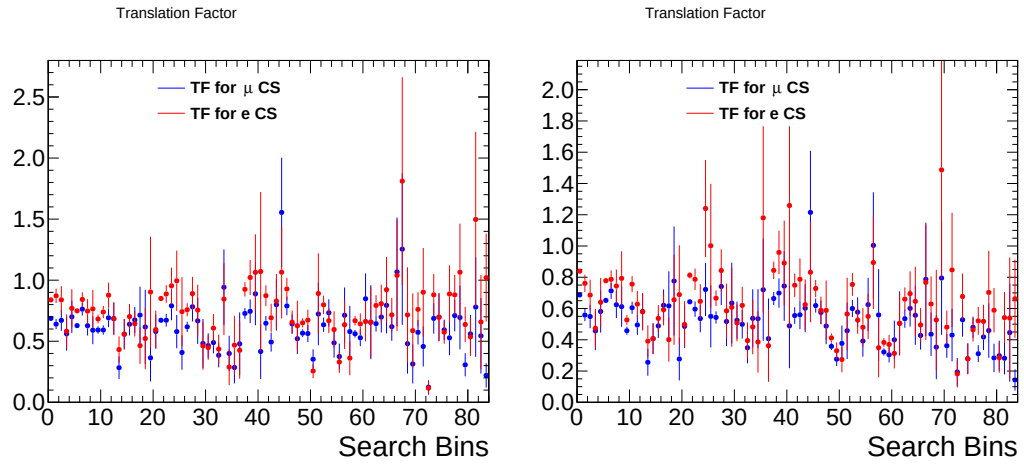

Figure 6.5: Translation factors for the τ_h (left) and the lost lepton (right) background prediction with their uncertainties from limited MC statistics for both muon and electron CS.

be obtained by estimating the change in the translation factor. Each factor folded into the translation factor is varied by its uncertainties to determine the change in the ratio. All of the dominant sources of uncertainties and their contribution to the overall uncertainties are listed in the Table 6.1 for hadronic tau background and in the Table 6.2 for lost lepton background.

Table 6.1: Contributions from different sources of systematic uncertainty to the τ_h background prediction.

Process	Source	Effect on τ_h Prediction in %
τ Translation factor statistical error	Statistics of MC SR and CS events	1 to 50
Lepton efficiency SF (including isolated tracks)	Data-MC correction from tag and probe method and studies	5 to 52
B-tag SF	Uncertainty on b-tag SF	0 to 1
$E_{\mathrm{T}}^{\mathrm{miss}}$ mag and ϕ	Uncertainty related to $E_{\mathrm{T}}^{\mathrm{miss}}$ mag and ϕ	0 to 54
JEC	Jet energy correction uncertainty	0 to 52
ISR	Variation of ISR weight	0 to 11
PDF	PDF uncertainty	0 to 31

6.1.3 Prediction

After applying the measured TF from simulation to the data CS events we can obtain the hadronic tau background predictions. Since we have data CS from both electron and muon channels, we average the predictions from both CS to estimate the final overall systematic uncertainty. Fig. 6.6 shows the predictions for all search regions. The error bars in the figures include both statistic and total systematic uncertainties. The statistical uncertainties are the propagation of Poisson statistics of the observed data CS events from both electron and muon channels given by the Garwood interval [60]. While a Poisson distribution of mean μ_s has a variance equal to μ_s, an interval $(\mu_s + \sqrt{\mu_s}, \mu_s - \sqrt{\mu_s})$ may result in under-coverage, especially if μ_s is not large. This may either arise in low-statistics histograms, or in high-statistics ones drawn on a semi-logarithmic scale. These "correct coverage" vertical bars, first derived by Garwood in 1936 [60], are obtained from the Neyman construction using the central interval convention.

Table 6.2: Contributions from different sources of systematic uncertainty to the lost lepton background prediction.

Process	Source	Effect on lost lepton Prediction in %
Lost lepton translation factor statistical error	Statistics of MC SR and CS events	2 to 51
Lepton efficiency SF (including isolated tracks)	Data-MC correction from tag and probe method and studies	7 to 46
B-tag SF	Uncertainty on b-tag SF	0 to 2
$E_{\mathrm{T}}^{\mathrm{miss}}$ mag and ϕ	Uncertainty related to $E_{\mathrm{T}}^{\mathrm{miss}}$ mag and ϕ	0 to 40
JEC	Jet energy correction uncertainty	0 to 56
ISR	Variation of ISR weight	0 to 13
PDF	PDF uncertainty	0 to 32

The prediction from an average TF method was compared with the classic and well established lost lepton method [56]. It is observed that both methods agree very

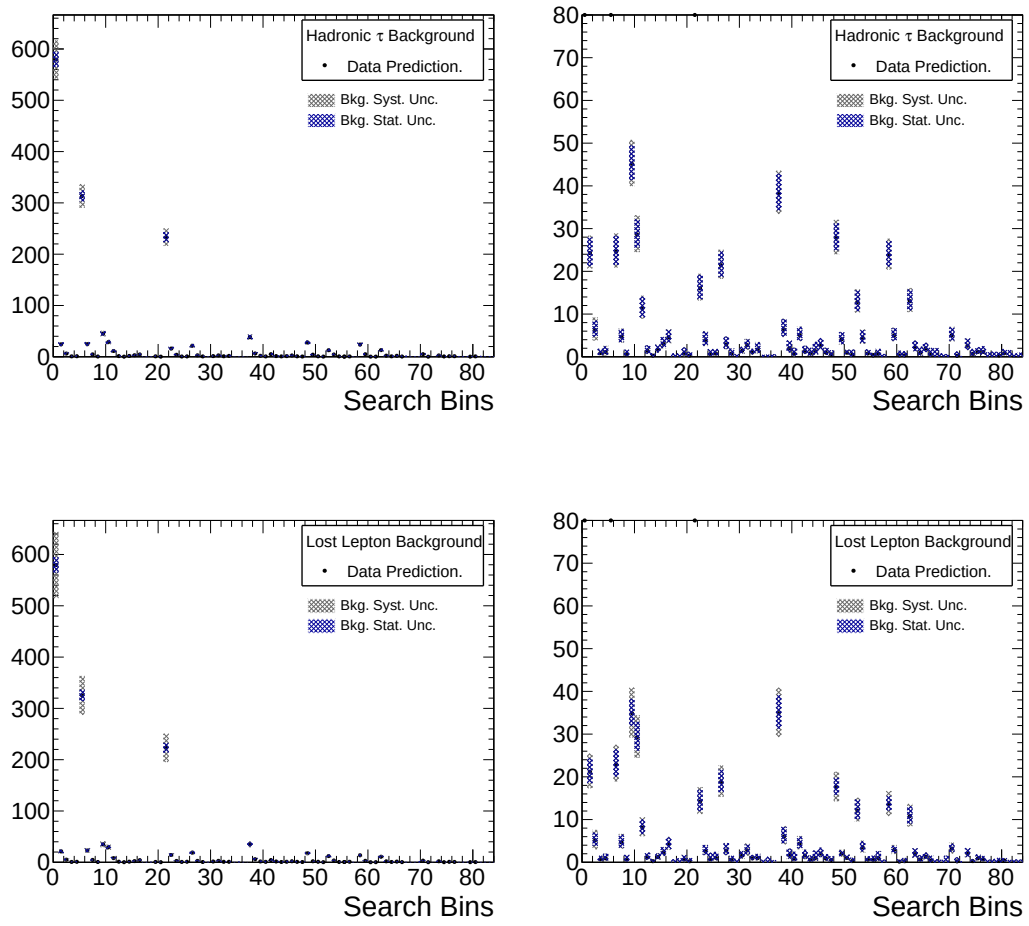

Figure 6.6: Predicted τ_h background (top) and lost lepton background (bottom) yield for a 35.9 fb^{-1} data for all the search regions. Right plots are a zoomed version of left plot. Both statistical and total systematic uncertainties are shown.

well within statistical uncertainties. Comparison of prediction from both methods is shown in Fig. 6.7.

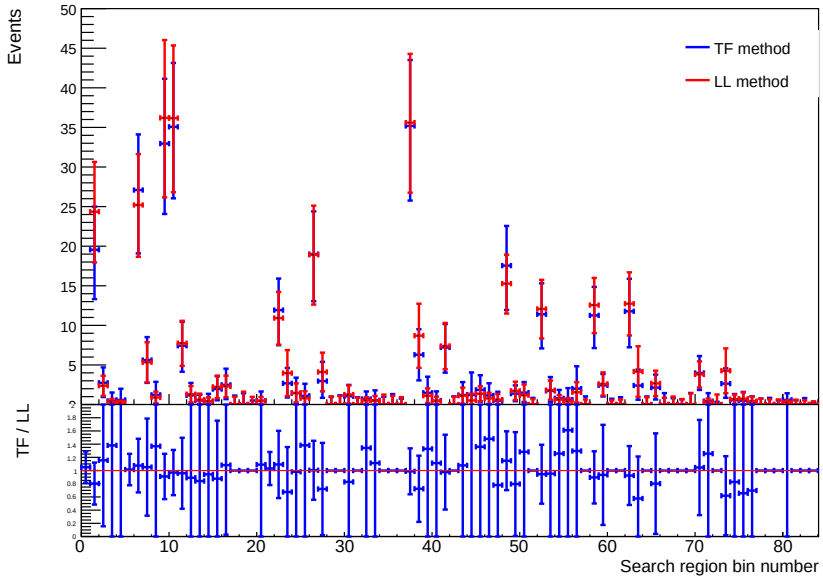

Figure 6.7: Lost lepton background predictions on muon control sample, in red. The blue points are the results obtained with the average TF method. The uncertainties include both the statistical and systematic uncertainties.

6.2 Backgrounds From Neutrinos in Z Decays

This background arises from Z + jets events where the Z boson decays into a pair of neutrinos. Neutrinos contribute to $E_{\mathrm{T}}^{\mathrm{miss}}$ and the presence of jets may allow the event to enter the search region. Due to a small branching ratio for $Z \to \nu\nu$ we do not have a large real data samples to study this irreducible background. Instead using the direct data-driven method, we use a data validated Monte-Carlo method. In this multistage process, the final estimate is taken from the $Z \to \nu\nu$ MC, which is corrected for data/MC differences observed in a control region with loosened cuts.

The yield of the $Z \to \nu\nu$ background prediction for each search bin B can be written as

$$\hat{N_B} = R_{norm} \cdot \sum_{events \epsilon B} S_{DY}(N_{jet}) W_{MC}. \tag{6.2}$$

where $\hat{N_{\mathrm{B}}}$ the predicted number of $Z \to \nu\nu$ background events in each search bin B, and W_{MC} a standard MC event weight that includes the estimated $Z \to \nu\nu$ cross-section, the data luminosity, the b tag scale factors, and the measured trigger efficiency. Each MC event is corrected using two additional scale factors. The first, R_{norm}, is an overall normalization factor for the $Z \to \nu\nu$ simulation that is derived in a tight control region in data. This tight control region has the same selection as the search region, apart from the requirement that there be two muons (treated as if they were neutrinos) and that events with any b-tagged jet multiplicity are allowed, so it is a very good proxy for the signal region. The second scale factor, S_{DY}, depends on the N_{jets} in the event and is derived in a loose control region in which the signal region requirements on $E_{\mathrm{T}}^{\mathrm{miss}}$, M_{T2}, and N_{tops} in the event are relaxed.

The corrected MC is further validated in three steps.

- To make sure that the Drell-Yann ($DY \to \mu\mu$) is a good proxy for $Z \to \nu\nu$, we need to match both samples. Some corrections are needed and we introduce a single scale factor. We eventually apply this scale factor to $Z \to \nu\nu$ MC.
- A second layer of validation is to use the loose control region, for which a reasonable number of events are available in data, to check the shape agreement between data and the simulated distributions. Any disagreements will be incorporated as a systematic uncertainty in the prediction.

- We also need to check the data/MC agreement in the loose region, where the shape systematics are assessed, versus the data/MC agreement in the tight region, which is the proxy for the region we want to predict.

6.2.1 Samples and Control Regions

The data set used in the $Z \to \nu\nu$ background estimate corresponds to data taken with the dimuon trigger. These data samples contain exactly two oppositely charged selected leptons, either two muons for the $DY \to \mu\mu$ validation, or an electron and a muon for the validation of the $t\bar{t}$ MC. To guarantee that leptons originate in Z decay, we require the dilepton invariant mass to be within the mass window of $81 < m_{ll} < 101$ GeV. The loose and tight selections were made relative to the baseline cuts to match the control and signal region respectively. The main goal for the loose control region is to provide a data sample that is close to the signal region in terms of kinematic requirements, e.g. the number of jets, but is loose enough to have sufficient events to do a shape comparison for the main analysis variables. The tight region is very similar to the expected signal in the search region in terms of kinematic properties, but it suffers from a lack of the statistics. Therefore, we cannot bin it in all the search bins and only use it to derive an overall normalization for the simulation.

6.2.2 Scale Factor Calculation

- $t\bar{t}$ **Reweighing:** One of the ways the search region differs from the loose control region is that the later is allowed to have zero b-tagged jet bin. When $DY \to \mu\mu$ is used to predict the $Z \to \nu\nu$ background and one b-tagged jet is in an event, a significant number of dimuon events can come from $t\bar{t}$ processes. Therefore, to be able to properly validate the DY MC sample against data in the dimuon

control region, we need a dependable prediction for the $t\bar{t}$ component in that region. Given that the $e\mu$ control region has the highest purity of $t\bar{t}$ events, we use this control region to validate $t\bar{t}$ MC. As per standard CMS SUSY group practices, we use a scale factor included to account for the initial state radiation (ISR reweighing) to make good matching. In Fig. 6.8 perfect agreement is observed between data and MC after applying ISR weight to $t\bar{t}$ MC.

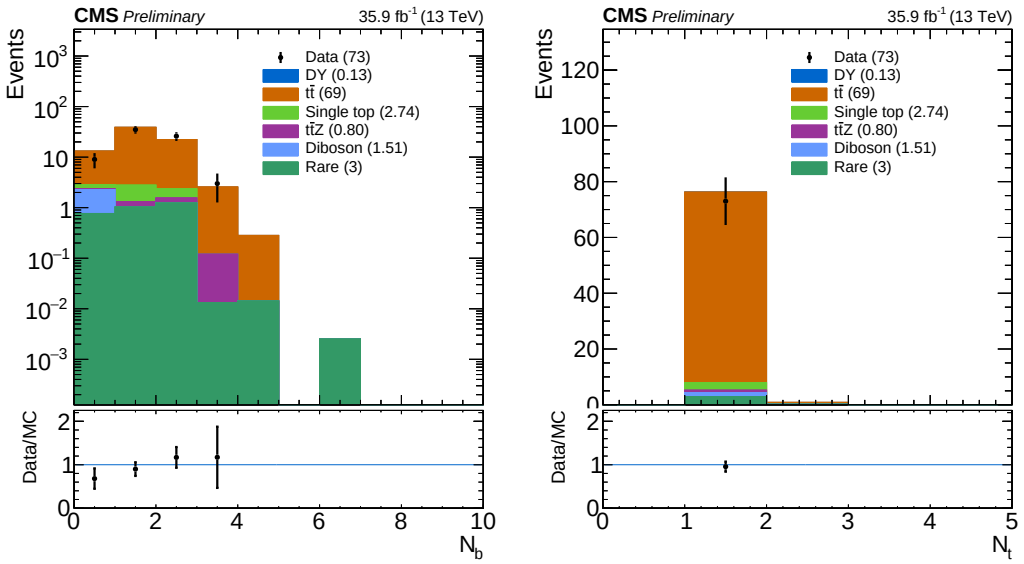

Figure 6.8: Comparison between the $t\bar{t}$ and MC samples for the b-tagged jet multiplicity distribution (left) and the distribution of the number of reconstructed tops in the event (right), in the loose $e\mu$ control region after applying ISR to $t\bar{t}$.

- **Data/MC correction factors from the loose $\mu\mu$ control region ($S_{DY}(N_{jet})$):** To validate DY samples with respect to data in the loose $\mu\mu$ control region which has high purity for the $DY \rightarrow \mu\mu$, it is important to correct for the $t\bar{t}$ contribution. Although there is reasonable agreement between data and MC after correction, lower jet multiplicity bins show larger shape disagreement. This disagreement can be seen in Fig. 6.9.

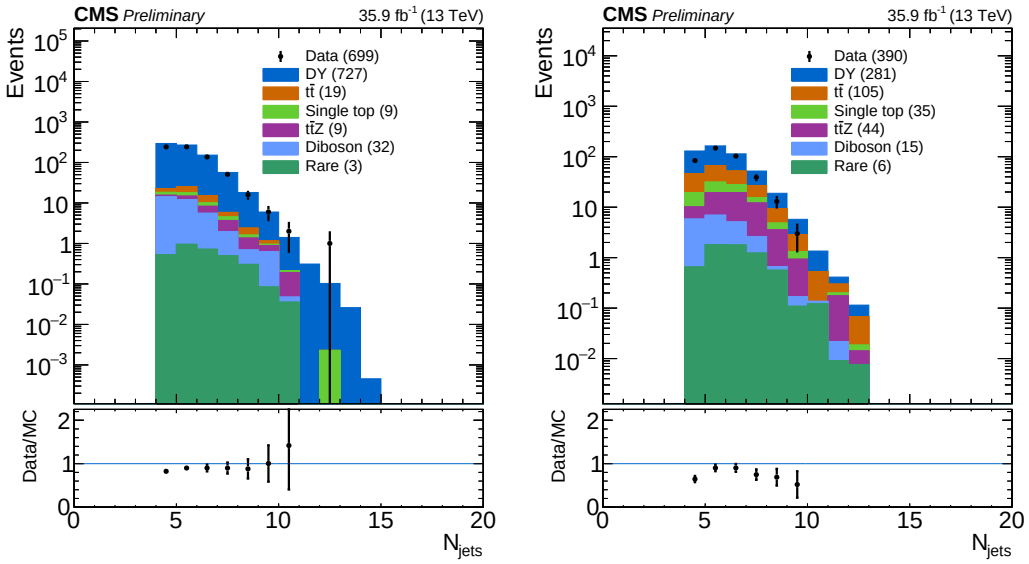

Figure 6.9: Comparison between DY data and MC for the jet multiplicity distribution in the loose $\mu\mu$ control region for events with 0 b-tagged jets (left) and 1b-tagged jets (right) after applying ISR to $t\bar{t}$.

The Data/MC ratio to correct for the difference seen above is derived from the loose $\mu\mu$ region for the separate b-tagged jet bin. All other backgrounds mimicking the $Z \to \nu\nu$ process must be subtracted (except for $t\bar{t}$ which is corrected). The DY MC sample is reweighed with $S_{DY}(N_{\text{jet}})$, which is given by the equation

$$S^i_{DY} = \frac{Data^i - S^i_{t\bar{t}} MC^i_{t\bar{t}} - MC^i_{other}}{MC^i_{DY}}, \tag{6.3}$$

where i denotes a given N_{jet} bin. Discrepancies seen in N_{jets} distribution in Fig. 6.9 are gone after applying $S_{\text{DY}}(N_{\text{jet}})$ as seen in Fig. 6.10.

- R_{norm} **from tight control region:** So far we have derived scale factors from the loose control region. But as mentioned earlier, a good proxy for the search region is the tight control region. First, we apply the N_{jet}-dependent scale factors, $S_{\text{DY}}(N_{\text{jet}})$, $S_{t\bar{t}}(N_{\text{jet}})$, to the relevant MC samples. Then, the ratio of the

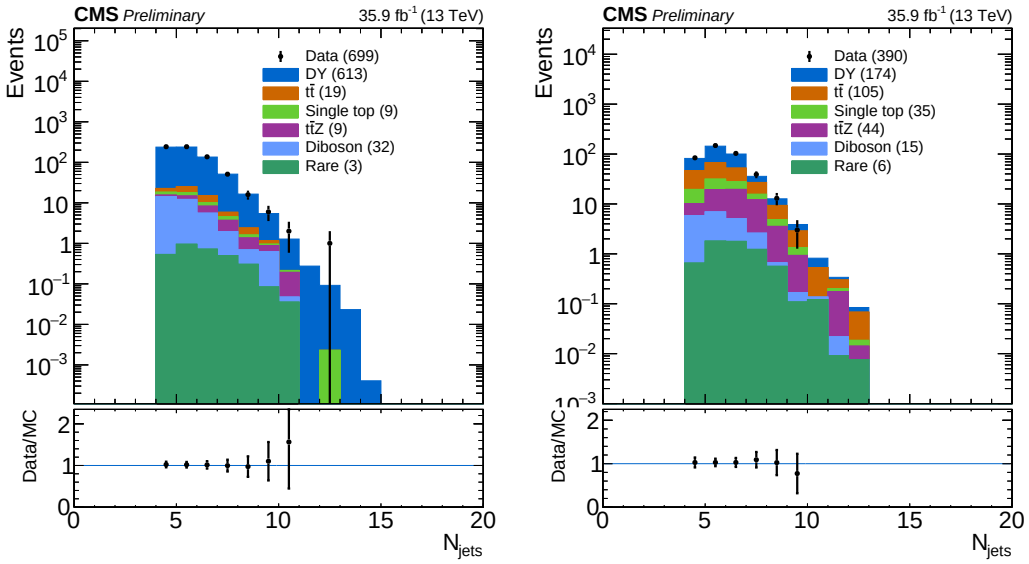

Figure 6.10: Comparison between DY data and MC samples for the jet multiplicity distribution in the loose control region for events with 0 b-tagged jets (left) and $\geq$1 b-tagged jets (right) after applying both the $t\bar{t}$ and DY scale factors.

total event yield in a data to that in the simulation for the tight control region, denoted by R_{norm}, is extracted. We find that

$$R_{\text{norm}} = 1.070 \pm 0.085, \tag{6.4}$$

where the uncertainty includes only the statistical uncertainties on data and simulation. Comparisons between data and MC after applying all scale factors are shown in Fig. 6.11.

6.2.3 Systematic Uncertainty and Prediction

The systematic uncertainties for the $Z \to \mu\mu$ background prediction fall into two categories: uncertainties associated with the use of MC simulations and uncertainties specifically associated with the background prediction method. The first set includes parton distribution function and renormalization/factorization scale factors, jet en-

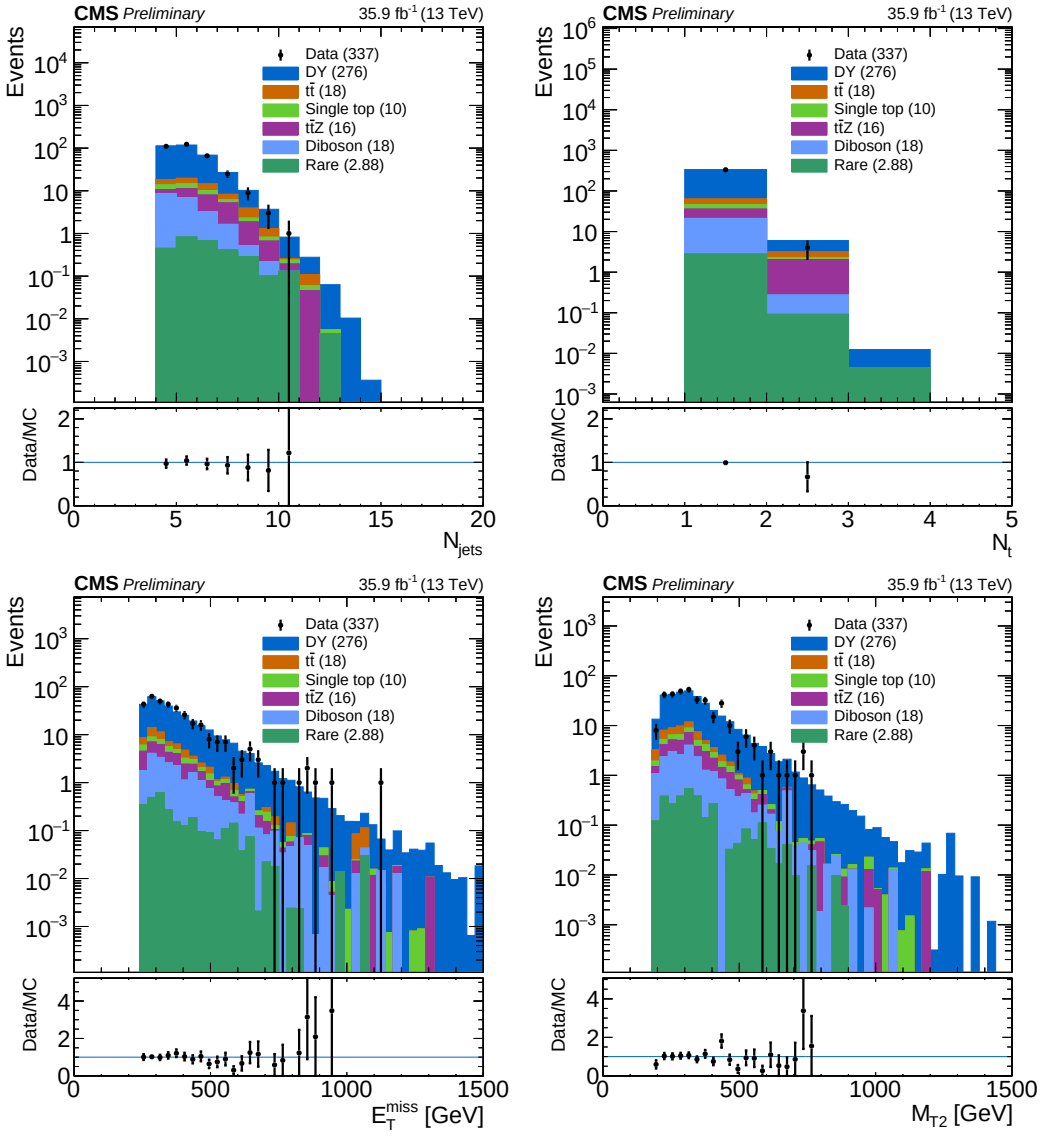

Figure 6.11: Comparison between DY data and MC samples for the N_{jets} (top left), N_{tops} (top right), $E_{\text{T}}^{\text{miss}}$ (bottom left) and M_{T2} (bottom right) in the tight $\mu\mu$ control region after applying both the $t\bar{t}$ and DY scale factors, as well as the normalization weight R_{norm}.

ergy correction $E_{\mathrm{T}}^{\mathrm{miss}}$ uncertainties, b-tag scale factors, the trigger efficiency scale factors. Systematic uncertainties inherent to the prediction method include uncertainty in the normalization factor R_{norm}, differences between data and MC etc. Major sources and their contribution are shown in Table 6.3.

Table 6.3: Contributions from different sources of systematic uncertainty to the $Z \to \nu\nu$ background prediction.

Source	Relative Uncertainty in %
R_{norm}	7.9%
Data/MC shape differences	9 – 55%
Stat. uncertainty on Data/MC comparison	11 – 56%
$Z \to \nu\nu$ MC statistics	1 – 100%
Shape variation due to μ_R, μ_F variations	<1% – 39%
Shape variation due to PDF variations	1% – 45%
Jet energy scale	2% – 75%
$E_{\mathrm{T}}^{\mathrm{miss}}$ energy scale	1% – 28%
b-tag SF	1% – 23%
b-mistag SF	<1% – 16%
Trigger efficiency	<14%

The $Z \to \nu\nu$ background prediction in each bin along with the statistical and systematic uncertainties is shown in Fig. 6.12. For bins that have zero events, the statistical uncertainty is treated as the average weight (sum of the weights squared divided by the weight) times the Poisson error on 0, which is 1.8.

6.3 Background from QCD Multijet Events

In the standard model, the QCD processes produce multijet events in the final state. If one or more jets energy is under-measured, the event may end up with a spurious imbalance of energy $E_{\mathrm{T}}^{\mathrm{miss}}$. These types of events, which consist of multiple jets and missing energy, can easily enter our search regions. Even though it is very rare to incorrectly reconstruct a bottom or top quark event, the very large QCD cross section means that estimating their contribution in the signal region is necessary. Monte

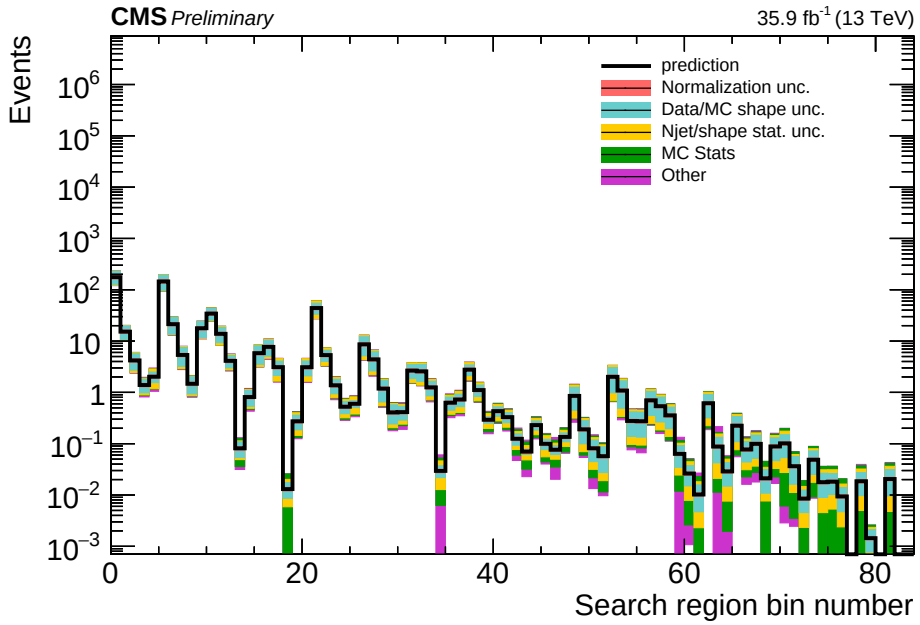

Figure 6.12: $Z \to \nu\nu$ background prediction for all search bins, including the breakdown of the various uncertainties.

Carlo studies have shown that cuts on $E_{\mathrm{T}}^{\mathrm{miss}}$ and the angle between a jets and the direction of the missing energy ($\Delta\phi$) between jets and $E_{\mathrm{T}}^{\mathrm{miss}}$ vector suppress most of the QCD backgrounds. But control samples used in the background estimation also have low statistics in the QCD background. Moreover, the contribution from $t\bar{t}$ processes makes it difficult to use the more common background estimation techniques, which would simply extrapolate QCD dominated distributions from the "sidebands" into the signal regions. The procedure to estimate the background involves selecting QCD enriched but signal depleted data samples from which $t\bar{t}$, Z+jets, W+jets processes are subtracted. Due to lack of statistics, we use MC samples to derive the translation factor, although we normalize their values to a data measurement in the 200 GeV $< E_{\mathrm{T}}^{\mathrm{miss}} <$ 250 GeV bin, just below the signal region, where there are enough statistics.

6.3.1 Translation Factor Method and Measurement

We create a QCD enriched sideband sample by applying all baseline cuts to the data but we invert the $\Delta\phi$ requirement. Fig. 6.13 shows typical events that passed $\Delta\phi$ cut and inverted $\Delta\phi$ ($\Delta\bar{\phi}$) case.

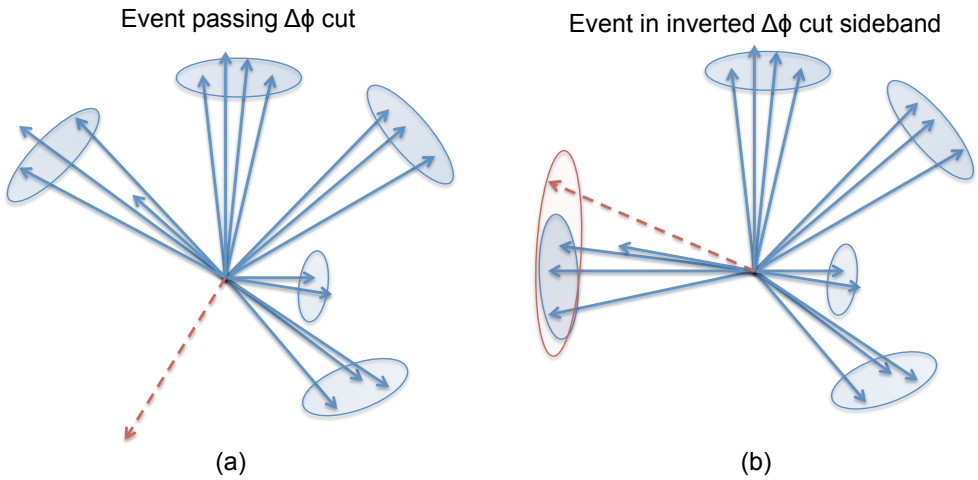

Figure 6.13: (a) Example of an event passing the $\Delta\phi$ cut. $E_{\mathrm{T}}^{\mathrm{miss}}$ is well separated from jets and p_{T} of the leading three jets.(b) Example of an event failing the $\Delta\phi$ cut. $E_{\mathrm{T}}^{\mathrm{miss}}$ is well aligned with one of the leading jets and most likely arises from jet mismeasurement.

The number of QCD events in $\Delta\bar{\phi}$ regions are obtained by subtracting the lost lepton, the hadronic tau, and the $Z \to \nu\nu$ contributions from data.

$$N_{QCD}^{\Delta\bar{\phi}} = N_{Data}^{\Delta\bar{\phi}} - N_{LL}^{\Delta\bar{\phi}} - N_{\tau_h}^{\Delta\bar{\phi}} - N_{Z\to\nu\nu}^{\Delta\bar{\phi}}, \tag{6.5}$$

where $N_X^{\Delta\bar{\phi}}$ is the number of type X events in the $\Delta\bar{\phi}$ sideband. Contributions subtracted in equation 6.5 are estimated using the technique discussed in the previous

sections. The translation factor, T_{QCD}^{MC} , is defined as the ratio of the MC predictions for the $\Delta\phi$ and $\Delta\bar{\phi}$ samples:

$$T_{QCD}^{MC} = \frac{N_{MC-QCD}^{\Delta\phi}}{N_{MC-QCD}^{\Delta\bar{\phi}}}. \tag{6.6}$$

while the final QCD background prediction in the search regions is calculated as:

$$N_{QCD}^{SR} = N_{QCD}^{\Delta\bar{\phi}} \times T_{QCD}^{Scale}, \tag{6.7}$$

where $N_{QCD}^{\Delta\bar{\phi}}$ comes from data (as defined in Eq. 6.5), and T_{QCD}^{Scale} is the T_{QCD}^{MC} normalized to a translation factor measured in the 200 GeV $< E_{\mathrm{T}}^{\mathrm{miss}} <$ 250 GeV sideband from data. This normalization provides a more accurate estimation of the true translation factors because although we trust (within the assigned uncertainties) the shape of the MC distributions utilized to calculate them, we do not trust their absolute values, which are corrected using the low 200 GeV $< E_{\mathrm{T}}^{\mathrm{miss}} <$ 250 GeV sideband T_{QCD}^{Data} measurement.

The procedure to derive the translation factors is the following:

- Calculate T_{QCD}^{MC} from QCD MC
- Measure T_{QCD}^{Data} from data in low $E_{\mathrm{T}}^{\mathrm{miss}}$ sideband
- Measure T_{QCD}^{Scale} by normalizing the T_{QCD}^{MC} versus $E_{\mathrm{T}}^{\mathrm{miss}}$ functions using the sideband T_{QCD}^{Data} factors measured in real data from the 200 GeV $< E_{\mathrm{T}}^{\mathrm{miss}} <$ 250 GeV bin. T_{QCD}^{Scale} are factors applied to get final QCD background predictions.

6.3.2 Systematic Uncertainties and Prediction

A systematic uncertainty in the QCD multijet prediction for each search region is evaluated as the difference between the event yield obtained directly from the QCD multijet simulation for that region and the prediction obtained by applying the background prediction procedure to simulated QCD multijet samples (30% to 500%). Additional sources of uncertainty are from the statistical uncertainty in the translation factors (30% to 300%) and the subtraction of the non-QCD-multijet SM contributions to the QCD control sample (2% to 50%). The validity of the method is checked by a closure test. In the closure test, direct simulated samples are compared with simulated samples treated as if they were data.

6.4 Background From Other Processes

Besides the dominant backgrounds discussed above, other SM backgrounds with small cross sections were considered and estimated for this analysis. Backgrounds from rare events contribute to only a small fraction of the total background and have only a small effect on the final result. These are diboson or multiboson processes associated with the production of top quark pairs. Fig. 6.14 shows $t\bar{t}Z$ and $t\bar{t}W^+$ production mechanisms in proton-proton collisions.

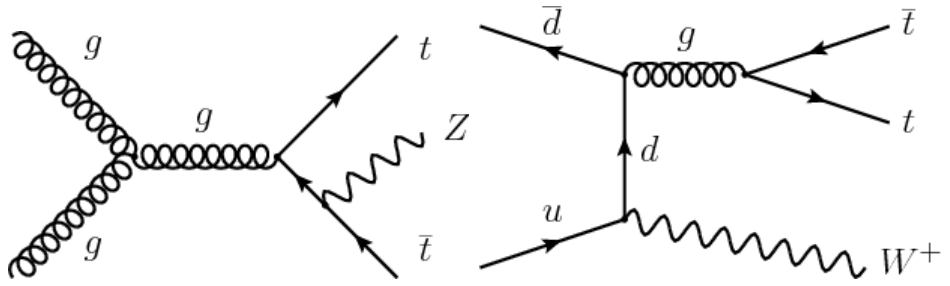

Figure 6.14: Dominant feynmann diagram for $t\bar{t}Z$(left) and $t\bar{t}W^+$(right).

Estimates of the rates of rare background processes are taken directly from the simulation. Processes such as $t\bar{t}Z$ form irreducible backgrounds when the Z decays to $\nu\nu$ and both top quarks decay hadronically. The $t\bar{t}Z$ cross section at 13 TeV is 782.6 pb so the predicted yield of $t\bar{t}Z$ events in the search bins is less than 10% of the total background. Given the small cross section associated with this process, we rely on simulation to generate a prediction, although this estimation is validated using real collider data. A generator-level veto of a W or Z decaying leptonically is applied to avoid double counting with the lost lepton and hadronic tau backgrounds. Except for the $t\bar{t}Z$ process, the other backgrounds are combined with the rare background. The yield of $t\bar{t}Z$ and rare processes are shown in Fig. 6.15. The yields of events in this sample from simulation and data are found to agree within a statistical uncertainty of 30%, which is taken as the systematic uncertainty in the $t\bar{t}Z$ background estimate.

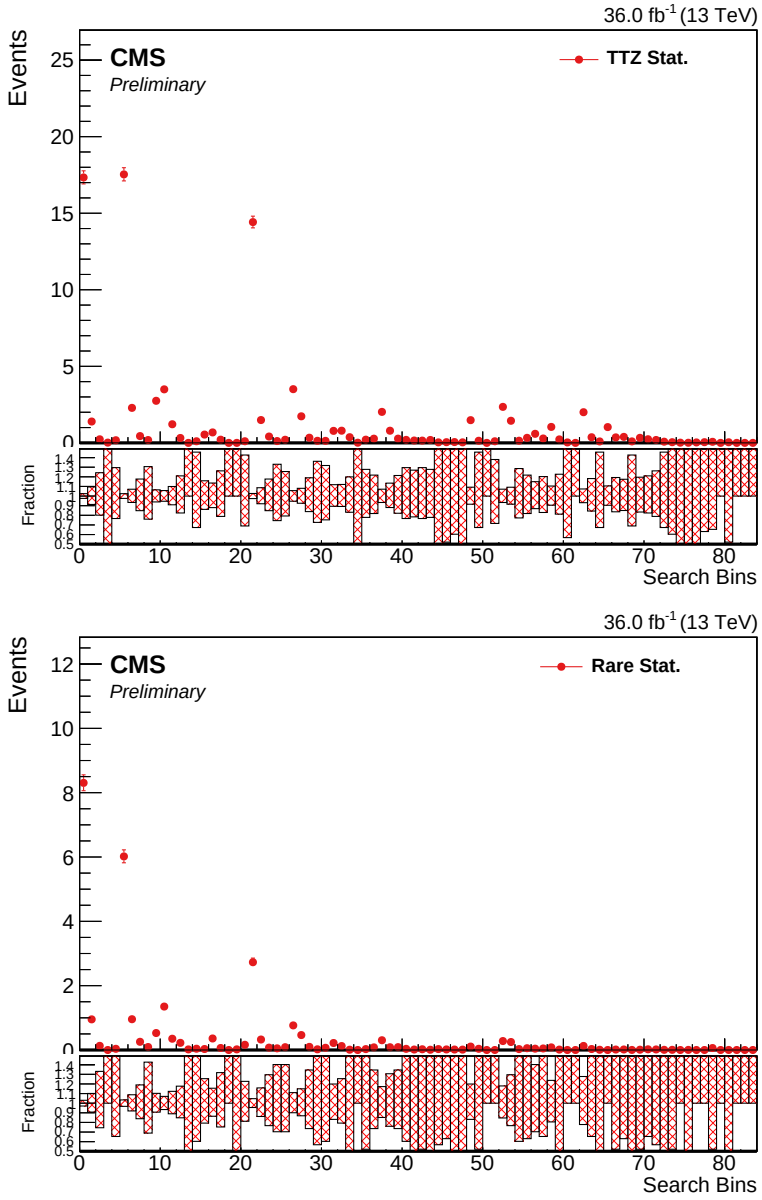

Figure 6.15: Yield of the $t\bar{t}Z$ (top) and rare background (bottom) prediction normalized to 36 fb[1].

CHAPTER 7

Results and Interpretation

7.1 Results

Our final prediction for the total background, including all sources utilizing the full data set and all control samples was compared to data corresponding to the integrated luminosity of 35.9 fb^{-1} as shown in Fig. 7.1. Statistical uncertainties of data and systematic uncertainties of predictions are shown. The bottom plot shows the ratio of data over total background predictions. There is an overall agreement in all search bins between the SM prediction and data within the uncertainties.

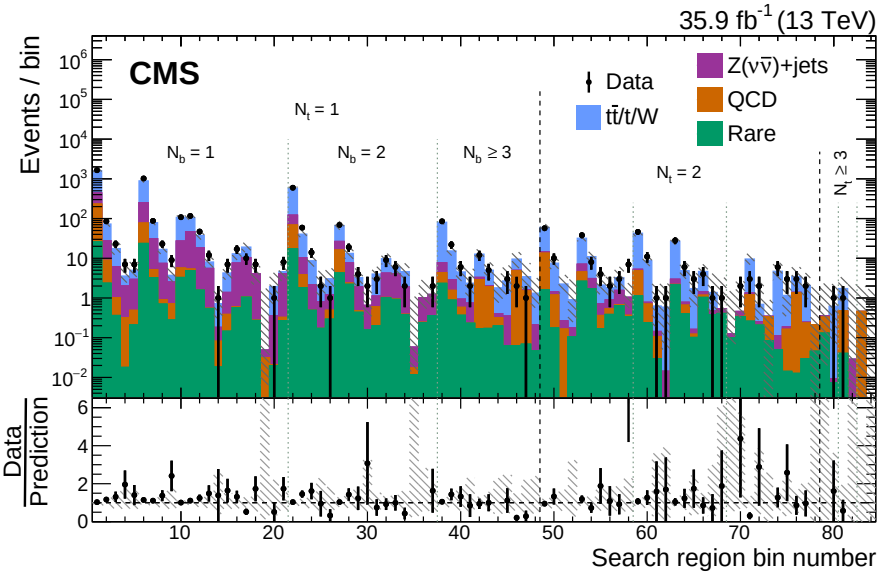

Figure 7.1: Observed data yields (black points) and prefit SM background predictions (filled solid areas) for the 84 search regions, where "prefit" means there is no constraint from the likelihood fit. The ratio of data to background prediction in each bin is shown in the bottom plot. The hatched bands correspond to the total uncertainty in the background prediction.

7.2 Statistics

Standard presentations of results in search experiments have always been a point of discussion among particle physicists. Bayesian credible intervals depend on some prior probability distribution and are often somewhat suggestive. In some cases where data do not overwhelm the prior probability, physicist want to summarize the observation independently. Frequentists on the other hand tend to draw conclusions based on compatibility of data with theory. In high statistics and signal dominated regions, both school of thoughts tend to converge. Unfortunately, experiments usually suffer from small signals buried in a large background. In such a case, misinterpretation of frequentist statements become a serious issue.

In this analysis, the null hypothesis is an observation that can be explained by SM contributions only, and the alternative hypothesis is the one where new physics is required to explain the observation. We aim to exclude the signal in it's absence and confirm it's existence in case of the actual signal. The sensitivity of the analysis to the different models discussed in Chapter 5 is investigated by computing the expected limits as a function of the mass of the lightest supersymmetric particle (LSP) versus the mass of the top squark. For limit calculations, we use the Modified Frequentist (CL_s) statistical method [61, 62].

For n different search channels, if s_i, B_i and d_i are signals predicted from MC, background and observed candidates in the i^{th} channel, trespectively, hen the test-statistic Q_i in that particular channel is given by,

$$Q_i = \frac{e^{-(s_i+b_i)}(s_i+b_i)^{d_i}}{d_i!} \Big/ \frac{e^{-b_i}(b_i)^{d_i}}{d_i!}, \tag{7.1}$$

and the test-statistic is the product of Q_i all over n channels. The test-statistic Q is constructed for the entire experiment so that the confidence in the signal + background hypothesis is given by the probability that the test-statistic is less than or equal to the value observed in the entire experiment, Q_{obs}, i.e.,

$$CL_{s+b} = P_{s+b}(Q \leq Q_{obs}), \tag{7.2}$$

where $P_{s+b}(Q \leq Q_{obs})$ is the sum of the Poisson probabilities. The confidence level for the background alone is,

$$CL_b = P_b(Q \leq Q_{obs}). \tag{7.3}$$

Values of CL_b very close to 1 indicate poor compatibility with the background hypothesis and favor the signal+background hypothesis. CL_s is a ratio of confidence levels:

$$CL_s = \frac{CL_{s+b}}{CL_b}. \tag{7.4}$$

The motivation behind the CL_s method is to avoid excluding or discovering signals to which the analysis is not sensitive. For example, observing less than the mean expected background events could be accommodated best with a negative signal cross section. The exclusion may be as strong as to exclude the zero signal scenario at a given confidence level. This is a valid result in terms of statistics, but it says more about fluctuations of the (known) background than about the searched signal. This effect is avoided by normalizing the confidence level of the signal plus background hypothesis CL_{s+b} to the confidence level in the background-only hypothesis CL_b. For this analysis, the Higgs combination tool was used to calculate the limits, the full frequentist CL_s limit calculation together with the LHC-like test statistics [63].

7.3 Systematic Uncertainties

Sources of systematic uncertainties were studied on MC signal samples and their contributions were computed as follows:

- **MC Statistics:** statistical uncertainties from MC signal samples.
- **Luminosity:** A 2.6% flat contribution is assigned as per suggestion from the CMS working group assigned to this task for the collaboration.
- **Lepton Veto:** The number of signal events vetoed by each category are evaluated. Then the yields are varied by the corresponding veto category uncertainties and propogated to determine the relative changes to the signal yields in each search bin. The number of vetoed events effectively reflects the various lepton selection efficiency.
- **b-tag Efficiency:** The b-tagging and mistagging scale factors are functions of the jet p_{T} and η. Scale factors were varied within their uncertainties and propagated to the signal bins to determine the signal uncertainties for each bin. We take the conservative assumption that the charm-mistagging scale factor uncertainty is correlated with the b-tagging scale factor. Both b-tagging and charm-mistagging scale factors were varied together, and the light flavor-mistagging scale factors were varied independently.
- **b-tag FastSim Corrections:** The b-tagging and mistagging performance as derived from fast simulation was corrected to match the full simulation predictions. Separate correction factors are derived for b-jets, c-jets, and light-flavor-jets, as a function of the jet p_{T} and η. As with the scale factors above, the correction factors for each type of jet are varied independently within their un-

certainties and propagated to determine the uncertainty in the signal for each search bin.

- **Trigger Efficiency:** The trigger efficiencies are measured using data as described in Sec. 5.1. The signal samples are corrected for the trigger inefficiencies. The effect of trigger efficiency uncertainties on the signal samples is at most 2.6% in the lowest $E_{\mathrm{T}}^{\mathrm{miss}}$ bins.

- **Renormalization and Factorization Scales:** This uncertainty was calculated using the envelope of the weights obtained from varying the renormalization and factorization scales, μ_R and μ_F, by a factor of two [64, 65]. These effects on the shape of the signal are taken as the uncertainties. These uncertainties are considered as uncertainties on the signal cross section.

- **Initial State Radiation:** An ISR correction is derived from $t\bar{t}$ events, with a selection requiring two leptons (electrons or muons) and two b-tagged jets, implying that any other jets in the event arise from ISR. The correction factors are 1.000, 0.882, 0.792, 0.702, 0.648, 0.601, 0.515 for N_{jet}^{ISR} = 0, 1, 2, 3, 4, 5, 6+. The corrections are applied to the simulated signal jet samples with an additional normalization factor, typically $\sim$1.15 (depending on the signal model), to ensure the overall cross section of the sample remains constant. The systematic uncertainty in these corrections is chosen to be half of the deviation from unity for each correction factor.

- **Jet Energy Corrections:** The jet energy corrections (JEC) are varied within the p_{T} and η-dependent jet energy scale uncertainties available in the official CMS database. A different set of corrections and uncertainties are used in fast simulation samples. These variations are propagated into the jet-dependent search variables, such as: N_{b-jets}, N_{tops}, $E_{\mathrm{T}}^{\mathrm{miss}}$, M_{T2}, H_{T}, $\Delta\phi(E_{\mathrm{T}}^{\mathrm{miss}}, j_i)$.

- **Parton Distribution Functions:** The PDF4LHC prescription [66] for the uncertainty on the total cross section is included as ±1 sigma bands in the results distributions.

Additional uncertainties such as data-MC difference scale factors and Fullsim/Fastsim scale factor for top quark reconstruction, uncertainties associated with $E_{\mathrm{T}}^{\mathrm{miss}}$ are considered. The signal systematic list and their typical range are shown in Tables 7.1 and 7.2.

Table 7.1: In T2tt SMS, the signal systematic sources and their typical ranges as calculated. These are relative uncertainties.

FSource	Typical Value
MC Statistics	1-100%
Luminosity	2.6%
Renormalization and factorization scales	0-2.4%
ISR recoil	%0-46
b-tagging efficiency, heavy flavor	0-17%
b-tagging efficiency, light flavor	0-17%
Lepton veto	0-4.7%
Jet energy scale	0-20%
MET uncerntainty	0-24%
Trigger	0-2.6%
Full/fastsim scale for top reco	0-19%
top tagger efficiency data/MC difference	0-14%

7.4 Interpretation

The exclusion limits on the model T2tt (a direct production of the top squark) with all of the different sources of the signal systematic uncertainties are shown in Fig. 7.2. For the 35.9 fb^{-1} data we have substantial improvement of our exclusion to the top squark mass up to 1133 GeV and the LSP mass up to 480 GeV for expected limits with respect to the previous result [59]. And for observed limits, we have exclusion

Table 7.2: In T1tttt SMS, the signal systematic sources and their typical ranges as calculatd. These are relative uncertainties.

Source	Typical Value
MC Statistics	1-100%
Luminosity	2.6%
Renormalization and factorization scales	0-3.5%
ISR recoil	%0-45
b-tagging efficiency, heavy flavor	0-16%
b-tagging efficiency, light flavor	0-21%
Lepton veto	0-6.8%
Jet energy scale	0-34 %
MET uncerntainty	0-17%
Trigger	0-2.6%
Full/fastsim scale for top reco	0-24 %
top tagger efficiency data/MC difference	0-11%

up to 1022 GeV of the top squark mass and up to 430 GeV of the LSP mass.

The results were also interpreted for the gluino mediated top squark production (T1tttt SMS) model shown in Fig. 7.3. All different sources of the systematic uncertainties were included in the limit calculations. For expected limits, the maximum exclusion of the gluino mass is 2028 GeV and the maximum LSP mass exclusion is 1154 GeV. For the observed limits, we have exclusion of the gluino mass up to 2038 GeV and 1154 GeV for the LSP mass. The results are a great improvement when compared to previous results based on data taken in the 2015 LHC run with an integrated luminosity of 2.3 fb^{-1} [59].

7.5 Summary

Results have been presented of a search for direct and gluino-mediated top squark production in proton-proton collisions at a center-of-mass energy of 13 TeV. The central feature of the analysis is our top quark identification algorithm that reconstructs

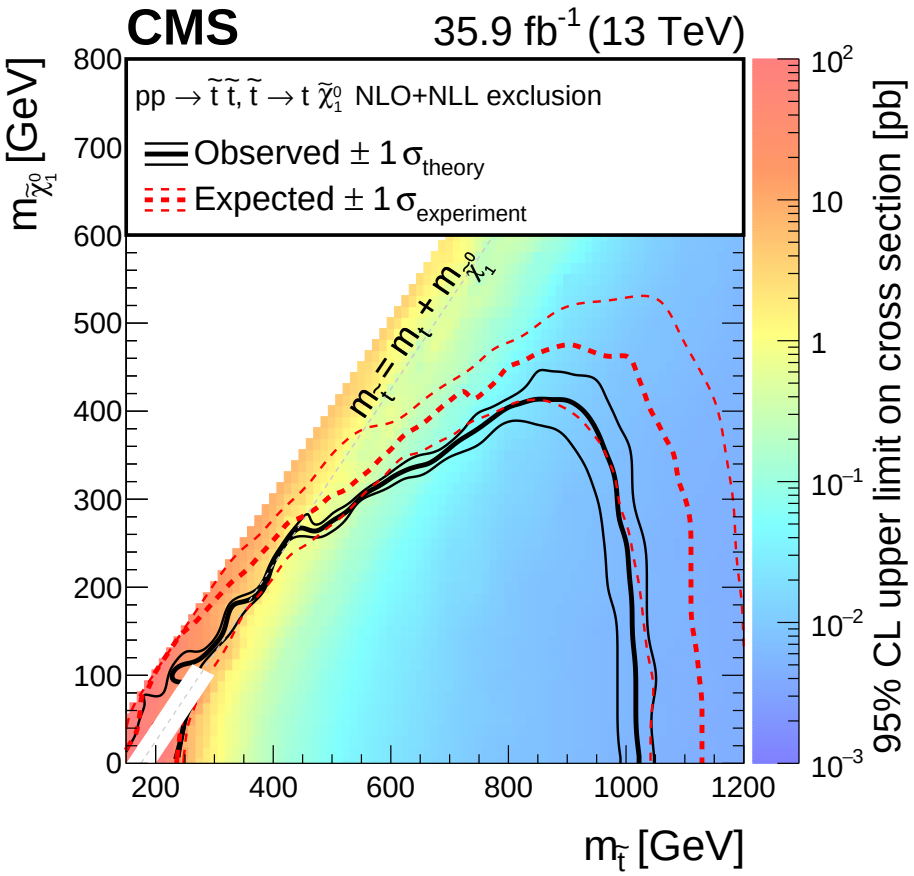

Figure 7.2: The 95% CL upper limit on the production cross section of the T2tt simplified model as a function of the top squark and LSP masses. The solid black curves represent the observed exclusion contour with respect to NLO+NLL signal cross sections and the change in this contour due to variation of these cross sections within their theoretical uncertainties [12]. The dashed red curves indicate the mean expected exclusion contour and the region containing 68% of the distribution of expected exclusion limits under the background-only hypothesis. No interpretation is provided for signal models for which $|m_{\tilde{t}} - m_{\tilde{\chi}^0_1} - m_{\mathrm{T}}| \leq 25$ GeV and $m_{\tilde{t}} \leq 275$ GeV because signal events are essentially indistinguishable from SM $t\bar{t}$ events in this region, rendering the signal event acceptance difficult to model.

hadronically decaying top quark across a wide spectrum of top quark transverse momentum p_{T} with very good efficiency. The search uses all-hadronic events with at least four jets and a large imbalance in transverse momentum ($E_{\mathrm{T}}^{\mathrm{miss}}$), selected from data corresponding to an integrated luminosity of 35.9 fb[1] collected with the CMS

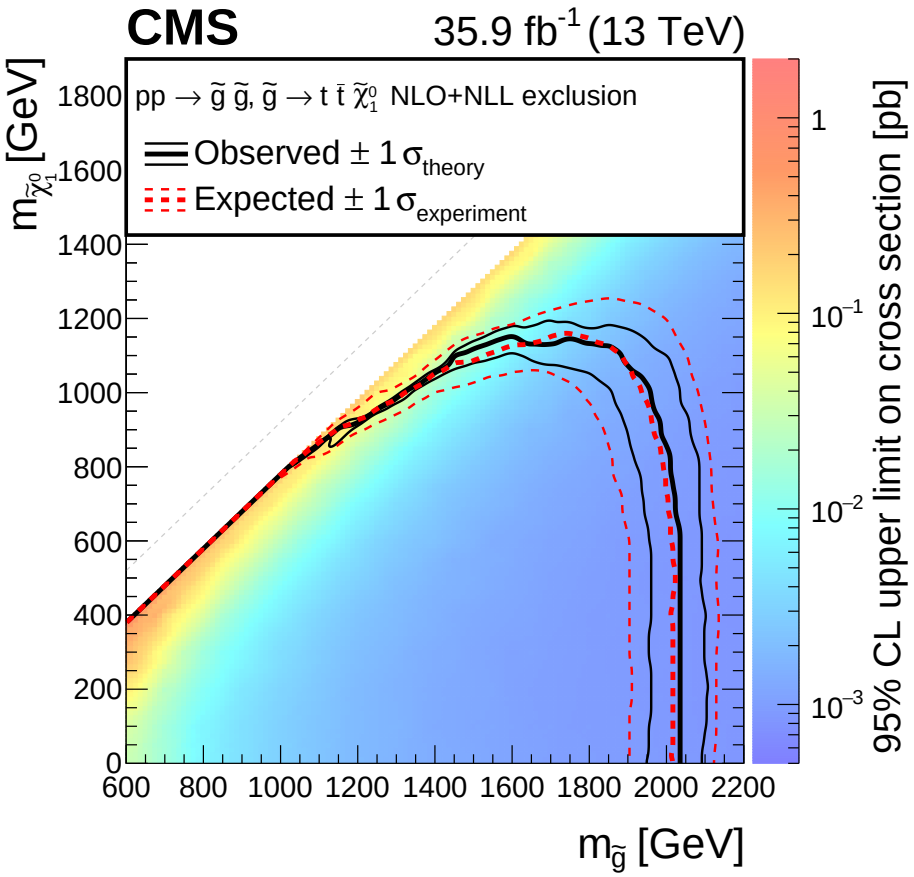

Figure 7.3: The 95% CL upper limit on the production cross section of the T1tttt simplified model as a function of the top squark and LSP masses. The meaning of the curves is explained in the 7.2 caption.

detector at the LHC in 2016. A set of 84 search regions where defined based on $E_{\mathrm{T}}^{\mathrm{miss}}$, M_{T2}, the number of top quark tagged objects, and the number of bottom quark jets. No statistically significant excess of events was observed when compared to the expectation from the standard model predictins.

In simplified models of pair production of top squarks, that decay to a top quark and a neutralino, top squark masses of up to 1020 GeV and neutralino masses up to 430 GeV are excluded at the 95% confidence level. For models with gluino pair production, gluino masses of up to 2040 GeV, and neutralino masses up to 1150

GeV are excluded, for the T1tttt model. These results significantly extend those of our previous study [59]. The use of top quark tagging was an exclusive approach taken in contrast to other analyses in CMS. A significant improvement of top quark tagging method over previous methods not only improved signal sensitivity, but also improved our background estimates. Top tagging provided a novel means to search for new phenomena at the LHC, yielding complementary sensitivity to other approaches.

Bibliography

[1] Gordon Kane. *Modern elementary particle physics : the fundamental particles and forces?* Perseus Publishing, 1993.

[2] Wikipedia Authors. Standard model of particle physics — Wikipedia, the free encyclopedia, 2018. [Online; accessed 11-June-2018]. URL: https://en.wikipedia.org/wiki/Standard_Model.

[3] S. L. Bein. *Targeting the Minimal Supersymmetric Standard Model with the Compact Muon Solenoid Experiment*. PhD thesis, Florida State University, 2016. URL: http://purl.flvc.org/fsu/fd/FSU_2016SU_Bein_fsu_0071E_13432.

[4] Christoph Borschensky, Michael Krmer, Anna Kulesza, Michelangelo Mangano, Sanjay Padhi, Tilman Plehn, and Xavier Portell. Squark and gluino production cross sections in pp collisions at $\sqrt{s} = 13$, 14, 33 and 100 TeV. *Eur. Phys. J.*, C74(12):3174, 2014. arXiv:1407.5066, doi:10.1140/epjc/s10052-014-3174-y.

[5] Oliver S. Bruning, P. Collier, P. Lebrun, S. Myers, R. Ostojic, J. Poole, and P. Proudlock. LHC Design Report Vol.1: The LHC Main Ring. Technical report, 2004.

[6] G. L. Bayatian et al. CMS physics: Technical design report. 2006.

[7] CMS Collaboration. *CMS, tracker technical design report*. 1998. URL: http://weblib.cern.ch/abstract?CERN-LHCC-98-6.

[8] CMS Collaboration. CMS: The electromagnetic calorimeter. Technical design report. 1997.

[9] The CMS hadron calorimeter project: Technical Design Report. 1997. URL: http://cds.cern.ch/record/357153.

[10] The CMS Collaboration. Particle-flow event reconstruction in cms and performance for jets, taus, and met, April 2009. URL: http://cdsweb.cern.ch/record/1194487.

[11] Byron P. Roe, Hai-Jun Yang, Ji Zhu, Yong Liu, Ion Stancu, and Gordon McGregor. Boosted decision trees, an alternative to artificial neural networks. *Nucl. Instrum. Meth.*, A543(2-3):577–584, 2005. arXiv:physics/0408124, doi:10.1016/j.nima.2004.12.018.

[12] Christoph Borschensky, Michael Krmer, Anna Kulesza, Michelangelo Mangano, Sanjay Padhi, Tilman Plehn, and Xavier Portell. Squark and gluino production cross sections in pp collisions at $\sqrt{s} = 13$, 14, 33 and 100 TeV. *Eur. Phys. J.*, C74(12):3174, 2014. arXiv:1407.5066, doi:10.1140/epjc/s10052-014-3174-y.

[13] CMS Collaboration. Observation of a new boson at a mass of 125 gev with the cms experiment at the lhc. *Physics Letters B*, 716(1):30 – 61, 2012. URL: http://www.sciencedirect.com/science/article/pii/S0370269312008581, doi:http://dx.doi.org/10.1016/j.physletb.2012.08.021.

[14] Irene Niessen. *Supersymmetric Phenomenology in the mSUGRA Parameter Space*. PhD thesis, Nijmegen U., IMAPP, 2008. URL: https://inspirehep.net/record/796204/files/arXiv:0809.1748.pdf, arXiv:0809.1748.

[15] Steven Weinberg. A model of leptons. *Phys. Rev. Lett.*, 19:1264–1266, Nov 1967. URL: https://link.aps.org/doi/10.1103/PhysRevLett.19.1264, doi:10.1103/PhysRevLett.19.1264.

[16] Peter W. Higgs. Broken symmetries and the masses of gauge bosons. *Phys. Rev. Lett.*, 13:508–509, Oct 1964. URL: https://link.aps.org/doi/10.1103/PhysRevLett.13.508, doi:10.1103/PhysRevLett.13.508.

[17] P. M. Watkins. DISCOVERY OF THE W AND Z BOSONS. *Contemp. Phys.*, 27:291–324, 1986. doi:10.1080/00107518608211015.

[18] C. Patrignani et al. Review of Particle Physics. *Chin. Phys.*, C40(10):100001, 2016. doi:10.1088/1674-1137/40/10/100001.

[19] Marko B. Popovic. The Standard model hierarchy, fine tuning, and negativity of the Higgs mass squared. 2002. arXiv:hep-ph/0204345.

[20] G. Hinshaw et al. Five-year wilkinson microwave anisotropy probe (wmap) observa- tions: Data processing, sky maps, and basic results. *The Astrophysical Journal Supplement Series*, 2008.

[21] Steen Hannestad, Alessandro Mirizzi, Georg G. Raffelt, and Yvonne Y. Y. Wong. Neutrino and axion hot dark matter bounds after WMAP-7. *JCAP*, 1008:001, 2010. doi:10.1088/1475-7516/2010/08/001.

[22] Palash B. Pal. Dirac, Majorana and Weyl fermions. *Am. J. Phys.*, 79:485–498, 2011. arXiv:1006.1718, doi:10.1119/1.3549729.

[23] S. P. Martin. *A supersymmetry primer*. 2016. URL: https://arxiv.org/abs/hep-ph/9709356v7, doi:10.1142/9789812839657_0001.

[24] H. E. Haber. *Introductory low-energy supersymmetry*. 1993. URL: hep-ph/9306207.

[25] M. Dugan, Benjamin Grinstein, and Lawrence J. Hall. CP Violation in the Minimal N=1 Supergravity Theory. *Nucl. Phys.*, B255:413–438, 1985. doi:10.1016/0550-3213(85)90145-2.

[26] Serguei Chatrchyan et al. Interpretation of Searches for Supersymmetry with simplified Models. *Phys. Rev.*, D88(5):052017, 2013. arXiv:1301.2175, doi:10.1103/PhysRevD.88.052017.

[27] Giulia Lanza, Vincent Baglin, Giuseppe Bregliozzi, and Paolo Chiggiato. LHC Experimental Beam Pipe Upgrade during LS1. In *Proceedings, 5th International Particle Accelerator Conference (IPAC 2014): Dresden, Germany, June 15-20, 2014*, page WEPME044, 2014. URL: http://jacow.org/IPAC2014/papers/wepme044.pdf.

[28] G. Aad et al. The ATLAS Experiment at the CERN Large Hadron Collider. *JINST*, 3:S08003, 2008. doi:10.1088/1748-0221/3/08/S08003.

[29] L. Rossi. The lhc superconducting magnets. In *Proceedings of the 2003 Particle Accelerator Conference*, volume 1, pages 141–145 Vol.1, May 2003. doi:10.1109/PAC.2003.1288863.

[30] L. Rossi. Superconducting magnets for the lhc main lattice. *IEEE Transactions on Applied Superconductivity*, 14(2):153–158, June 2004. doi:10.1109/TASC.2004.829031.

[31] *The CMS muon project: Technical Design Report.* Technical Design Report CMS. CERN, Geneva, 1997. URL: http://cds.cern.ch/record/343814.

[32] *The CMS tracker: addendum to the Technical Design Report.* Technical Design Report CMS. CERN, Geneva, 2000. URL: https://cds.cern.ch/record/490194.

[33] G. Baiatian et al. Design, Performance, and Calibration of CMS Hadron-Barrel Calorimeter Wedges. 2007.

[34] G. Baiatian et al. Design, performance, and calibration of CMS hadron endcap calorimeters. 2008.

[35] G. Bayatian et al. Design, performance and calibration of the CMS forward calorimeter wedges. *Eur. Phys. J.*, C53:139–166, 2008. doi:10.1140/epjc/s10052-007-0459-4.

[36] G. Acquistapace et al. CMS, the magnet project: Technical design report. 1997.

[37] Serguei Chatrchyan et al. Performance of CMS muon reconstruction in pp collision events at $\sqrt{s} = 7$ TeV. *JINST*, 7:P10002, 2012. arXiv:1206.4071, doi:10.1088/1748-0221/7/10/P10002.

[38] P. Sphicas. CMS: The TriDAS project. Technical design report, Vol. 2: Data acquisition and high-level trigger. 2002.

[39] Florian Beaudette. The CMS Particle Flow Algorithm. In *Proceedings, International Conference on Calorimetry for the High Energy Frontier (CHEF 2013): Paris, France, April 22-25, 2013*, pages 295–304, 2013. URL: https://inspirehep.net/record/1279774/files/arXiv:1401.8155.pdf, arXiv:1401.8155.

[40] A. M. Sirunyan et al. Particle-flow reconstruction and global event description with the CMS detector. *JINST*, 12(10):P10003, 2017. arXiv:1706.04965, doi:10.1088/1748-0221/12/10/P10003.

[41] Wolfgang Adam, Boris Mangano, Thomas Speer, and Teddy Todorov. Track Reconstruction in the CMS tracker. Technical Report CMS-NOTE-2006-041, CERN, Geneva, Dec 2006. URL: http://cds.cern.ch/record/934067.

[42] M Rovere. Cms reconstruction improvements for the tracking in large pileup events. *Journal of Physics: Conference Series*, 664(7):072040, 2015. URL: http://stacks.iop.org/1742-6596/664/i=7/a=072040.

[43] J.P. Merlo. Cms hadronic forward calorimeter. *Nuclear Physics B - Proceedings Supplements*, 61(3):41 – 46, 1998. Proceedings of the Fifth International Conference on Advanced Technology and Particle Physics. URL: http://www.sciencedirect.com/science/article/pii/S0920563297005367, doi:https://doi.org/10.1016/S0920-5632(97)00536-7.

[44] Wolfgang Adam, R. Frhwirth, Are Strandlie, and T. Todor. Reconstruction of Electrons with the Gaussian-Sum Filter in the CMS Tracker at the LHC. 2005.

[45] Torbjorn Sjostrand, Stephen Mrenna, and Peter Z. Skands. A Brief Introduction to PYTHIA 8.1. *Comput. Phys. Commun.*, 178:852–867, 2008. arXiv:0710.3820, doi:10.1016/j.cpc.2008.01.036.

[46] S. Agostinelli et al. Geant4a simulation toolkit. *Nuclear Instruments and Methods in Physics Research Section A: Accelerators, Spectrometers, Detectors and Associated Equipment*, 506(3):250 – 303, 2003. URL: http://www.sciencedirect.com/science/article/pii/S0168900203013688, doi:https://doi.org/10.1016/S0168-9002(03)01368-8.

[47] Matteo Cacciari, Gavin P. Salam, and Gregory Soyez. The Anti-k(t) jet clustering algorithm. *JHEP*, 04:063, 2008. arXiv:0802.1189, doi:10.1088/1126-6708/2008/04/063.

[48] Ryan Atkin. Review of jet reconstruction algorithms. *Journal of Physics: Conference Series*, 645(1):012008, 2015. URL: http://stacks.iop.org/1742-6596/645/i=1/a=012008.

[49] A Cambridge-Aachen (C-A) based Jet Algorithm for boosted top-jet tagging. 2009.

[50] CMS: The computing project. Technical design report. 2005.

[51] Serguei Chatrchyan et al. Identification of b-quark jets with the CMS experiment. *JINST*, 8:P04013, 2013. arXiv:1211.4462, doi:10.1088/1748-0221/8/04/P04013.

[52] C. G. Lester and D. J. Summers. Measuring masses of semiinvisibly decaying particles pair produced at hadron colliders. *Phys. Lett.*, B463:99–103, 1999. arXiv:hep-ph/9906349, doi:10.1016/S0370-2693(99)00945-4.

[53] Jehad Ali, Rehanullah Khan, Nasir Ahmad, and Imran Maqsood. Random forests and decision trees, 2012.

[54] F. Pedregosa, G. Varoquaux, A. Gramfort, V. Michel, B. Thirion, O. Grisel, M. Blondel, P. Prettenhofer, R. Weiss, V. Dubourg, J. Vanderplas, A. Passos, D. Cournapeau, M. Brucher, M. Perrot, and E. Duchesnay. Scikit-learn: Machine learning in Python. *Journal of Machine Learning Research*, 12:2825–2830, 2011.

[55] G. Bradski. The OpenCV Library. *Dr. Dobb's Journal of Software Tools*, 2000.

[56] Vardan Khachatryan et al. Searches for third-generation squark production in fully hadronic final states in proton-proton collisions at $\sqrt{s} = 8$ TeV. *JHEP*, 06:116, 2015. arXiv:1503.08037, doi:10.1007/JHEP06(2015)116.

[57] Andrew J. Larkoski, Simone Marzani, Gregory Soyez, and Jesse Thaler. Soft Drop. *JHEP*, 05:146, 2014. arXiv:1402.2657, doi:10.1007/JHEP05(2014)146.

[58] Jesse Thaler and Ken Van Tilburg. Identifying Boosted Objects with N-subjettiness. *JHEP*, 03:015, 2011. arXiv:1011.2268, doi:10.1007/JHEP03(2011)015.

[59] Vardan Khachatryan et al. Search for supersymmetry in the all-hadronic final state using top quark tagging in pp collisions at $\sqrt{s} = 13$ TeV. *Phys. Rev.*, D96(1):012004, 2017. arXiv:1701.01954, doi:10.1103/PhysRevD.96.012004.

[60] F. GARWOOD. (i) fiducial limits for the poisson distribution. *Biometrika*, 28:437442, Dec 1936. doi:https://doi.org/10.1093/biomet/28.3-4.437.

[61] A L Read. Presentation of search results: the cl s technique. *Journal of Physics G: Nuclear and Particle Physics*, 28(10):2693, 2002. URL: http://stacks.iop.org/0954-3899/28/i=10/a=313.

[62] Thomas Junk. Confidence level computation for combining searches with small statistics. *Nuclear Instruments and Methods in Physics Research Section A: Accelerators, Spectrometers, Detectors and Associated Equipment*, 434(2):435 – 443, 1999. URL: http://www.sciencedirect.com/science/article/pii/S0168900299004982, doi:https://doi.org/10.1016/S0168-9002(99)00498-2.

[63] Glen Cowan, Kyle Cranmer, Eilam Gross, and Ofer Vitells. Asymptotic formulae for likelihood-based tests of new physics. *The European Physical Journal C*, 71(2), 2011.

[64] M. Cacciari, S. Frixione, M. L. Mangano, P. Nason, and G. Ridolfi. The t anti-t cross-section at 1.8-TeV and 1.96-TeV: A Study of the systematics due to parton densities and scale dependence. *JHEP*, 04:068, 2004. arXiv:hep-ph/0303085, doi:10.1088/1126-6708/2004/04/068.

[65] Stefano Catani, Daniel de Florian, Massimiliano Grazzini, and Paolo Nason. Soft gluon resummation for Higgs boson production at hadron colliders. *JHEP*, 07:028, 2003. arXiv:hep-ph/0306211, doi:10.1088/1126-6708/2003/07/028.

[66] Jon Butterworth et al. PDF4LHC recommendations for LHC Run II. *J. Phys.*, G43:023001, 2016. arXiv:1510.03865, doi:10.1088/0954-3899/43/2/023001.

VITA

YAGYA R. JOSHI

Born, Lamjung, Nepal

2012 - 2018	PhD Candidate Florida International University Miami, Florida
2018 - Present	Dissertation Year Fellow Florida International University Miami, Florida
2016 - 2107	Graduate Teaching Assistant Florida International University Miami, Florida
2015 - 2106	Graduate Research Assistant Florida International University Miami, Florida
2012 - 2015	Presidential Fellow Florida International University Miami, Florida
2010 - 2012	Faculty Member Purbanchal University Kathmandu, Nepal
2007-2009	M.Sc. in Physics Tribhuvan University Kathmandu, Nepal
2007	B.Sc. in Physics Tribhuvan University Kathmandu, Nepal

PUBLICATIONS AND PRESENTATIONS

- Vardan Khachatryan et al. Search for supersymmetry in the all-hadronic final state using top quark tagging in pp collisions at $\sqrt{s}$ =13 TeV. Phys. Rev., D96(1):012004, 2017.
- Albert M Sirunyan et al. Search for supersymmetry in proton-proton collisionsat 13 TeV using identified top quarks. Phys. Rev., D97(1):012007, 2018.

- Y. Joshi, All hadronic top squark search with CMS detector at the 13 TeV proton- proton collision as the Large Hadron Collider, APS April Meeting 2016, Salt Lake City, Utah, April 16-19 2016

- Y. Joshi, Search for scalar quark pair production with CMS detector at the 13 TeV proton-proton collision as the Large Hadron Collider, FIU Graduate Symposium 2016

- Y. Joshi, Background estimation techniques search for scalar top-quark production with top quark tagging in the all-hadronic channel at 13 TeV with the CMS detector, APS April Meeting 2017, Washington DC, January 28-31 2017

- Y. Joshi, Top quark tagging technique at proton proton collision using machine learning techniques, Florida International University, Graduate Symposium 2017

- Y. Joshi, Top quark tagging technique using machine learning techniques, Florida International University, physics research competition April 16, 2017